

國立交通大學

機械工程學系

博士論文

球形螺旋齒輪之特性研究

Characteristic Study of Spherical Helical Gears



研究生：趙立碁

指導教授：徐瑞坤 教授

共同指導教授：蔡忠杓 教授

中華民國九十九年六月

球形螺旋齒輪之特性研究

Characteristic Study of Spherical Helical Gears

研究生：趙立碁

Student : Li-Chi Chao

指導教授：徐瑞坤 博士

Advisor : Dr. Ray-Quan Hsu

共同指導教授：蔡忠杓 博士

Co-Advisor : Dr. Chung-Biau Tsay

國立交通大學

機械工程學系

博士論文



Submitted to Department of Mechanical Engineering

College of Engineering

National Chiao Tung University

in partial Fulfillment of the Requirements

for the Degree of

Doctor of Philosophy

in

Mechanical Engineering

June 2010

Hsinchu, Taiwan, Republic of China

中華民國九十九年六月

球形螺旋齒輪之特性研究

學生：趙立基

指導教授：徐瑞坤博士

共同指導教授：蔡忠杓博士

國立交通大學機械工程學系

摘要

球形齒輪(Spherical gear)是由日本三留謙一教授所提出的一種新型的齒輪。由其幾何外形來區分，球形齒輪可分為凸狀球形齒輪(Convex spherical gear)與凹狀球形齒輪(Concave spherical gear)。由球形齒輪所組成之齒輪組共有三種配對型式：凸狀球形齒輪配凸狀球形齒輪、凸狀球形齒輪配凹狀球形齒輪及凸狀球形齒輪配正(螺旋)齒輪。與一般常用之正齒輪組不同的是，球形齒輪組(Spherical gear set)具有可容許軸交角變動與軸裝配誤差且不發生齒形干涉之傳動特性。

基於球形齒輪在組裝上的優點，本論文提出一種結合球形齒輪及螺旋齒輪特性的球形螺旋齒輪(Spherical helical gear)。球形螺旋齒輪除了具有球形齒輪所有的幾何特色及傳動特性外，亦可透過球形螺旋齒輪之齒輪螺旋角(Helix angle)的設計，以交錯軸的組裝型式(Crossed axes mounting mode)進行傳動。因此，若能建立出球形螺旋齒輪的數學模式，則可利用此數學模式來進行球形螺旋齒輪之相關分析，以提供產業界更進一步了解球形螺旋齒輪之特性及應用上的限制。

由於滾齒加工方法具有切削效率高與成本低的加工特性，因此，本論文選用滾齒加工方法來模擬創成凸狀及凹狀球形螺旋齒輪，進一步分析並探討由滾齒加工所創成之球形螺旋齒輪所組成之齒輪組的接觸特性。首先，本論文建立一把ZN型蝸桿滾齒刀之齒面數學模式，接著依據滾齒加工之創成機構與齒輪原理推導出由此ZN型蝸桿滾齒刀所創成之凸狀及凹狀球形螺旋齒輪之齒面數學模式，並利用所建立之凸狀與凹狀球形螺旋齒輪之齒面數學模式進行後續的電腦模

擬，包括球形齒輪之齒形過切分析(Tooth undercutting analysis)、齒形尖點分析(Tooth pointing analysis)、齒面接觸分析(Tooth contact analysis)及接觸橢圓(Contact ellipses)分析，最後再利用本論文所發展的球形螺旋齒輪有限元素網格產生軟體，自動產生一組於接觸狀態的球形螺旋齒輪組之有限元素接觸模型，接著再使用有限元素商用分析軟體 ABAQUS/Standard 進行球形螺旋齒輪組之應力分析(Stress analysis)。

齒形過切分析探討在何種齒輪設計參數及滾齒加工參數下，凸狀球形螺旋齒輪會發生齒形過切的現象及其齒形過切之發生位置，而齒形尖點分析則探討當凹狀球形齒輪發生齒形尖點時，其所對應的齒輪設計參數及滾齒加工參數，以提供適合的球形齒輪設計參數及加工參數。齒面接觸分析則探討三種配對型式的球形螺旋齒輪組，分別在平行軸及交錯軸組裝，且在具有裝配誤差及理想組裝狀況時之運動誤差、接觸點位置與接觸比。接觸橢圓分析則利用齒面外形法(Surface separation topology method)來探討三種配對型式的球形齒輪組在不同組裝條件下之接觸橢圓的位置、大小與平均長短軸比。此外，應力分析則模擬球形螺旋齒輪組在實際受負載情況時，其可能產生之齒面接觸應力及齒根彎曲應力。

Characteristic Study of Spherical Helical Gears

Student: Li-Chi Chao

Advisor: Dr. Ray-Quan Hsu

Co-Advisor: Dr. Chung-Biau Tsay

Department of Mechanical Engineering

National Chiao Tung University

ABSTRACT

The spherical gear is a new type of gears proposed by Mitome. Geometrically, the spherical gears have two types of gear teeth—convex tooth and concave tooth. The spherical gear sets have three types of mating combinations: convex tooth with concave tooth, convex tooth with convex tooth and convex tooth with spur gear tooth. Different from that of the conventional spur gear set, the spherical gear set is in point contact and allows variable transmission shaft angles and larger axial misalignments without gear interference during the gear drive meshing.

Based on the advantages of the spherical gear, this study proposes a gear by considering the assembly and transmission characteristics of the spherical gear and helical gear, called spherical helical gear. The spherical helical gear has all geometry and transmission characteristics of the spherical gear, while the gear set can also be assembled in crossed axes mounting mode. Therefore, to develop a complete mathematical model of the spherical helical gears with convex and concave teeth can provide further investigation on the manufacturing conditions, transmission characteristics and application limits of the spherical helical gear for industry.

In this study, hobbing method is considered for generation of spherical helical gears with convex and concave teeth due to its high cutting efficiency and low

manufacturing cost. Based on the hobbing generation mechanism and theory of gearing, mathematical models of the spherical helical gears with convex and concave teeth can be developed. Firstly, the surface equation of a ZN-type worm-type hob cutter is derived, and then surface equations of the spherical helical gears with convex tooth and concave teeth cut by the hob cutter can be obtained. Sequentially, the tooth undercutting and tooth pointing condition equations for the convex and concave spherical helical gears are derived by utilizing the developed tooth surface equations of the gears, respectively. Therefore, the limit curves of the tooth non-undercutting of the convex spherical helical gear under different design parameters are investigated, while the Z cross-sections of tooth pointing beginning of the concave spherical helical gear are determined. Moreover, the tooth contact analysis (TCA) method is applied to determine the contact characteristics, such as kinematic errors, contact ratios and contact positions, of the spherical helical gear set with the three mating combinations (convex pinion mating with convex gear, convex pinion mating with concave gear and convex pinion mating with helical gear) and two assembly modes (parallel axes and crossing axes modes). Surface separation topology method is adopted to find the contact ellipses and bearing contacts of the spherical helical gear set, and the average ratio a/b of the major and minor axes of contact ellipses of the spherical helical gear set can also be obtained. Finally, an automatic mesh-generation program of the spherical helical gear sets is developed to investigate the stress analysis of the gear sets by utilizing the commercial FEA package, ABAQUS/Standard. Therefore, the contact and bending stress contours of the spherical helical gear sets under two axes mounting modes and three mating combinations can be determined.

ACKNOWLEDGEMENT(誌謝)

在交通大學機械工程學系博士班五年的學習過程，隨著論文的付梓，即將劃上句點，回顧這段時間以來的點點滴滴，充滿歡樂，也夾雜著些許不捨；歡樂的是有這麼多人填滿我人生的錄影帶，不捨的是即將告別這奮鬥好幾年的戰場，轉往未知的新領域。

本論文能順利完成，幸蒙蔡教授忠杓與徐教授瑞坤的指導與教誨，對於研究的方向、觀念的啟迪、架構的匡正與求學的態度逐一斧正與細細關懷，於此獻上最深的敬意與謝意。此外，論文口試期間，承蒙口試委員顏教授鴻森、宋教授震國、洪教授景華與馮教授展華的鼓勵與疏漏處之指正，使得本論文更臻完備，在此謹深致謝忱。

論文寫作期間，承蒙張老師信良、學長威良、怡呈、家彰、瑞堂、冠宇、政成及煌基提供寶貴的意見；感謝張小姐鴻瑜、好友明達、志榮、陽光與正展的關懷與支持；學弟政豪、俊諭、家誠、宗賢、健育與庚慶的鼎力相助；之灝與之頤為我這五年的研究生涯注入很不一樣的元素。對於所有幫助與關懷過我的人，致上由衷感謝。

外出休閒的時候，可愛女友與小香菇們的賣力演出更填滿了很多我的人生底片，感謝你們這十幾年來的相伴，有了你們的電力，才使得我的博士戰鬥營有持續下去的動力。

另外，可愛女友在背後的默默支持更是我另一個前進的動力，沒有妳的體諒、包容及在生活小細節上的提醒，相信這五年的博士生活將是很慌亂的情況。

最後，特將本文獻給我最敬愛的親人，感謝您們無時無刻的關懷包容與經濟上的支持，讓我能專注於課業研究中，願以此與家人共享。

Jackicy 謹誌於 新竹
中華民國九十九年六月

TABLE OF CONTENTS

摘要.....	i
ABSTRACT	iii
ACKNOWLEDGEMENT(誌謝)	v
TABLE OF CONTENTS	vi
LIST OF TABLES	viii
LIST OF FIGURES	x
NOMENCLATURE	xiv
CHAPTER 1 Introduction	1
1.1 Features of spherical gear.....	1
1.2 Literatures review.....	6
1.3 Motivation.....	8
1.4 Overviews.....	9
CHAPTER 2 Mathematical Model of Spherical Helical Gears	11
2.1 Introduction.....	11
2.2 Mathematical model of the ZN-type worm-type hob cutter.....	13
2.3 Tooth generation of the convex spherical helical gear.....	18
2.3.1 Relationship between hob cutter and convex spherical helical gear.....	18
2.3.2 Equation of meshing for convex spherical helical gears.....	21
2.3.3 Mathematical model of the convex spherical helical gear.....	27
2.4 Tooth generation of the concave spherical helical gear.....	27
2.4.1 Relationship between hob cutter and concave spherical helical gear.....	27
2.4.2 Equation of meshing for concave spherical helical gears.....	30
2.4.3 Mathematical model of concave spherical helical gear.....	36
2.5 Computer graphs of convex and concave spherical helical gears.....	36
2.6 Transverse pitch chord thicknesses of convex, concave and conventional helical gears.....	38
2.7 Remarks.....	39
CHAPTER 3 Tooth Undercutting and Tooth Pointing Analyses	40
3.1 Introduction.....	40
3.2 Tooth undercutting of convex spherical helical gear.....	42
3.3 Tooth pointing of concave spherical helical gear.....	50
3.4 Numerical examples.....	53
3.5 Remarks.....	62
CHAPTER 4 Tooth Contact Analysis	64

4.1	Introduction.....	64
4.2	Meshing model for spherical helical gear set.....	65
4.3	Kinematic errors.....	71
4.4	Contact ratio.....	73
4.5	Contact ellipses.....	73
4.6	Numerical examples.....	78
4.6.1	Spherical helical gear sets under parallel axes mounting mode....	78
4.6.2	Spherical helical gear sets under crossed axes mounting mode....	89
4.7	Remarks.....	98
Chapter 5 Finite Element Stress Analysis.....		101
5.1	Introduction.....	101
5.2	Finite element contact models of spherical helical gear sets.....	102
5.2.1	Processes of establishing FE contact model.....	102
5.2.2	Simplified meshing model of a gear set.....	104
5.2.3	Meshes convergence test and local refined FE model.....	107
5.3	Numerical examples.....	111
5.4	Remarks.....	127
CHAPTER 6 Conclusions and Future Works.....		129
6.1	Conclusions.....	129
6.2	Future works.....	132
REFERENCES.....		134
APPENDIX A Stress distributions of A Spherical Helical Gear Set with Uniform Element Size along Tooth Thickness Direction.....		140
APPENDIX B Stress Distributions of A Conventional Helical Gear Set with Axial Misalignments under Parallel Axes Mounting Mode.....		142

LIST OF TABLES

Table 2.1	Major design parameters of the hob cutter, convex spherical helical pinion and concave spherical helical gear.....	37
Table 2.2	Major design parameters of the hob cutter, convex spherical, concave spherical and conventional helical gears.....	38
Table 3.1	Major design parameters of the hob cutter, convex spherical helical gear.....	54
Table 3.2	The coordinates of left- and right-side tooth profiles of the convex spherical helical gear at $Z_g=0$ mm cross-section.....	55
Table 3.3	The Z_g cross-section of tooth pointing beginning of the concave spherical helical gear under different normal pressure angle α_n	63
Table 3.4	The Z_g cross-section of tooth pointing beginning of the concave spherical helical gear under different gear's lead angle λ_g	63
Table 4.1	Major design parameters of hob cutter, pinion and gear for spherical helical gear sets under parallel axes mounting mode.....	80
Table 4.2	Contact ratios and rotation angles of the spherical helical gear sets under parallel axes mounting mode and two different assembly conditions.....	88
Table 4.3	Average ratio a/b and rotation angles of major and minor axes of contact ellipses of the spherical helical gear sets under parallel axes mounting mode and two different assembly conditions.....	88
Table 4.4	Major design parameters of hob cutter, pinion and gears for spherical helical gear sets under crossed axes mounting mode.....	90
Table 4.5	Contact ratios of the spherical helical gear sets with crossed axes under different assembly conditions.....	98
Table 4.6	Average ratio a/b of major and minor axes of contact ellipses of spherical helical gear sets with crossed axes meshing under different assembly conditions.....	98
Table 5.1	Major design parameters of spherical helical gear set with convex pinion and concave gear under parallel and crossed axes mounting modes.....	104
Table 5.2	Mesh densities of the spherical convex pinion and concave gear.....	108
Table 5.3	Major design parameters of the spherical helical gear sets under parallel axes mounting mode.....	111
Table 5.4	Contact and bending von-Mises stresses of the spherical helical gear set with three types of mating combinations under parallel axes mounting mode at the pinion's beginning rotation angle.....	112

Table 5.5	Major design parameters of the spherical helical gear sets under crossed axes mounting mode.....	120
Table 5.6	Contact and bending von-Mises stresses of the spherical helical gear set with three types of mating combinations under crossed axes mounting mode at the pinion's beginning rotation angle.....	120



LIST OF FIGURES

Fig. 1.1	Mating statuses of spherical gear sets with axial misalignments.....	2
Fig. 1.2	The changes of straight pitch traces in axial section for different types of gears.....	4
Fig. 1.3	The changes of quadratic pitch traces in axial section for different types of gears.....	5
Fig. 2.1	Hobbing locus for spherical helical gear with (a)convex teeth and (b)concave teeth.....	12
Fig. 2.2	Geometric relationships of the straight-edged cutting blade and the ZN-type worm-type hob cutter.....	14
Fig. 2.3	Coordinate systems between the cutting blade and ZN-type worm-type hob cutter.....	16
Fig. 2.4	Generating relationship between hob cutter and convex spherical helical gear.....	19
Fig. 2.5	Coordinate systems between the hob cutter and convex spherical helical gear.....	22
Fig. 2.6	Generating relationship between hob cutter and concave spherical helical gear.....	29
Fig. 2.7	Coordinate systems between the hob cutter and concave spherical helical gear.....	31
Fig. 2.8	Computer graph of the spherical helical gear set with convex pinion and concave gear.....	37
Fig. 2.9	Transverse pitch chord thicknesses of the convex spherical, concave spherical and conventional helical gears.....	39
Fig. 3.1	The phenomenon of tooth undercutting.....	41
Fig. 3.2	The phenomenon of tooth pointing.....	41
Fig. 3.3	Simulation of a generation mechanism with two-parameter motion....	46
Fig. 3.4	Tooth pointing of concave spherical helical gear.....	52
Fig. 3.5	Tooth profile of the convex spherical helical gear with tooth undercutting under different Z_g cross-sections.....	55
Fig. 3.6	Locations of limit curves of the convex spherical helical gear under different number of teeth T_g	56
Fig. 3.7	Locations of limit curves of the convex spherical helical gear under different gear's lead angle λ_g	58
Fig. 3.8	Locations of limit curves of the convex spherical helical gear under different hob cutter's pitch radius r_w	59
Fig. 3.9	Locations of limit curves of the convex spherical helical gear under	

	different normal pressure angle α_n	60
Fig. 3.10	The Z_g cross-sections of tooth pointing beginning of the concave spherical helical gear.....	61
Fig. 4.1	Simulation of meshing for spherical helical gear set with assembly errors.....	66
Fig. 4.2	Relationship among two contact teeth and their common tangent plane.....	68
Fig. 4.3	Mounting relationships of the spherical helical gear set under the crossed axes mounting mode.....	72
Fig. 4.4	Coordinate system relationship of the contact point and tangent plane	75
Fig. 4.5	Schematic diagram for surface topology measurement.....	77
Fig. 4.6	Two axes mounting modes of the spherical helical gear sets.....	79
Fig. 4.7	KEs of the spherical helical gear set with convex pinion and convex gear under parallel axes mounting mode and different assembly conditions.....	81
Fig. 4.8	Contact ellipses and contact loci on tooth surfaces of the spherical helical gear set under parallel axes mounting mode and different assembly conditions.....	81
Fig. 4.9	KEs of the spherical helical gear set with convex pinion and concave gear under parallel axes mounting mode and different assembly conditions.....	84
Fig. 4.10	Contact ellipses and contact loci on tooth surfaces of the spherical helical gear set under parallel axes mounting mode and different assembly conditions.....	84
Fig. 4.11	KEs of the gear set with convex pinion and conventional helical gear under parallel axes mounting mode and different assembly conditions.....	86
Fig. 4.12	Contact ellipses and contact loci on tooth surfaces of the gear set under parallel axes mounting mode and different assembly conditions.....	86
Fig. 4.13	KEs of the spherical helical gear set with convex pinion and convex gear under crossed axes mounting mode and different assembly conditions.....	91
Fig. 4.14	Contact ellipses and contact loci on tooth surfaces of the spherical helical gear set under crossed axes mounting mode and different assembly conditions.....	91
Fig. 4.15	KEs of the spherical helical gear set with convex pinion and concave gear under crossed axes mounting mode and different assembly	93

	conditions.....	
Fig. 4.16	Contact ellipses and contact loci on tooth surfaces of the spherical helical gear set under crossed axes mounting mode and different assembly conditions.....	93
Fig. 4.17	KEs of the gear set with convex pinion and conventional helical gear under crossed axes mounting mode and different assembly conditions.....	96
Fig. 4.18	Contact ellipses and contact loci on tooth surfaces of the gear set under crossed axes mounting mode and different assembly conditions	96
Fig. 5.1	Processes of establishing the FE contact model of a spherical helical gear.....	103
Fig. 5.2	Finite element contact model of a spherical helical gear set with convex pinion and concave gear under parallel axes mounting mode...	105
Fig. 5.3	Finite element contact model of a spherical helical gear set with convex pinion and concave gear under crossed axes mounting mode...	105
Fig. 5.4	Simplified contact model of a gear set with boundary conditions.....	106
Fig. 5.5	Finite element model of the convex spherical helical pinion with different mesh densities.....	108
Fig. 5.6	Convergence test of nodal displacements and bending stresses for the mating of spherical convex pinion and concave gear with four teeth subjected to a torque of 200N-m.....	109
Fig. 5.7	Finite element contact model of the spherical helical gear set with local refined meshes under parallel axes mounting mode.....	110
Fig. 5.8	Finite element contact model of the spherical helical gear set with local refined meshes under crossed axes mounting mode.....	110
Fig. 5.9	von-Mises stress distributions on tooth surfaces of the spherical helical gear set with convex pinion and convex gear under the parallel axes mounting mode and ideal assembly condition.....	113
Fig. 5.10	von-Mises stress distributions on tooth surfaces of the spherical helical gear set with convex pinion and concave gear under the parallel axes mounting mode and ideal assembly condition.....	114
Fig. 5.11	von-Mises stress distributions on tooth surfaces of the spherical helical gear set with convex pinion and conventional helical gear under the parallel axes mounting mode and ideal assembly condition..	115
Fig. 5.12	von-Mises stress distributions on tooth surfaces of the spherical helical gear set with convex pinion and concave gear under the parallel axes mounting mode and axial misalignments.....	117
Fig. 5.13	von-Mises stress distributions on tooth surfaces of the spherical	

	helical gear set with large modified spherical radii under the parallel axes mounting mode and ideal assembly condition.....	119
Fig. 5.14	von-Mises stress distributions on tooth surfaces of the spherical helical gear set with convex pinion and convex gear under crossed axes mounting mode and ideal assembly condition.....	121
Fig. 5.15	von-Mises stress distributions on tooth surfaces of the spherical helical gear set with convex pinion and concave gear under crossed axes mounting mode and ideal assembly condition.....	122
Fig. 5.16	von-Mises stress distributions on tooth surfaces of the spherical helical gear set with convex pinion and conventional helical gear under crossed axes mounting mode and ideal assembly condition.....	123
Fig. 5.17	von-Mises stress distributions on tooth surfaces of the spherical helical gear set with convex pinion and concave gear under crossed axes mounting mode and ideal assembly condition.....	124
Fig. 5.18	von-Mises stress distributions on tooth surfaces of the spherical helical gear set with large modified spherical radii under the parallel axes mounting mode and ideal assembly condition.....	126
Fig. A.1	von-Mises stress distributions on tooth surfaces of the spherical helical gear set with convex pinion and convex gear under the parallel axes mounting mode and ideal assembly condition.....	141
Fig. B.1	von-Mises stress distributions on tooth surfaces of the conventional helical gear set with axial misalignment $\Delta\gamma_v = 0.15^\circ$ under the parallel axes mounting mode.....	143
Fig. B.2	von-Mises stress distributions on tooth surfaces of the conventional helical gear set with axial misalignment $\Delta\gamma_h = 0.1^\circ$ under the parallel axes mounting mode.....	144

NOMENCLATURE

a/b	Ratio of major and minor axes of contact ellipses
b_n	Cutting blade width or normal groove width of the ZN-type worm-type hob cutter, as shown in Figs. 2.2(c) and (d)
d_j	Separation distance measured from common tangent plane to pinion surface ($j=1$) or gear surface ($j=2$), as shown in Fig. 4.5(b)
d_t	Tooth thickness of a tooth top-land, as shown in Fig. 3.4
f_j	Equations of meshing of the convex spherical gear ($j=1, 2$)
g_j	Equations of meshing of the concave spherical gear ($j=1, 2$)
l_a	Shift distance of the ZN-type worm-type hob cutter along its spindle axis, as shown in Figs. 2.5 and 2.7
l_b	Surface parameter of the ZN-type worm-type hob cutter, as shown in Fig. 2.2 (b)
$l_{c,j}$	Shortest distance between hob cutter rotation axis and convex ($j=vex$) and concave ($j=cave$) spherical helical gear rotation axes, as shown in Figs. 2.5 and 2.7
$l_{b,max}$	Upper bounds of the working interval of the ZN-type worm-type hob cutter
$l_{b,min}$	Lower bounds of the working interval of the ZN-type worm-type hob cutter
$l_{x,j}$	Radial feed displacement of the ZN-type worm-type hob cutter for cutting convex ($j=vex$) and concave ($j=cave$) spherical helical gears, as shown in Figs. 2.4(b) and 2.6(b)

$l_{z,j}$	Axial feed displacement of the ZN-type worm-type hob cutter for cutting convex ($j=vex$) and concave ($j=cave$) spherical helical gears, as shown in Figs. 2.4(b) and 2.6(b)
m_c	Contact ratio of the spherical helical gear set
m_n	Normal module of the spherical helical gear
$m_{wg,j}$	Gear ratio between number of thread of hob cutter and number of teeth of convex ($j=vex$) and concave ($j=cave$) spherical helical gears
p_w	Screw parameter of the ZN-type worm-type hob cutter, as shown in Fig. 2.3
$p_{g,j}$	Screw parameter of the generated convex ($j=vex$) and concave ($j=cave$) spherical helical gears
(r, θ_i)	Polar coordinates for contact ellipse measurement, as shown in Fig. 4.5(a)
r_f	Root radius of the ZN-type worm-type hob cutter, as shown in Fig. 2.2(c)
$r_{g,j}$	Pitch radius of the convex ($j=vex$) and concave ($j=cave$) spherical helical gears, as shown in Figs. 2.4(b) and 2.6(b)
r_o	Outside radius of the ZN-type worm-type hob cutter, as shown in Fig. 2.2(c)
r_t	Distance measured from cutting blade tip to the original point O_b of coordinate system S_b of the hob rotation axis, as shown in Fig. 2.2(b)
r_{ti}	Radius of tooth top circle, as shown in Fig. 3.4
r_w	Pitch radius of the ZN-type worm-type hob cutter, as shown in Fig. 2.2(c)
d	Shortest vector measured from the center of the work piece to that of

the hob cutter, as shown in Figs. 2.5 and 2.7

$\mathbf{n}_f^{(j)}$	Unit surface normal vector of pinion ($j=1$) or gear ($j=2$) expressed in fixed coordinate system S_f , as shown in Fig. 4.2
C'	Operational center distance of spherical helical gear set with center distance error, as shown in Fig. 4.1
$H_{g,j}$	Lead of the generated convex ($j=vex$) and concave ($j=cave$) spherical helical gears, as shown in Figs. 2.4(a) and 2.6(a)
$R_{c,j}$	Radius of hobbing locus for convex ($j=vex$) and concave ($j=cave$) spherical helical gear generations, as shown in Figs. 2.4(b) and 2.6(b)
$R_{s,j}$	Spherical radius of convex ($j=vex$) and concave ($j=cave$) spherical helical gears, as shown in Figs. 2.4(b) and 2.6(b)
S_j	Coordinate systems S_j ($j=b, c, f, g, h, m, n, p, q, t, v, w, 1, 2$)
$T_{g,j}$	Number of teeth of the convex ($j=vex$) and concave ($j=cave$) spherical helical gear
T_j	Number of teeth of pinion ($j=1$) and gear ($j=2$)
T_w	Thread of the ZN-type worm-type hob cutter
W	Tooth face width of generated gear
\mathbf{L}_{ij}	3×3 homogenous coordinate transformation matrix for vectors transforming from coordinate system S_j to S_i
\mathbf{M}_{ij}	4×4 homogenous coordinate transformation matrix for position vectors transforming from coordinate system S_j to S_i
\mathbf{N}_j	Surface normal vector expressed in coordinate system S_j ($j=w, q$)
\mathbf{R}_b	Position vector of the straight-line cutting blade expressed in its coordinate system S_b

$\mathbf{R}_f^{(j)}$	Position vectors of pinion ($j=1$) and gear ($j=2$) expressed in fixed coordinate system S_f , as shown in Fig. 4.2
$\mathbf{R}_q^{(g,j)}$	Position vectors of convex ($j=vex$) and concave ($j=cave$) spherical helical gears, as shown in Figs. 2.5 and 2.7
$\mathbf{R}_q^{(w)}$	Position vectors of hob cutter express in coordinate system S_q , as shown in Figs. 2.5 and 2.7
$\mathbf{R}_t^{(j)}$	Position vectors of pinion ($j=1$) and gear ($j=2$), expressed in common tangent plane coordinate system S_t
\mathbf{R}_w	Position vector of the ZN-type worm-type hob cutter expressed in coordinate system S_w
$\mathbf{V}_q^{(g,j)}$	Velocity of generated convex ($j=vex$) and concave ($j=cave$) spherical helical gears expressed in coordinate system S_q
$\mathbf{V}_q^{(w)}$	Velocity of the ZN-type worm-type hob cutter expressed in coordinate system S_q
$\mathbf{V}_q^{(wg)}$	Relative velocity between the ZN-type worm-type hob cutter and generated gear expressed in coordinate system S_q
\mathbf{V}_x	Linear velocity of radial feed motion of the ZN-type worm-type hob cutter, as shown in Figs. 2.4(b) and 2.6(b)
\mathbf{V}_z	Linear velocity of axial feed motion of the ZN-type worm-type hob cutter, as shown in Figs. 2.4(a) and 2.6(a)
α_n	Half-apex blade angle or normal pressure angle of generated gear, as shown in Fig. 2.2(b)
$\beta_g^{(j)}$	Helix angle of pinion ($j=1$) and gear ($j=2$), as shown in Fig. 4.3
δ	Angle measured from axis Z_m to axis Z_n , as shown in Fig. 4.4
δ_c	Cone angle of conical gear, as shown in Fig. 1.2(b)

ε	Angle measured from axis Z_n to axis Z_t , as shown in Fig. 4.4
ϕ'_1	Actual rotation angle of pinion, as shown in Fig. 4.1
ϕ'_{1S}	Pinion's rotation angle of spherical helical gear set at the starting contact point during meshing
ϕ'_2	Actual rotation angle of gear, as shown in Fig. 4.1
ϕ'_{2E}	Gear's rotation angle of spherical helical gear set at the ending contact point during meshing
$\phi_{g,j}$	Rotational angle of the generated convex ($j=vex$) and concave ($j=cave$) spherical helical gear, as shown in Figs. 2.5 and 2.7
ϕ_w	Surface parameter of the ZN-type worm-type hob cutter, as shown Fig. 2.3(b)
$\lambda_{g,j}$	Lead angle of the generated convex ($j=vex$) and concave ($j=cave$) spherical helical gears, as shown in Figs. 2.4(a) and 2.6(a)
$\lambda_g^{(j)}$	Lead angle of pinion ($j=1$) and gear ($j=2$), as shown in Fig. 4.3
λ_w	Lead angle of the ZN-type worm-type hob cutter, as shown in Figs. 2.2(a), 2.4(a) and 2.6(a)
ψ	Spindle rotation angle of the ZN-type worm-type hob cutter, as shown in Figs. 2.5 and 2.7
γ	Cross angle between the ZN-type worm-type hob cutter and work piece rotation axes, as shown in Figs. 2.4(a) and 2.6(a)
γ_o	Cross angle formed by pinion' and gear's rotation axes, as shown in Figs. 4.1 and 4.3
$\mathbf{p}^{(j)}$	Position vector measured from original point O_q of coordinate system S_q to center of hob cutter ($j=w$) or work piece ($j=g$), as shown in Fig. 3.3

$\theta_{s,j}$	Spherical angle of convex ($j=vex$) and concave ($j=cave$) spherical helical gears, as shown Figs. 2.4(b) and 2.6(b)
$\omega_{g,j}$	Angular velocity of the generated convex ($j=vex$) and concave ($j=cave$) spherical helical gears, as shown in Figs. 2.4 and 2.6
$\omega_{s,j}$	Angular velocity from hobbing locus of convex ($j=vex$) and concave ($j=cave$) spherical helical gears
ω_w	Angular velocity rate of the ZN-type worm-type hob cutter, as shown in Figs. 2.1, 2.4(a) and 2.6(a)
ω_l	Angular velocity of pinion ($j=1$) and gear ($j=2$), as shown in Fig. 4.3
$\omega_k^{(w)}$	Angular velocity of the ZN-type worm-type hob cutter express in coordinate system S_k ($k = c, q$)
$\omega_q^{(g,j)}$	Angular velocity of the generated convex ($j=vex$) and concave ($j=cave$) spherical helical gears expressed in coordinate system S_q
ΔC	Center distance error of the spherical helical gear set, as shown in Fig. 4.1
ΔZ	Axial shifted amount of the face width of the spherical helical gear set, as shown in Fig. 4.1
$\Delta\phi'_2$	Kinematic error of spherical helical gear set
$\Delta\phi_{g,j}$	Additional angle of the generated convex ($j=vex$) and concave ($j=cave$) spherical helical gears rotation due to the hob's feed motion, as shown in Figs. 2.4(a) and 2.6(a)
$\Delta\gamma_h$	Horizontal axial misaligned angle of the spherical helical gear set, as shown in Fig. 4.1
$\Delta\gamma_v$	Vertical axial misaligned angle of the spherical helical gear set, as shown in Fig. 4.1

Σ_j

Contact tooth surfaces of pinion ($j=1$) and gear ($j=2$), as shown in Figs. 4.2 and 4.5



CHAPTER 1

Introduction

1.1. Features of spherical gears and spherical helical gears

The spherical gear is a new type of gear proposed by Mitome et al. [1,2]. Geometrically, spherical gears have straight tooth trace and two types of gear teeth—convex teeth and concave teeth. The spherical gear with convex teeth is similar to a part of ball, while the spherical gear with concave teeth looks like a worm gear. Moreover, the spherical gear set has three types of mating combinations: convex teeth with concave teeth, convex teeth with convex teeth and convex teeth with spur gear teeth. The conventional spur gear sets with parallel axes are in line contact [3-5], and thus their kinematic errors are sensitive to the gear axial misalignments. When these gear sets have axial misalignments, tooth edge contact will occur and this results in serious stress concentration, noise and vibration. However, the spherical gear set is in point contact and allows variable shaft angles and larger axial misalignments without gear interference during the gear drive meshing. Therefore, it is a good application by applying the spherical gear set to replace the gear-type coupling [6]. Besides, the spherical gear set also can substitute some application occasions of the conical gear set. Figure 1.1 illustrates three types of mating combinations for the spherical gear sets with axial misalignments. The spherical helical gear is a gear considering the assembly and transmission characteristics of the spherical gear and helical gear. The spherical helical gear has all geometry and transmission characteristics of the spherical gear, and the spherical helical gear set can be assembled in crossing axes mode the same as that of the helical gear set. Therefore, the spherical helical gears also have two types of gear teeth—convex and concave teeth, while the spherical

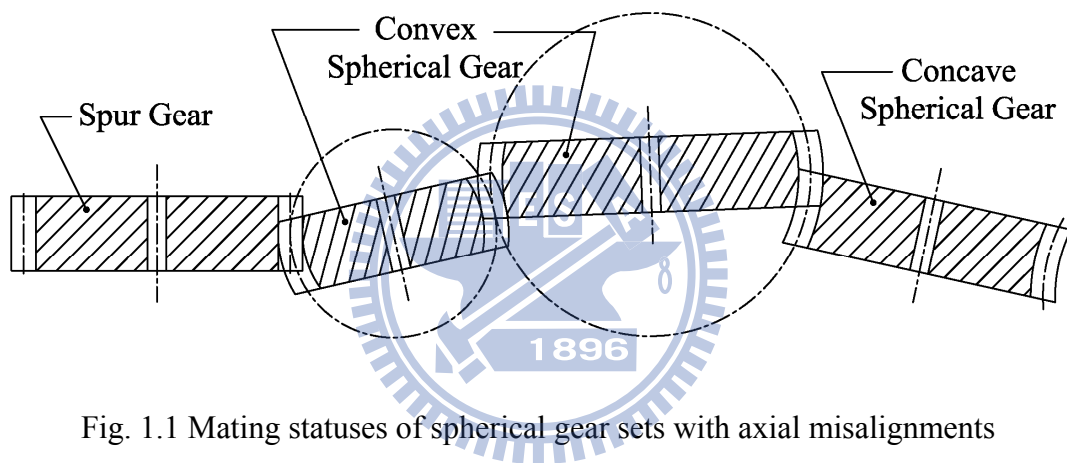
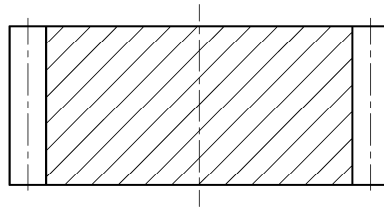


Fig. 1.1 Mating statuses of spherical gear sets with axial misalignments

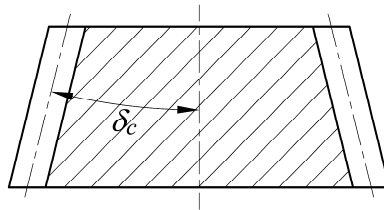
helical gear set also has three types of mating combinations: convex teeth with concave teeth, convex teeth with convex teeth and convex teeth with helical gear teeth.

Figures 1.2(a)-(e) shows five schematic illustrations for the changes of straight pitch traces in the axial section of different gear types. The axial section of a conventional external gear, i.e. spur (helical) gears, is shown in Fig. 1.2(a), and the pitch trace and gear axis are parallel to each other. When the pitch trace of the gear intersects the gear rotation axis with a cone angle δ_c , then this type of gear is called the conical gear, as shown in Fig. 1.2(b). When the pitch trace and the gear rotation axis are perpendicular to each other, then the type of gear is called the face gear, as shown in Fig 1.2(c). If the cone angle δ_c of an internal gear is equal to 180° , the pitch trace and gear rotation axis are parallel to each other, as shown in Fig. 1.2(d), and this type of gear is called the internal spur (helical) gear. While the cone angle δ_c of an internal gear is more than 90° and less than 180° , this type of gear is called the internal conical gear, as shown in Fig. 1.2(e).

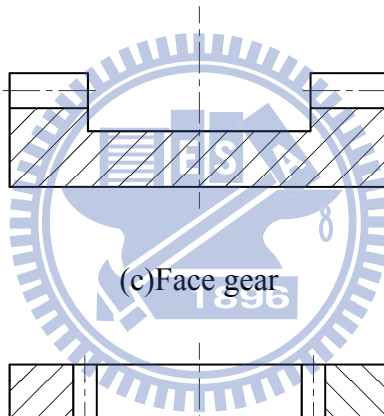
Figures 1.2 shows the gear with linear pitch traces (i.e. straight lines), however, Fig. 1.3 shows the gear with quadratic pitch traces (e.g. arcs). Gears with quadratic pitch traces and convex outward are shown in Figs. 1.3(a) and (b), while gears with quadratic pitch traces and concave outward are illustrated in Figs. 1.3(c) and (d). When the pitch traces of a gear have a quadratic convex outward and form as a circle, this type of gear is called the convex spherical gear, as shown in Fig. 1.3(a). Figure 1.3(b) shows the gear with crowning tooth, and this gear also has a convex outward pitch trace with quadratic form. Whereas, the concave spherical gear has the quadratic pitch trace with concave outward, as shown in Fig. 1.3(c). As shown in Fig. 1.3(d), the worm wheel has the quadratic pitch trace with concave outward, and the radius of the pitch trace is equal to the pitch radius of the worm-type hob cutter.



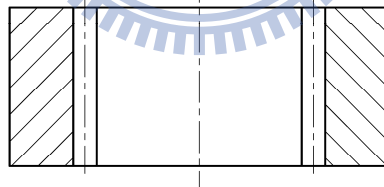
(a) External gear (Spur gear)



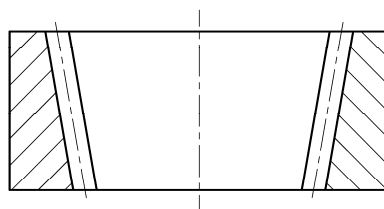
(b) Conical gear



(c) Face gear

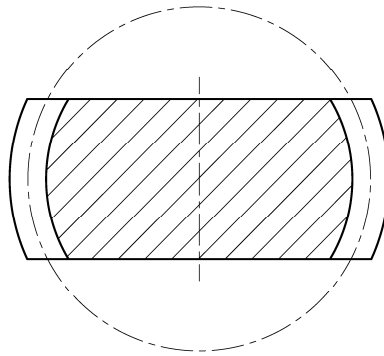


(d) Internal gear

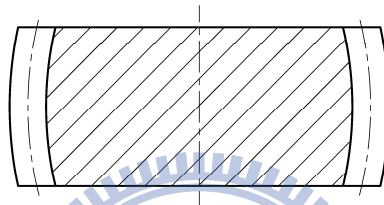


(e) Internal conical gear

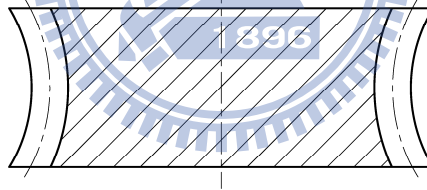
Fig. 1.2 The changes of straight pitch traces in axial section for different types of gears



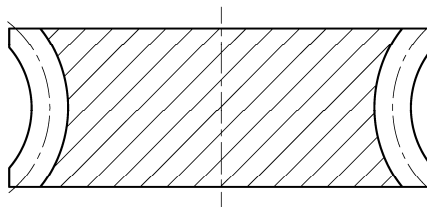
(a)Convex spherical gear



(b)Crowning gear



(c)Concave spherical gear



(d)Worm wheel

Fig. 1.3 The changes of quadratic pitch traces in axial section for different types of gears

1.2. Literatures review

Although the manufacturing method of the spherical gears have been proposed by Mitome [1,2], however, only a few of researches on the spherical gears were performed up to now. Yang [7,8] and Yang et al. [9] proposed a ring-involute-teeth spherical gear with double degrees of freedom. Yang [10] applied the spherical gear with double degrees of freedom to the elbow mechanism. Tsai and Jehng [11] applied a rapid prototyping to manufacture a spherical gear with skew axes. Chao and Tsay [12,13] studied the contact characteristics of the spherical gear set generated by the imaginary rack cutters. Chao and Tsay [14] developed an automatic mesh-generation program to generate the contact model of the spherical gear set cut by two imaginary rack cutters, and investigated the contact and bending stresses of the gear pair by the FEA package ABAQUS/Standard. However, both spherical gears proposed by Yang [7-10] and Tsai [11] are quite different from that proposed in this study neither in generated mechanism, teeth profiles, kinematic characteristics nor meshing model of gear set.

In the past, many studies have been made for spur gears, helical gears, conical gears, noncircular gears, curvilinear cylindrical gears and worm gears, including their respective mathematical models, tooth undercuttings, bearing contacts, stress analyses, manufactures or experiments. Wang and Fong [15] proposed a dual face-hobbing method for the cycloidal spur gears with crowning teeth. Mao [16] simulated the contact situation of a helical gear set, and investigated the reduction of fatigue wear of a spur gear set. Wang and Howard [17] studied the errors analysis of the spur gear drive between the 2-D and 3-D finite element approaches. Moreover, Chen and Tsai [18], and Ganesan and Vijayarangan [19] utilized the finite element method to investigate the involute spur gear by considering the frictional effects. The spur gear is a special case of helical gears with zero degree of helix angle. Tsay [20]

investigated the geometry, computer simulation, tooth contact analysis and stress analysis of the involute helical gear. Litvin et al. [21] simulated the meshing, contact stress and bending stress of the Novikov-Wildhaber helical gears. Chen and Tsay [22] investigated the tooth contact analysis and kinematic optimization of the helical gear pair with an involute pinion and a modified gear. Chen and Tsay [23] also discussed the stress analysis of a helical gear set with localized bearing contacts. Brauer [24] proposed a method to create a general finite element (FE) model for involute helical gears. Colbourne [25] studied the contact stress of the Novikov gear. Moreover, Liu and Tsay [26,27] studied the contact characteristic and tooth undercutting of beveloid gears. Tsai and Chin [28] discussed the surface geometry of bevel gears. Litvin et al. [29] investigated the bevel gears with low-noise and high-endurance by design, manufacture, stress analysis and experimental tests. Litvin et al. [30] applied FEM to investigate the loaded tooth contact analysis (LTCA) of the spiral bevel gear drive. Chang and Tsay [31] studied the tooth profile and undercutting of noncircular gears. Tseng and Tsay [32,33] studied the contact characteristics and tooth undercutting of the cylindrical curvilinear gear generated by two imaginary cutters. Tseng and Tsay [34,35] utilized the ZN-type hob cutter to cut the cylindrical curvilinear gear and enveloped to a two-parameter family of surface by computer simulation. They also investigated the surface deviations and tooth undercutting of the cylindrical curvilinear gear. Besides, Simon [36] discussed the influences of gear hobbing on worm gear characteristics. Janninck [37] proposed the surface separation topology method to simulate contact ellipses for the worm gear drive. Litvin [38] proposed a new geometry of face worm gear drives with conical and cylindrical worms, and investigated their generations, meshings and stress analyses. Fang and Tsay [39] utilized an oversize hob cutter to cut the ZN-type worm gear by computer simulations, and studied the bearing contacts of the ZN-type worm gear drive. Maki and Sakai [40]

proposed a new type of hourglass worm gearing with developable tooth surfaces. Chen and Tsay [41] studied the worm wheel working surfaces of the ZN-type hourglass worm gear set. Simon [42] studied the stress analysis of the double enveloping worm gears by the finite element method. Sun and Hung [43] applied the FE model of simplified gear pair with local refined meshes to investigate 2-D surface contact problem of two deformable bodies. Tsai and Hung [44] applied the finite element model with local refined meshes to investigate 3-D surface contact analysis of two elastically deformable bodies.

1.3. Motivation

The spherical gear is a new type of gear. Based on the advances of the spherical gear, this study proposes a gear by considering the assembly and transmission characteristics of the spherical gear and helical gear, called the spherical helical gear. The spherical helical gear has all geometry and transmission characteristics of the spherical gear, and the spherical helical gear set can be assembled in crossing axes mode which is the same as that of the helical gear set. Moreover, the hobbing method is considered for the generation of spherical helical gears due to its high cutting efficiency and low manufacturing cost. However, the cutting mechanism of a 5-axis CNC hobbing machine with multiple degrees of freedom may result in complex tooth surfaces because of the envelope surfaces of two-parameter family [45]. In this study, a complete mathematical model of the spherical helical gear with envelope surfaces of two-parameter family cut by the ZN-type worm-type hob cutter is developed firstly. Then the tooth undercutting and tooth pointing of the spherical helical gear and the contact situations of the spherical helical gear set under two assembly modes (parallel axes and crossing axes modes) and three mating combinations (convex tooth with convex tooth, convex tooth with concave tooth and convex tooth with helical gear

tooth) are also investigated. These contact situations, including kinematic errors, contact ratio, contact locus, dimension and orientation of contact ellipses, and contact and bending stress contours, are also investigated.

1.4. Overviews

This study totally includes six chapters. Chapter 1 is the introduction to the contents that contains the feature of the spherical helical gears, literatures reviews and motivation of this study.

In Chapter 2, the mathematical model for the ZN-type worm-type hob cutter surfaces have been developed. According to the theory of gearing and generating mechanism of the CNC hobbing machine, the motions between the hob cutter and work piece, and the mathematical models for the convex and concave spherical helical gears can be obtained. Moreover, a 3-D computer graph of the spherical helical gear set with convex pinion and concave gear has been plotted by using the computer aided drawing technique.

In Chapter 3, the condition equations of tooth undercutting and tooth pointing of the spherical helical gears are derived by utilizing the developed surface equations of the gears. Therefore, the limit curves of the tooth non-undercutting and tooth non-pointing of the spherical helical gears under different design parameters can be determined.

In Chapter 4, the tooth contact analysis (TCA) method is applied to develop the tooth surface meshing model of the spherical helical gear set. The tooth surface meshing model includes assembly errors of the horizontal axial misalignment, vertical axial misalignment, axial shift along on the face width and the center distance error. Based on the developed tooth meshing model, the contact characteristics of the spherical helical gear set, under two axes (parallel and crossed axes) mounting modes

and three mating combinations (convex teeth with convex teeth, convex teeth with concave teeth and convex tooth with helical gear teeth), such as kinematic errors (KEs), contact ratios and contact loci can be obtained. The contact ellipses of the spherical helical gear sets can be obtained by using the TCA results and the surface separation topology method. Moreover, several numerical examples are presented to discuss the influences of the assembly errors on kinematic errors, contact ratios and contact ellipses of the spherical helical gear sets under two axes mounting modes and three mating combinations.

In Chapter 5, the contact and bending stress contours of the proposed spherical helical gear sets are investigated by using the commercial FEA package, ABAQUS/Standard. Firstly, an automatic mesh-generation program is developed to generate the finite element contact model of the spherical helical gear sets by considering the developed surface equations of the gear sets. Therefore, an input file for ABAQUS/Standard computation is generated automatically by the developed mesh-generation program. Some numerical examples are presented to demonstrate the tooth stress with different gear design parameters.

Chapter 6 concludes the proposal by summarizing the accomplished works in Chapters 2 and 3, and the future works for the advanced study.

CHAPTER 2

Mathematical Model of Spherical Helical Gears

2.1 Introduction

Hobbing is an economical method for gear manufacturing due to its versatility and high cutting efficiency. Hobbing method can be employed to generate various types of gears such as spur, helical, conical and worm gears. A hob cutter with straight-edged normal section can be used to generate the involute spur and helical gears. Different tooth profiles can be generated on the same CNC hobbing machine by changing the profile of hob cutters. However, the hobbing method is complicated since the gear generating motion is a multi-degree of freedom. Therefore, the method of two-parameter family envelope surfaces can be used to simulate hobbing process.

Since the spherical helical gear is hobbled by a ZN-type worm-type hob cutter in this study, the convex and concave spherical helical gears can be considered as hobbing a helical gear with its hobbing path of positive or negative continuous hob shiftings in a quadric form, shifting from both sides of the tooth face width to its middle section, respectively [12,13]. Figure 2.1 shows two hobbing loci for hobbing the convex (Fig. 2.1(a)) and concave (Fig. 2.1(b)) spherical helical gears. Where the direction of positive profile shifting is defined as the direction outward the generated gear, whereas the direction of negative profile shifting is defined as the direction inward the generated gear. Moreover, compared with the standard tooth profile of a helical gear, the tooth profiles of the convex spherical helical gear at both ends of tooth face width have negative profile shifting, whereas the concave spherical helical gear has positive profile shifting at its both ends of tooth face width. Again, the hobbing path of a spherical helical gear is generated by hobbing a cylinder with a

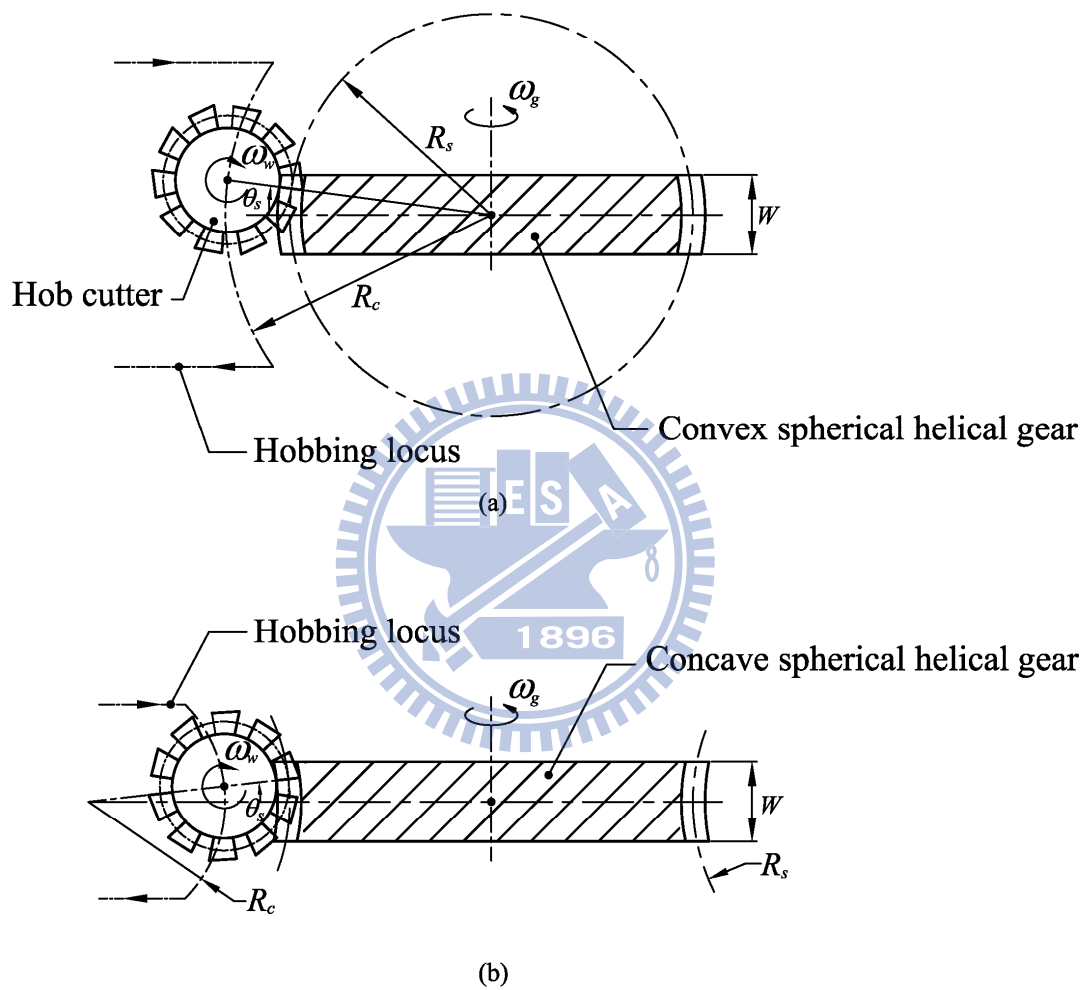


Fig. 2.1 Hobbing locus for spherical helical gear with (a)convex teeth and (b)concave teeth

quadric form of continuous profile shifting (i.e. an arc) along the gear rotation axis instead of a straight line for the generation of the conventional helical gear.

In this chapter, the mathematical model of the ZN-type worm-type hob cutter is derived firstly. Then the tooth surface equations of the convex and concave spherical helical gears are developed based on the generating mechanism of the CNC hobbing machine, the ZN-type worm-type hob cutter, and the theory of gearing.

2.2 Mathematical model of the ZN-type worm-type hob cutter

The normal profile of the ZN-type worm-type hob cutter is widely used for the gear manufacturing, and it is much more easier to manufacture a hob cutter with its normal section profile as a straight-lined shape. Therefore, a right-handed ZN-type worm-type hob cutter is used to simulate the manufacture of spherical helical gears in this study.

The tooth surfaces of the hob cutter can be generated by a blade with the straight-lined shape, performing a screw motion with respect to the rotational axis of hob cutter. The cutting blade is installed on the normal section to the groove of the ZN-type worm, as shown in Fig. 2.2(a). The design parameter λ_w is the lead angle of the worm. Figure 2.2(b) illustrates the normal section of a cutting blade that is rigidly connected to the coordinate system $S_b(X_b, Y_b, Z_b)$, and the cutting blade is formed by two straight lines. The blade's half apex angle α_n is formed by the straight-lined of the blade and X_b -axis, as shown in Fig. 2.2(b). Moreover, the distance l_b measured from the initial point M_0 , moving along the straight line $\overline{M_0M_1}$, to any point M_1 is also a design parameter of the cutting blade. Therefore, the equation of the straight-line cutting blade can be represented in coordinate system S_b as follows:

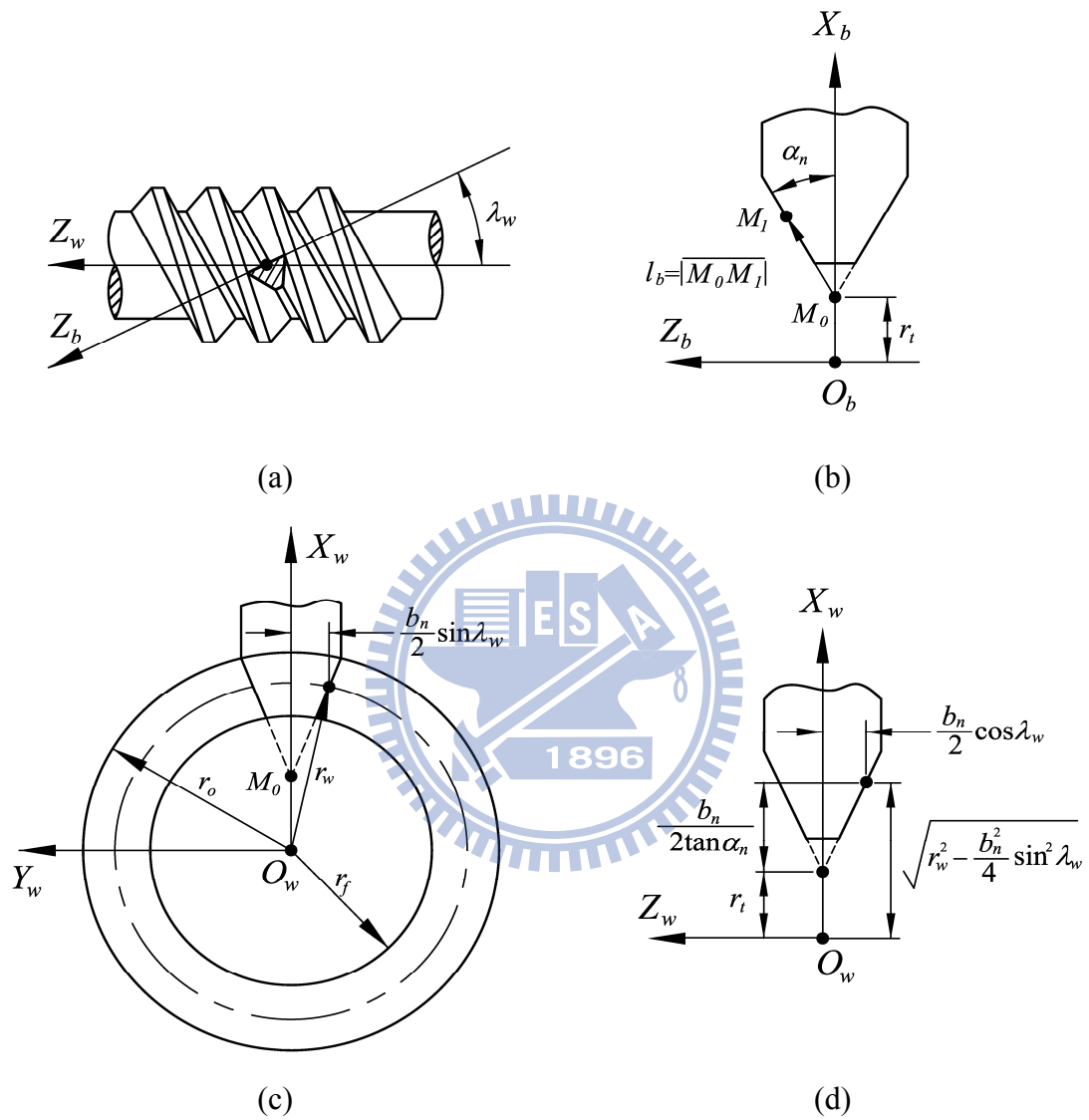


Fig. 2.2 Geometric relationships of the straight-edged cutting blade and the ZN-type worm-type hob cutter

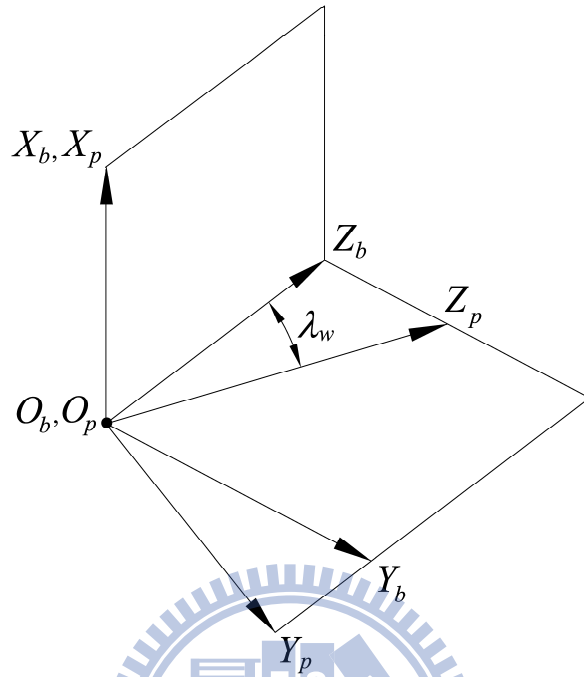
$$\mathbf{R}_b = \begin{bmatrix} r_t + l_b \cos \alpha_n \\ 0 \\ \pm l_b \sin \alpha_n \\ 1 \end{bmatrix}, \quad (2.1)$$

where the upper “±” sign represents the left-side cutting blade, while the lower sign indicates the right-side cutting blade.

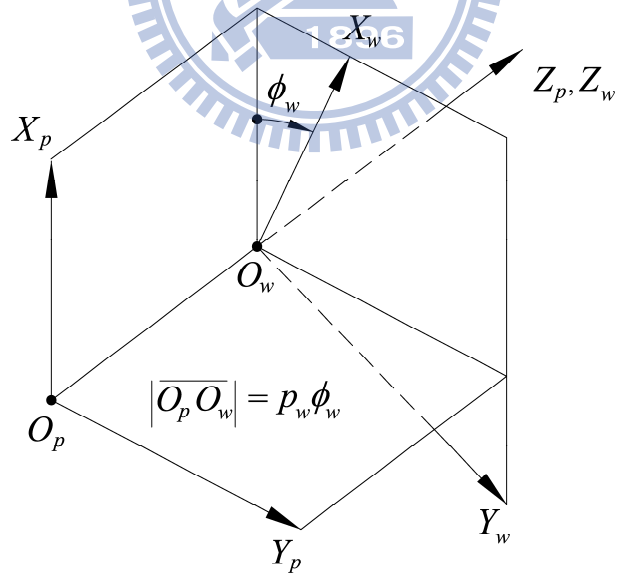
Figure 2.2(c) shows the relationship between the cutting blade and the ZN-type worm-type hob cutter represented in the normal section of hob cutter’s rotation axis. Symbols r_o , r_f and r_w express the outside radius, root radius and pitch radius of the ZN-type worm-type hob cutter, respectively. The cutting blade width b_n equals the normal groove width of the hob cutter, and the design parameter r_t can be obtained from the geometric relationship, as shown in Figs. 2.2(c) and (d) as follows:

$$r_t = \sqrt{r_w^2 - \frac{b_n}{4} \sin^2 \lambda_w} - \frac{b_n}{2 \tan \alpha_n}. \quad (2.2)$$

Figure 2.3 shows the relations among coordinate systems $S_b(X_b, Y_b, Z_b)$, $S_p(X_p, Y_p, Z_p)$ and $S_w(X_w, Y_w, Z_w)$, where coordinate system S_b is the blade coordinate system, coordinate system S_w is rigidly connected to the hob cutter, and coordinate system S_p is the auxiliary reference coordinate system. Axes Z_b and Z_p form an angle λ_w that is equal to the lead angle on the worm pitch cylinder, as shown in Fig. 2.3(a). Figure 2.3(b) shows that the movable coordinate system S_w performs a screw motion with respect to the auxiliary reference coordinate system S_p along the rotational axis of the hob cutter rotating through an angle ϕ_w . Therefore, the locus equation of the cutting blade can be represented in coordinate system S_w by applying the following homogeneous coordinate transformation matrix equation, transforming from coordinate system S_b to S_w :



(a) Relationship between coordinate systems S_b and S_p



(b) Relationship between coordinate systems S_p and S_w

Fig. 2.3 Coordinate systems between the cutting blade and ZN-type worm-type hob cutter

$$\mathbf{R}_w(l_b, \phi_w) = \mathbf{M}_{wp} \mathbf{M}_{pb} \mathbf{R}_b = \begin{bmatrix} (r_t + l_b \cos \alpha_n) \cos \phi_w \mp l_b \sin \alpha_n \sin \phi_w \sin \lambda_w \\ -(r_t + l_b \cos \alpha_n) \sin \phi_w \mp l_b \sin \alpha_n \cos \phi_w \sin \lambda_w \\ \pm l_b \sin \alpha_n \cos \lambda_w - p_w \phi_w \\ 1 \end{bmatrix}, \quad (2.3)$$

where

$$\mathbf{M}_{pb} = \begin{bmatrix} 1 & 0 & 0 & 0 \\ 0 & \cos \lambda_w & -\sin \lambda_w & 0 \\ 0 & \sin \lambda_w & \cos \lambda_w & 0 \\ 0 & 0 & 0 & 1 \end{bmatrix},$$

and

$$\mathbf{M}_{wp} = \begin{bmatrix} \cos \phi_w & \sin \phi_w & 0 & 0 \\ -\sin \phi_w & \cos \phi_w & 0 & 0 \\ 0 & 0 & 1 & -p_w \phi_w \\ 0 & 0 & 0 & 1 \end{bmatrix},$$

where, symbol p_w represents the screw parameter of the ZN-type worm-type hob cutter. In Eq. (2.3), symbols l_b and ϕ_w are surface parameters of the hob cutter, and the upper “ \pm ” sign represents the left-side surface of the hob cutter, while the lower sign indicates the right-side surface of the hob cutter. Since the working interval of the ZN-type worm-type hob cutter must be limited between the outside radius r_o and root radius r_f of the worm, the upper and lower bounds of the design parameter l_b can be limited by

$$l_{b,max} = \frac{\sqrt{(r_o^2 - r_t^2) \sin^2 \alpha_n \sin^2 \beta_w + r_o^2 \cos^2 \alpha_n} - r_t \cos \alpha_n}{\sin^2 \alpha_n \sin^2 \beta_w + \cos^2 \alpha_n}, \quad (2.4)$$

$$\text{and } l_{b,min} = \frac{\sqrt{(r_f^2 - r_t^2) \sin^2 \alpha_n \sin^2 \beta_w + r_f^2 \cos^2 \alpha_n} - r_t \cos \alpha_n}{\sin^2 \alpha_n \sin^2 \beta_w + \cos^2 \alpha_n}, \quad (2.5)$$

respectively.

The surface normal vector \mathbf{N}_w of the hob cutter can be obtained and expressed

in coordinate system S_w as follows:

$$\mathbf{N}_w = \frac{\partial \mathbf{R}_w}{\partial l_b} \times \frac{\partial \mathbf{R}_w}{\partial \phi_w}, \quad (2.6)$$

where

$$\frac{\partial \mathbf{R}_w}{\partial l_b} = \begin{bmatrix} \cos \alpha_n \cos \phi_w \mp \sin \alpha_n \sin \phi_w \sin \lambda_w \\ -\cos \alpha_n \sin \phi_w \mp \sin \alpha_n \cos \phi_w \sin \lambda_w \\ \pm \sin \alpha_n \cos \lambda_w \end{bmatrix},$$

$$\text{and } \frac{\partial \mathbf{R}_w}{\partial \phi_h} = \begin{bmatrix} -(r_t + l_b \cos \alpha_n) \sin \phi_w \mp l_b \sin \alpha_n \cos \phi_w \sin \lambda_w \\ -(r_t + l_b \cos \alpha_n) \cos \phi_w \pm l_b \sin \alpha_n \sin \phi_w \sin \lambda_w \\ -P_w \end{bmatrix}.$$

Again, the upper “ \pm ” sign in Eq. (2.6) represents the left-side surface of the hob cutter, while the lower sign indicates the right-side surface of the hob cutter.

2.3 Tooth generation of the convex spherical helical gear

2.3.1 Generating relationship between hob cutter and convex spherical helical gear

Figure 2.4 depicts the generating relationship between hob cutter and work piece of the convex spherical helical gear. Axes Z_w and Z_g are the rotation axis of the hob cutter and the work piece with angular velocities ω_w and ω_g , respectively, and these two axes form an angle γ called the crossing angle. The crossing angle is synthesized by the lead angles of the hob cutter λ_w and the convex spherical helical gear $\lambda_{g,vex}$ (i.e. $\gamma = \lambda_w + \lambda_{g,vex}$). Moreover, point O_w denotes the rotational center of the hob cutter’s swivel, and point O_g is the center of the work piece. In Fig. 2.4(a), the common the hob cutter and the work piece are in tangency at point P . During the hobbing process, the center of hob cutter is moving along the hobbing locus with the linear axial and radial feeding velocities \mathbf{V}_x and \mathbf{V}_z , as shown in Fig. 2.4. Moreover, the

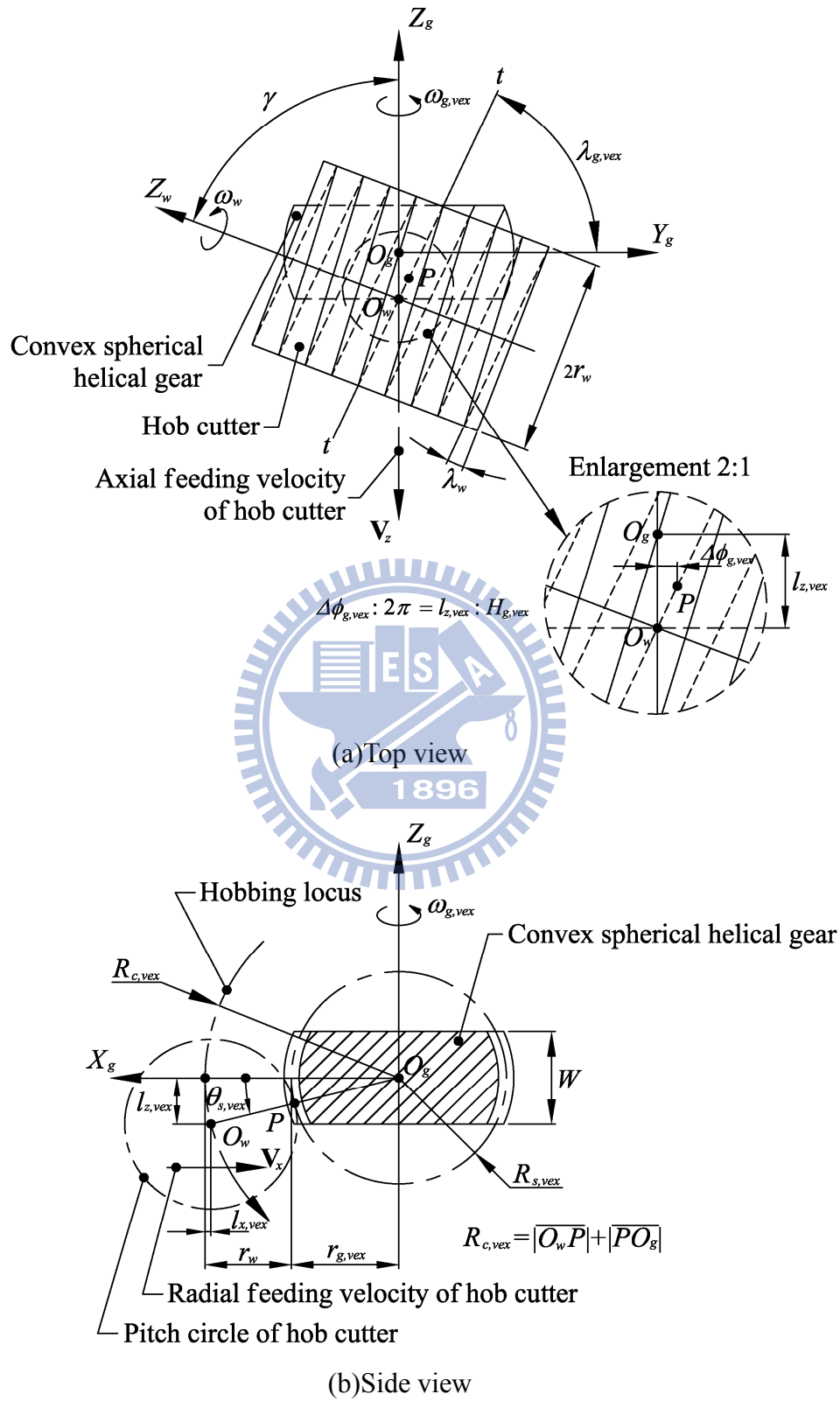


Fig. 2.4 Generating relationship between hob cutter and convex spherical helical gear

tangent to both hob cutter and work piece is $t-t$, and the operating pitch cylinders of axial and radial feeding displacements of the hob cutter are designed as $l_{z,vex}$ and $l_{x,vex}$, respectively, and they are related by the following equations:

$$l_{z,vex} = R_{c,vex} \sin \theta_{s,vex}, \quad (2.7)$$

$$\text{and } l_{x,vex} = R_{c,vex} (1 - \cos \theta_{s,vex}), \quad (2.8)$$

where symbol $R_{c,vex}$ denotes the cutting radius, and symbol $\theta_{s,vex}$ indicates the spherical angle for the convex spherical helical gear. According to Fig. 2.4(b), the cutting radius $R_{c,vex}$ can be synthesized by the spherical radius $R_{s,vex}$ and the pitch radius r_w of the hob cutter for the convex spherical helical gear generation as follows:

$$R_{c,vex} = R_{s,vex} + r_w. \quad (2.9)$$

According to Fig. 2.4(a), the rotation angles of the hob cutter and the work piece can be related as follows:

$$\phi_{g,vex} = m_{wg,vex} \psi + \Delta \phi_{g,vex}, \quad (2.10)$$

where symbol $m_{wg,vex} = \frac{T_w}{T_{g,vex}}$, while symbols T_w and $T_{g,vex}$ denote the number of threads of the hob cutter and number of teeth of the convex spherical helical gear, respectively. Symbols $\phi_{g,vex}$ and ψ indicate the rotational angles of the work piece and the spindle of the hob cutter, respectively. Symbol $\Delta \phi_{g,vex}$ expresses the additional angle of the work piece (convex spherical helical gear) due to the generated gear with a helix angle. According to Fig. 2.4(a), the ratio of axial feeding displacement $l_{z,vex}$ to the lead $H_{g,vex}$ of the generated convex spherical helical gear is equal to that of the additional angle $\Delta \phi_{g,vex}$ to a rotation cycle (i.e. 2π) of the gear. Therefore, the

additional angle $\Delta\phi_{g,vex}$ for the convex spherical helical gear can be expressed by

$$\Delta\phi_{g,vex} = \frac{l_{z,vex}}{p_{g,vex}}, \quad (2.11)$$

where symbol $p_{g,vex} = H_{g,vex} / 2\pi$ represents the screw parameter of the convex spherical helical gear.

2.3.2 Equation of meshing for convex spherical helical gears

Figure 2.5 illustrates the schematic relationships among coordinate systems $S_w(X_w, Y_w, Z_w)$, $S_c(X_c, Y_c, Z_c)$, $S_q(X_q, Y_q, Z_q)$ and $S_g(X_g, Y_g, Z_g)$ for the generation mechanism of the convex spherical helical gear. Coordinate systems S_w and S_g are attached to the hob cutter and convex spherical helical gear, respectively. Coordinate system S_c is an auxiliary coordinate system to describe the hob cutter's rotational motion with a rotational angle ψ , which coordinate system S_q is an auxiliary fixed coordinate system attached to the housing of a CNC hobbing machine. Moreover, symbol $\phi_{g,vex}$ is the rotational angle of the generated gear (i.e. convex spherical helical gear). According to Fig. 2.5, the homogenous coordinate transformation matrices \mathbf{M}_{cw} , \mathbf{M}_{qc} and \mathbf{M}_{gq} can be expressed as follows:

$$\mathbf{M}_{cw} = \begin{bmatrix} \cos\psi & -\sin\psi & 0 & 0 \\ \sin\psi & \cos\psi & 0 & 0 \\ 0 & 0 & 1 & l_{a,vex} \\ 0 & 0 & 0 & 1 \end{bmatrix}, \quad (2.12)$$

$$\mathbf{M}_{qc} = \begin{bmatrix} -1 & 0 & 0 & l_{c,vex} - l_{x,vex} \\ 0 & -\cos\gamma & -\sin\gamma & 0 \\ 0 & -\sin\gamma & \cos\gamma & l_{z,vex} \\ 0 & 0 & 0 & 1 \end{bmatrix}, \quad (2.13)$$

and

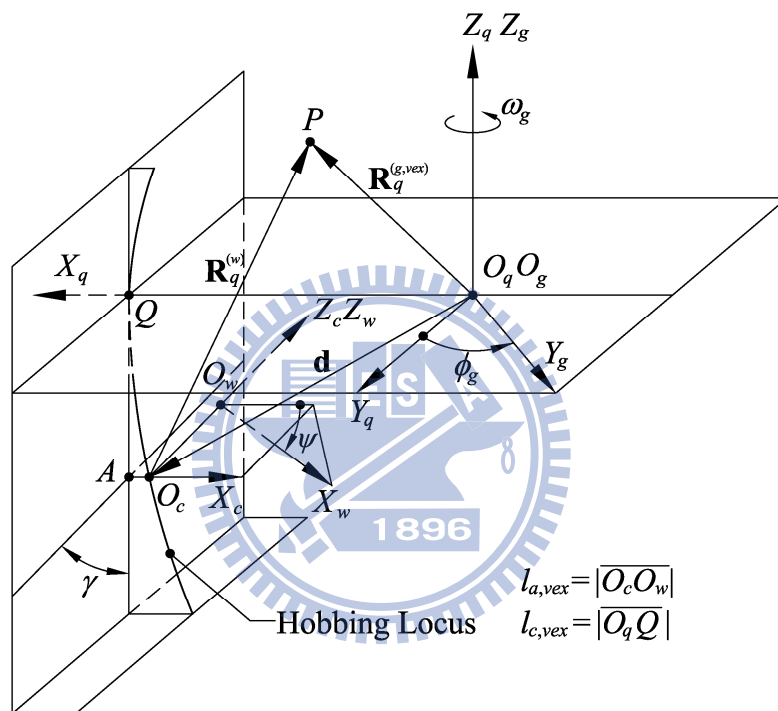


Fig. 2.5 Coordinate systems between the hob cutter and convex spherical helical gear

$$\mathbf{M}_{gq} = \begin{bmatrix} \cos \phi_{g,vex} & \sin \phi_{g,vex} & 0 & 0 \\ -\sin \phi_{g,vex} & \cos \phi_{g,vex} & 0 & 0 \\ 0 & 0 & 1 & 0 \\ 0 & 0 & 0 & 1 \end{bmatrix}, \quad (2.14)$$

where symbol $l_{a,vex} = \overline{O_c O_w}$ is the axial displacement of the hob cutter, while symbol $l_{c,vex} = \overline{O_q Q}$ is the distance between points O_q and Q . Moreover, the feeding displacements $l_{z,vex}$ and $l_{x,vex}$ of the hob cutter are expressed in Eqs. (2.7) and (2.8), respectively.

In Fig. 2.5, point P denotes an instantaneous common point to the hob cutter and work piece (convex spherical helical gear) during a hobbing process. Therefore, surface coordinates $\mathbf{R}_q^{(g,vex)}$ of the work piece can be determined by transforming the hob's surface from coordinate system S_w into the fixed coordinate system S_q as follows:

$$\mathbf{R}_q^{(g,vex)} = \mathbf{M}_{qc} \mathbf{M}_{cw} \mathbf{R}_w = [x_q \ y_q \ z_q \ 1]^T, \quad (2.15)$$

where symbols x_q , y_q and z_q are the X , Y and Z components of the hob cutter's surface $\mathbf{R}_q^{(g,vex)}$ repressed in coordinate system S_q , respectively. Therefore, the velocity $\mathbf{V}_q^{(g,vex)}$ at point P of the work piece can be obtained by

$$\mathbf{V}_q^{(g,vex)} = \boldsymbol{\omega}_q^{(g,vex)} \times \mathbf{R}_q^{(g,vex)} = [-y_q \omega_{g,vex} \ x_q \omega_{g,vex} \ 0]^T, \quad (2.16)$$

where $\boldsymbol{\omega}_q^{(g,vex)} = \omega_{g,vex} \mathbf{k}_q$ denotes the angular velocity of the work piece expressed in the fixed coordinate system S_q . Differentiating Eq. (2.10) with respect to time, the relationship among angular velocities $\omega_{g,vex}$, ω_w and $\omega_{s,vex}$ can be obtained as follows:

$$\omega_{g,vex} = \frac{d\phi_{g,vex}}{dt} = m_{wg,vex} \omega_w + \frac{R_{c,vex} \cos \theta_{s,vex}}{P_{g,vex}} \omega_{s,vex}, \quad (2.17)$$

where symbol $\omega_w = \frac{d\psi}{dt}$ indicates the angular velocity of the hob cutter, while symbol $\omega_{s,vex} = \frac{d\theta_s}{dt}$ denotes the angular velocity of hob cutter's generating motion along the hobbing locus (see Fig. 2.4(b)). Equation (2.17) indicates the rotation angle $\omega_{g,vex}$ of work piece (convex spherical helical gear) in terms of two independent variables ω_w and $\omega_{s,vex}$.

Similarly, the velocity at point P that attached to the hob cutter, $\mathbf{V}_q^{(w)}$, can be obtained as follows:

$$\mathbf{V}_q^{(w)} = \boldsymbol{\omega}_q^{(w)} \times \mathbf{R}_q^{(w)} + \mathbf{V}_x + \mathbf{V}_z, \quad (2.18)$$

where \mathbf{V}_x and \mathbf{V}_z express the linear velocity of axial and radial feeding motion, and $\boldsymbol{\omega}_q^{(w)}$ indicates the angular velocity of the hob cutter expressed in the fixed coordinate system S_q , as follows:

$$\boldsymbol{\omega}_q^{(w)} = \mathbf{L}_{qc} \boldsymbol{\omega}_c^{(w)} = [0 \quad -\omega_w \sin \gamma \quad \omega_w \cos \gamma]^T, \quad (2.19)$$

where the matrix \mathbf{L}_{qc} can be expressed as:

$$\mathbf{L}_{qc} = \begin{bmatrix} -1 & 0 & 0 \\ 0 & -\cos \gamma & -\sin \gamma \\ 0 & -\sin \gamma & \cos \gamma \end{bmatrix}.$$

The surface coordinate of the hob cutter $\mathbf{R}_q^{(w)}$ can be obtained by

$$\mathbf{R}_q^{(w)} = \mathbf{R}_q^{(g,vex)} - \mathbf{d}, \quad (2.20)$$

where symbol \mathbf{d} denotes the shortest vector measured from the center of the work piece to that of the hob cutter, and it can be expressed by

$$\mathbf{d} = [l_{c,vex} - l_{x,vex} \quad 0 \quad l_{z,vex}]^T. \quad (2.21)$$

Substituting Eqs. (2.15) and (2.21) into Eq. (2.20), the surface coordinates of point P of the hob cutter can be determined as follows:

$$\mathbf{R}_q^{(w)} = [x_q - l_{c,vex} + l_{x,vex} \quad y_q \quad z_q - l_{z,vex}]^T. \quad (2.22)$$

Differentiating Eqs. (2.7) and (2.8) with respect to time, the linear velocities of axial and radial feeding motion \mathbf{V}_z and \mathbf{V}_x can be expressed as follows:

$$\mathbf{V}_z = -\frac{dl_{z,vex}}{dt} \mathbf{k}_q = -\omega_{s,vex} R_{c,vex} \cos \theta_{s,vex} \mathbf{k}_q, \quad (2.23)$$

$$\text{and } \mathbf{V}_x = \frac{dl_{x,vex}}{dt} \mathbf{i}_q = \omega_{s,vex} R_{c,vex} \sin \theta_{s,vex} \mathbf{i}_q, \quad (2.24)$$

where $\omega_{s,vex} = \frac{d\theta_{s,vex}}{dt}$. Substituting Eqs. (2.19) and (2.22)~(2.24) into Eq. (2.18), the velocity of the hob cutter expressed in coordinate system S_g , $\mathbf{V}_q^{(w)}$, can be obtained as follows:

$$\mathbf{V}_q^{(w)} = \begin{bmatrix} (l_{z,vex} - z_q) \omega_w \sin \gamma - y_q \omega_w \cos \gamma + \omega_{s,vex} R_{c,vex} \sin \theta_{s,vex} \\ (x_q - l_{c,vex} + l_{x,vex}) \omega_w \cos \gamma \\ (x_q - l_{c,vex} + l_{x,vex}) \omega_w \sin \gamma - \omega_{s,vex} R_{c,vex} \cos \theta_{s,vex} \end{bmatrix}. \quad (2.25)$$

Therefore, the relative velocity $\mathbf{V}_q^{(wg)}$ of the hob cutter and work piece at their common contact point P can be represented in the fixed coordinate system S_q as follows:

$$\begin{aligned} \mathbf{V}_q^{(wg)} &= \mathbf{V}_q^{(w)} - \mathbf{V}_q^{(g,vex)} \\ &= \begin{bmatrix} (l_{z,vex} - z_q) \sin \gamma - y_q (\cos \gamma - m_{wg,vex}) \\ (x_q - l_{c,vex} + l_{x,vex}) \cos \gamma - x_q m_{wg,vex} \\ (x_q - l_{c,vex} + l_{x,vex}) \sin \gamma \end{bmatrix} \omega_w + \begin{bmatrix} R_{c,vex} (\sin \theta_{s,vex} + y_q \cos \theta_{s,vex} / p_{g,vex}) \\ -x_q R_{c,vex} \cos \theta_{s,vex} / p_{g,vex} \\ -R_{c,vex} \cos \theta_{s,vex} \end{bmatrix} \omega_{s,vex}. \end{aligned} \quad (2.26)$$

According to the theory of gearing [3-5], the common surface normal \mathbf{N}_q of the tool surface and the work piece is perpendicular to their of relative velocity $\mathbf{V}_q^{(wg)}$ at the instantaneous common contact point. Therefore, the equation of meshing between the hob cutter surface and the convex spherical helical gear surface can be obtained by

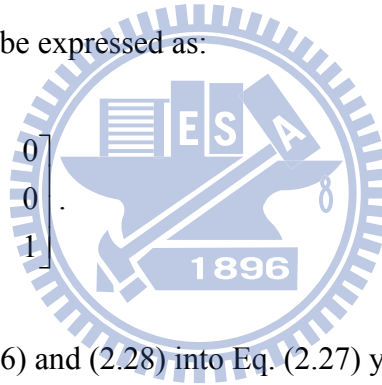
$$\mathbf{N}_q \cdot \mathbf{V}_q^{(wg)} = 0 \quad (2.27)$$

where the surface normal \mathbf{N}_q can be obtained by using the following homogenous coordinate transformation matrix equation:

$$\mathbf{N}_q = \mathbf{L}_{qc} \mathbf{L}_{cw} \mathbf{N}_w, \quad (2.28)$$

where the matrix \mathbf{L}_{cw} can be expressed as:

$$\mathbf{L}_{cw} = \begin{bmatrix} \cos \psi & -\sin \psi & 0 \\ \sin \psi & \cos \psi & 0 \\ 0 & 0 & 1 \end{bmatrix}.$$



Substituting Eqs. (2.6), (2.26) and (2.28) into Eq. (2.27) yields:

$$\begin{aligned} & \{[(l_{z,vex} - z_p) \sin \gamma - y_q (\cos \gamma - m_{wg,vex})] \omega_w + [R_{c,vex} (\sin \theta_{s,vex} + y_q \cos \theta_{s,vex} / p_{g,vex})] \omega_{s,vex}\} N_{qx} \\ & + \{[(x_q - l_{c,vex} + l_{x,vex}) \cos \gamma - x_q m_{wg,vex}] \omega_w - (x_q R_{c,vex} \cos \theta_{s,vex} / p_{g,vex}) \omega_{s,vex}\} N_{qy} \\ & + \{[(x_q - l_{c,vex} + l_{x,vex}) \sin \gamma] \omega_w - (R_{c,vex} \cos \theta_{s,vex}) \omega_{s,vex}\} N_{qz} = 0, \end{aligned} \quad (2.29)$$

where symbols N_{qx} , N_{qy} and N_{qz} are the X , Y and Z components of the surface normal vector \mathbf{N}_q , respectively. Rearranging Eq. (2.29) in terms of the independent of variables, ω_w and $\omega_{s,vex}$, yields the following equation:

$$\begin{aligned} & \{[(l_{z,vex} - z_q) \sin \gamma - y_q (\cos \gamma - m_{wg,vex})] N_{qx} + [(x_q - l_{c,vex} + l_{x,vex}) \cos \gamma - x_q m_{wg,vex}] N_{qy} \\ & + [(x_q - l_{c,vex} + l_{x,vex}) \sin \gamma] N_{qz}\} \omega_w + [R_{c,vex} (\sin \theta_{s,vex} + y_p \cos \theta_{s,vex} / p_{g,vex}) N_{qx} \\ & - (x_q R_{c,vex} \cos \theta_{s,vex} / p_{g,vex}) N_{qy} - (R_{c,vex} \cos \theta_{s,vex}) N_{qz}] \omega_{s,vex} = 0. \end{aligned} \quad (2.30)$$

Since ω_w and $\omega_{s,vex}$ are independent variables, two equations of meshing that relate the

hob cutter's surface parameters and the cutting motion parameters can be obtained as follows:

$$\begin{aligned}
 f_1(l_b, \phi_w, \psi, \theta_{s,vex}) &= [(l_{z,vex} - z_q) \sin \gamma - y_q (\cos \gamma - m_{wg,vex})] N_{qx} \\
 &+ [(x_q - l_{c,vex} + l_{x,vex}) \cos \gamma - x_q m_{wg,vex}] N_{qy} \\
 &+ [(x_q - l_{c,vex} + l_{x,vex}) \sin \gamma] N_{qz} = 0,
 \end{aligned} \tag{2.31}$$

and

$$\begin{aligned}
 f_2(l_b, \phi_w, \psi, \theta_{s,vex}) &= R_{c,vex} (\sin \theta_{s,vex} + y_q \cos \theta_{s,vex} / p_{g,vex}) N_{qx} \\
 &- (x_q R_{c,vex} \cos \theta_{s,vex} / p_{g,vex}) N_{qy} - (R_{c,vex} \cos \theta_{s,vex}) N_{qz} = 0.
 \end{aligned} \tag{2.32}$$

2.3.3 Mathematical model of the convex spherical helical gear

According to Fig. 2.5, surface locus of the hob cutter, expressed in coordinate system S_g , can be obtained by applying the following homogenous coordinate transformation matrix equation:

$$\mathbf{R}_g = \mathbf{M}_{gq} \mathbf{M}_{qc} \mathbf{M}_{cw} \mathbf{R}_w. \tag{2.33}$$

where the homogenous coordinate transformation matrices \mathbf{M}_{cw} , \mathbf{M}_{qc} and \mathbf{M}_{gq} are expressed in Eqs. (2.12)~(2.14), respectively.

Based on the theory of gearing [3-5], the mathematical model of the generated gear is the combination of equation of meshing and the surface locus of hob cutter. Therefore, the mathematical model of the convex spherical helical gear can be obtained by considering Eqs. (2.31)~(2.33), simultaneously.

2.4 Tooth generation of the concave spherical helical gear

2.4.1 Relationship between hob cutter and concave spherical helical gear

Figure 2.6 illustrates the generating relationship between the hob cutter and work

piece of the concave spherical helical gear. The rotational axes Z_w and Z_g of the hob cutter and work piece have the angular velocities ω_w and ω_g , respectively. The crossing angle γ is the included angle between axes Z_w and Z_g . Moreover, points O_w and O_g denote the rotational center of hob's swivel and the center of work piece, respectively. The hob's moves along the hobbing locus, as shown in Fig. 2.6, during the gear generation process. In Fig. 2.6(a), the operating pitch cylinders of hob cutter and work piece are in tangency at point P on the common tangent $t-t$. Similarly to that of section 2.3.1, the axial and radial feeding displacements of hob cutter for the generating of concave spherical helical gear are also designed as $l_{z,cave}$ and $l_{x,cave}$:

$$l_{z,cave} = R_{c,cave} \sin \theta_{s,cave}, \quad (2.34)$$

$$\text{and } l_{x,cave} = R_{c,cave} (1 - \cos \theta_{s,cave}), \quad (2.35)$$

where symbols $R_{c,cave}$ and $\theta_{s,cave}$ indicate the cutting radius and spherical angle of the concave spherical helical gear, respectively. According to Fig. 2.6(b), the cutting radius $R_{c,cave}$ can be determined by

$$R_{c,cave} = R_{s,cave} - r_w, \quad (2.36)$$

where symbols $R_{s,cave}$ and r_w denote the spherical radius of the concave spherical helical and pitch radius of the hob cutter, respectively.

Similar to the deriving process of the convex spherical helical gear (see subsection 2.3.1) and according to Fig. 2.6, the relationship between the concave spherical helical and hob cutter rotation angles, and the additional angle $\Delta\phi_{g,cave}$ for the concave spherical helical gear can be expressed by:

$$\phi_{g,cave} = m_{wg,cave} \psi + \Delta\phi_{g,cave}, \quad (2.37)$$

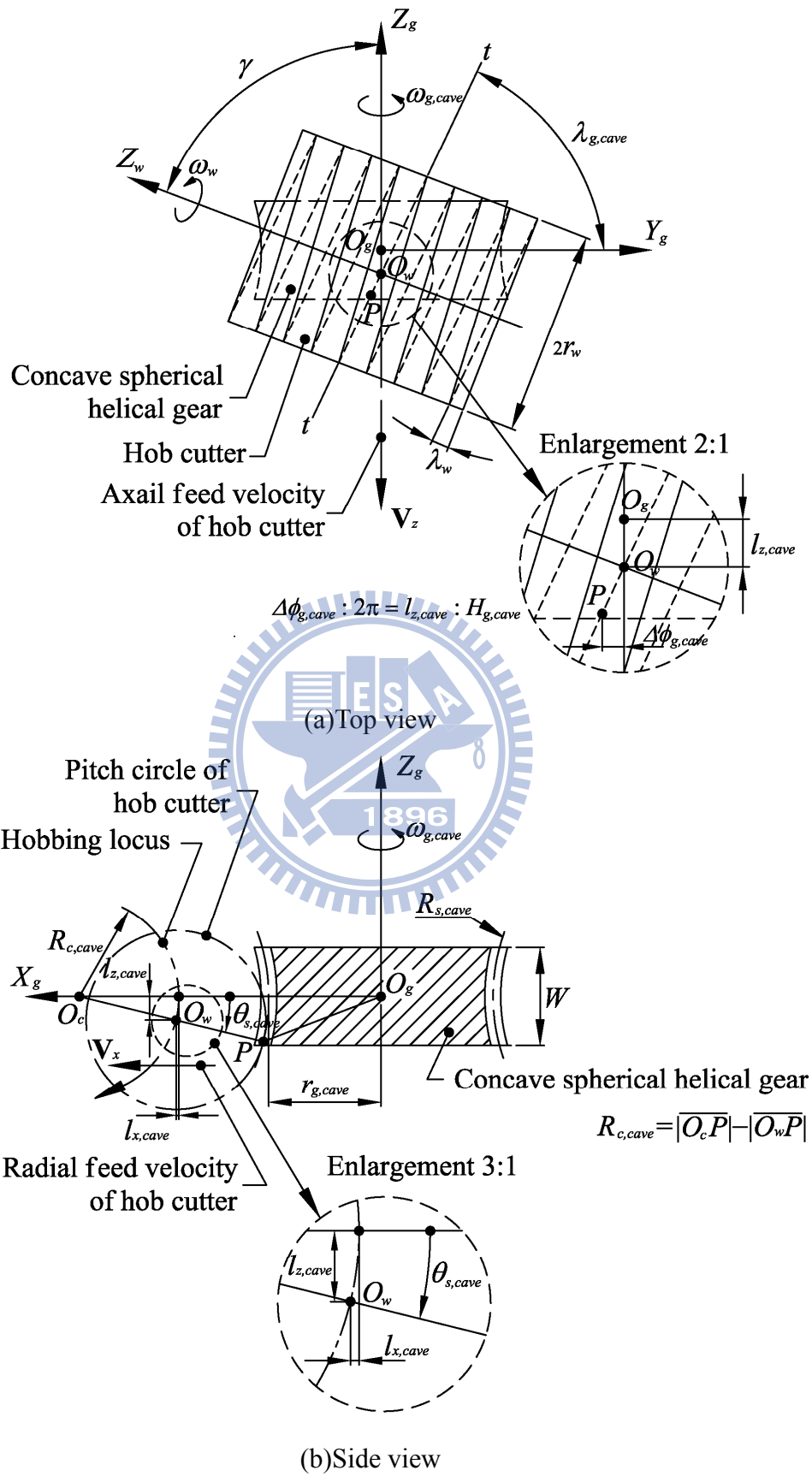


Fig. 2.6 Generating relationship between hob cutter and concave spherical helical gear

$$\text{and } \Delta\phi_{g,cave} = \frac{l_{z,cave}}{p_{g,cave}}, \quad (2.38)$$

where symbol $m_{wg,cave} = \frac{T_w}{T_{g,cave}}$ of Eq. (2.37) is the gear ratio, while symbol $p_{g,cave} = H_{g,cave} / 2\pi$ of Eq. (2.38) indicates the screw parameter of the generated gear. Again, the additional angle $\Delta\phi_{g,cave}$ indicates the work piece (concave spherical helical gear) due to the generated gear with a helix angle.

2.4.2 Equation of meshing for concave spherical helical gears

Figure 2.7 shows a schematic relationship of coordinate systems $S_w(X_w, Y_w, Z_w)$, $S_c(X_c, Y_c, Z_c)$, $S_q(X_q, Y_q, Z_q)$ and $S_g(X_g, Y_g, Z_g)$ for the generation mechanism of concave spherical helical gears. Coordinate systems S_w and S_g are attached to the hob cutter and concave spherical helical gear, respectively. The rotation motion of the hob cutter is expressed by considering an auxiliary coordinate system S_c with a rotational angle ψ . Coordinate system S_q is the fixed coordinate system attached to the machine housing. Moreover, symbol $\phi_{g,cave}$ is the rotational angle of the generated gear (e.g. concave spherical helical gear). Therefore, the homogenous coordinate transformation matrices \mathbf{M}_{cw} , \mathbf{M}_{qc} and \mathbf{M}_{gq} can be expressed as follows:

$$\mathbf{M}_{cw} = \begin{bmatrix} \cos \psi & -\sin \psi & 0 & 0 \\ \sin \psi & \cos \psi & 0 & 0 \\ 0 & 0 & 1 & l_{a,cave} \\ 0 & 0 & 0 & 1 \end{bmatrix}, \quad (2.39)$$

$$\mathbf{M}_{qc} = \begin{bmatrix} -1 & 0 & 0 & l_{c,cave} + l_{x,cave} \\ 0 & -\cos \gamma & -\sin \gamma & 0 \\ 0 & -\sin \gamma & \cos \gamma & l_{z,cave} \\ 0 & 0 & 0 & 1 \end{bmatrix}, \quad (2.40)$$

and

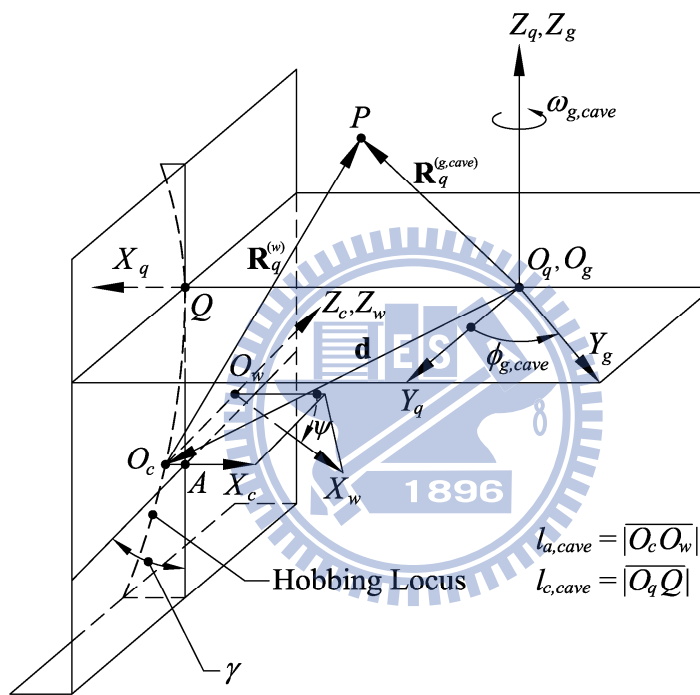


Fig. 2.7 Coordinate systems between the hob cutter and concave spherical helical gear

$$\mathbf{M}_{gq} = \begin{bmatrix} \cos \phi_{g,cave} & \sin \phi_{g,cave} & 0 & 0 \\ -\sin \phi_{g,cave} & \cos \phi_{g,cave} & 0 & 0 \\ 0 & 0 & 1 & 0 \\ 0 & 0 & 0 & 1 \end{bmatrix}, \quad (2.41)$$

where symbol $l_{a,cave} = \overline{O_c O_w}$ is the axial displacement of the hob cutter, while symbol $l_{c,cave} = \overline{O_q Q}$ is the distance between points O_q and Q . Moreover, the feeding displacements $l_{z,cave}$ and $l_{x,cave}$ of the hob cutter are expressed in Eqs. (2.34) and (2.35), respectively.

In Fig. 2.7, point P is a common contact point of the hob cutter and work piece. Therefore, the surface coordinates $\mathbf{R}_q^{(g,cave)}$ of the work piece can be determined by transforming the hob's surface from coordinate system S_w into the fixed coordinate system S_q as follows:

$$\mathbf{R}_q^{(g,cave)} = \mathbf{M}_{qc} \mathbf{M}_{cw} \mathbf{R}_w = [x_q \quad y_q \quad z_q \quad 1]^T. \quad (2.42)$$

The velocity at point P of the work piece can be obtained by:

$$\mathbf{V}_q^{(g,cave)} = \boldsymbol{\omega}_q^{(g,cave)} \times \mathbf{R}_q^{(g,cave)} = [-y_q \omega_{g,cave} \quad x_q \omega_{g,cave} \quad 0]^T, \quad (2.43)$$

where $\boldsymbol{\omega}_q^{(g,cave)} = \omega_{g,cave} \mathbf{k}_q$ denotes the angular velocity of the work piece (concave spherical helical gear) expressed in the fixed coordinate system S_q . Differentiating Eq. (2.37) with respect to time, the relationship among angular velocities $\omega_{g,cave}$, ω_w and $\omega_{s,cave}$ can be obtained as follows:

$$\omega_{g,cave} = \frac{d\phi_{g,cave}}{dt} = m_{wg,cave} \omega_w + \frac{R_{c,cave} \cos \theta_{s,cave}}{P_{g,cave}} \omega_{s,cave}, \quad (2.44)$$

where symbols $\omega_w = \frac{d\psi}{dt}$ and $\omega_s = \frac{d\theta_{s,cave}}{dt}$ indicate the angular velocities of hob

cutter and hob cutter's generating motion along the hobbing locus (see Fig. 2.6), respectively. Equation (2.44) indicates the rotation angle $\omega_{g,cave}$ of work piece (concave spherical helical gear) in terms of angular velocities ω_w and $\omega_{s,cave}$.

Similarly, the velocity at point P that attached to the hob cutter can be obtained as follows:

$$\mathbf{V}_q^{(w)} = \boldsymbol{\omega}_q^{(w)} \times \mathbf{R}_q^{(w)} + \mathbf{V}_x + \mathbf{V}_z, \quad (2.45)$$

where \mathbf{V}_x and \mathbf{V}_z express the linear velocities of axial and radial feeding motion, and $\boldsymbol{\omega}_q^{(w)}$ indicates the angular velocity of the hob cutter expressed in the fixed coordinate system S_q , as follows:

$$\boldsymbol{\omega}_q^{(w)} = \mathbf{L}_{qc} \boldsymbol{\omega}_c^{(w)} = [0 \quad -\omega_w \sin \gamma \quad \omega_w \cos \gamma]^T, \quad (2.46)$$

where the matrix \mathbf{L}_{qc} can be expressed as:

$$\mathbf{L}_{qc} = \begin{bmatrix} -1 & 0 & 0 \\ 0 & -\cos \gamma & -\sin \gamma \\ 0 & -\sin \gamma & \cos \gamma \end{bmatrix}.$$

The surface coordinate of the hob cutter $\mathbf{R}_q^{(w)}$ can be obtained by

$$\mathbf{R}_q^{(w)} = \mathbf{R}_q^{(g,cave)} - \mathbf{d}, \quad (2.47)$$

where symbol \mathbf{d} denote the shortest vector measured from the center of the work piece to that of the hob cutter, and it can be expressed by

$$\mathbf{d} = [l_{c,cave} + l_{x,cave} \quad 0 \quad l_{z,cave}]^T. \quad (2.48)$$

Substituting Eqs. (2.42) and (2.48) into Eq. (2.47), the surface coordinates of the hob

cutter can be determined as follows:

$$\mathbf{R}_q^{(w)} = [x_q - l_{c,cave} - l_{x,cave} \quad y_q \quad z_q - l_{z,cave}]^T. \quad (2.49)$$

Differentiating Eqs. (2.34) and (2.35) with respect to time, the linear velocities of axial and radial feeding motions \mathbf{V}_z and \mathbf{V}_x can be determined by parameters of spherical angle $\theta_{s,cave}$, cutting radius $R_{c,cave}$ and angular velocity $\omega_{s,cave}$ as follows:

$$\mathbf{V}_z = -\frac{dl_{z,cave}}{dt} \mathbf{k}_q = -\omega_{s,cave} R_{c,cave} \cos \theta_{s,cave} \mathbf{k}_q, \quad (2.50)$$

$$\text{and } \mathbf{V}_x = -\frac{dl_{x,cave}}{dt} \mathbf{i}_q = -\omega_{s,cave} R_{c,cave} \sin \theta_{s,cave} \mathbf{i}_q. \quad (2.51)$$

Substituting Eqs. (2.46) and (2.49)~(2.51) into Eq. (2.45), the velocity $\mathbf{V}_q^{(w)}$ can be determined and simplified as follows:

$$\mathbf{V}_q^{(w)} = \begin{bmatrix} (l_{z,cave} - z_q) \omega_w \sin \gamma - y_q \omega_w \cos \gamma - \omega_{s,cave} R_{c,cave} \sin \theta_{s,cave} \\ (x_q - l_{c,cave} - l_{x,cave}) \omega_w \cos \gamma \\ (x_q - l_{c,cave} - l_{x,cave}) \omega_w \sin \gamma - \omega_{s,cave} R_{c,cave} \cos \theta_{s,cave} \end{bmatrix}. \quad (2.52)$$

Therefore, the relative velocity $\mathbf{V}_q^{(wg)}$ of the hob cutter and work piece at their common contact point P can be represented in the fixed coordinate system S_q as follows:

$$\begin{aligned} \mathbf{V}_q^{(wg)} &= \mathbf{V}_q^{(w)} - \mathbf{V}_q^{(g,cave)} \\ &= \begin{bmatrix} (l_{z,cave} - z_q) \sin \gamma - y_q (\cos \gamma - m_{wg,cave}) \\ (x_q - l_c - l_x) \cos \gamma - x_q m_{wg,cave} \\ (x_q - l_{c,cave} - l_{x,cave}) \sin \gamma \end{bmatrix} \omega_w - \begin{bmatrix} R_{c,cave} (\sin \theta_{s,cave} - y_q \cos \theta_{s,cave} / p_{g,cave}) \\ x_q R_{c,cave} \cos \theta_{s,cave} / p_{g,cave} \\ R_{c,cave} \cos \theta_{s,cave} \end{bmatrix} \omega_{s,cave}. \end{aligned} \quad (2.53)$$

The equation of meshing of hob cutter and convex spherical helical gear can be

obtained by

$$\mathbf{N}_q \cdot \mathbf{V}_q^{(wg)} = 0, \quad (2.54)$$

where the surface normal \mathbf{N}_q can be obtained by using the following homogenous coordinate transformation matrix equation:

$$\mathbf{N}_q = \mathbf{L}_{qc} \mathbf{L}_{cw} \mathbf{N}_w, \quad (2.55)$$

where the matrix \mathbf{L}_{cw} can be expressed as:

$$\mathbf{L}_{cw} = \begin{bmatrix} \cos \psi & -\sin \psi & 0 \\ \sin \psi & \cos \psi & 0 \\ 0 & 0 & 1 \end{bmatrix}.$$

Substituting Eqs. (2.6), (2.55) and (2.53) into Eq. (2.54) yields:

$$\begin{aligned} & \{[(l_{z,cave} - z_p) \sin \gamma - y_q (\cos \gamma - m_{wg,cave})] \omega_w - R_{c,cave} (\sin \theta_{s,cave} - y_q \cos \theta_{s,cave} / p_{g,cave}) \omega_{s,cave}\} N_{qx} \\ & + \{[(x_q - l_{c,cave} - l_{x,cave}) \cos \gamma - x_q m_{wg,cave}] \omega_w - (x_q R_{c,cave} \cos \theta_{s,cave} / p_{g,cave}) \omega_{s,cave}\} N_{qy} \\ & + \{[(x_q - l_{c,cave} - l_{x,cave}) \sin \gamma] \omega_w - (R_{c,cave} \cos \theta_{s,cave}) \omega_{s,cave}\} N_{qz} = 0, \end{aligned} \quad (2.56)$$

where symbols N_{qx} , N_{qy} and N_{qz} are the X , Y and Z components of the surface normal vector \mathbf{N}_q , respectively. Rearranging Eq. (2.56) in terms of the independent of variables, ω_w and $\omega_{s,cave}$, yields the following equation:

$$\begin{aligned} & \{[(l_{z,cave} - z_q) \sin \gamma - y_q (\cos \gamma - m_{wg,cave})] N_{qx} + [(x_q - l_{c,cave} - l_{x,cave}) \cos \gamma - x_q m_{wg,cave}] N_{qy} \\ & + [(x_q - l_{c,cave} - l_{x,cave}) \sin \gamma] N_{qz}\} \omega_w + [-R_{c,cave} (\sin \theta_{s,cave} - y_p R_{c,cave} \cos \theta_{s,cave} / p_{g,cave}) N_{qx} \\ & - (x_q R_{c,cave} \cos \theta_{s,cave} / p_{g,cave}) N_{qy} - (R_{c,cave} \cos \theta_{s,cave}) N_{qz}] \omega_{s,cave} = 0. \end{aligned} \quad (2.57)$$

Since ω_w and $\omega_{s,cave}$ are independent variables, two equations of meshing that relative the hob cutter's surface parameters and the cutting motion parameters can be obtained as follows:

$$\begin{aligned}
g_1(l_b, \phi_w, \psi, \theta_{s,cave}) &= [(l_{z,cave} - z_q) \sin \gamma - y_q (\cos \gamma - m_{wg,cave})] N_{qx} \\
&+ [(x_q - l_{c,cave} - l_{x,cave}) \cos \gamma - x_q m_{wg,cave}] N_{qy} \\
&+ [(x_q - l_{c,cave} - l_{x,cave}) \sin \gamma] N_{qz} = 0,
\end{aligned} \tag{2.58}$$

and

$$\begin{aligned}
g_2(l_b, \phi_w, \psi, \theta_{s,cave}) &= -R_{c,cave} (\sin \theta_{s,cave} - y_q \cos \theta_{s,cave} / p_{g,cave}) N_{qx} \\
&- (x_q R_{c,cave} \cos \theta_{s,cave} / p_{g,cave}) N_{qy} - (R_{c,cave} \cos \theta_{s,cave}) N_{qz} = 0.
\end{aligned} \tag{2.59}$$

2.4.3 Mathematical model of the concave spherical helical gear

According to Fig. 2.7, the surface locus of the hob cutter, expressed in the generated concave spherical helical gear's coordinate system S_g , can be obtained by applying the homogenous coordinate transformation matrix equation:

$$\mathbf{R}_g = \mathbf{M}_{gq} \mathbf{M}_{qc} \mathbf{M}_{cw} \mathbf{R}_w. \tag{2.60}$$

where the homogenous coordinate transformation matrices \mathbf{M}_{cw} , \mathbf{M}_{qc} and \mathbf{M}_{gq} are expressed in Eqs. (2.39)-(2.41), respectively.

Therefore, the mathematical model of the generated gear is the combination of equation of meshing and the surface locus of hob cutter. Therefore, the mathematical model of the concave spherical helical gear can be obtained by considering Eqs. (2.58)~(2.60), simultaneously.

2.5 Computer graphs of convex and concave spherical helical gears

The mathematical model of the convex spherical helical gear is expressed in Eqs. (2.31)~(2.33), while the mathematical model for the concave spherical helical gear is represented in Eqs. (2.58)~(2.60). Table 2.1 summarizes some major design parameters of the hob cutter, convex pinion and concave gear. According to the developed mathematical models of the convex and concave spherical helical gears,

the tooth surfaces of the generated spherical helical gear can be plotted by using the developed computer programs. Therefore, a 3-D computer graph of the spherical helical gear set with convex pinion and concave gear can be plotted as shown in Fig. 2.8.

Table 2.1 Major design parameters of the hob cutter, convex spherical helical pinion and concave spherical helical gear

	Hob cutter	Convex pinion	Concave gear
Normal module, m_n (mm/tooth)	4	4	4
Number of teeth, T_g	1	33	47
Normal pressure angle, α_n (deg.)	20	20	20
Lead angle λ_w, λ_g (deg.)	3.823 RH	75 RH	75 LH
Face width, W (mm)	-	20	20
Pitch radius, r_g (mm)	30	68.328	97.316
Spherical radius, R_s (mm)	-	68.328	97.316
Cutting radius, R_c (mm)	-	98.328	67.316

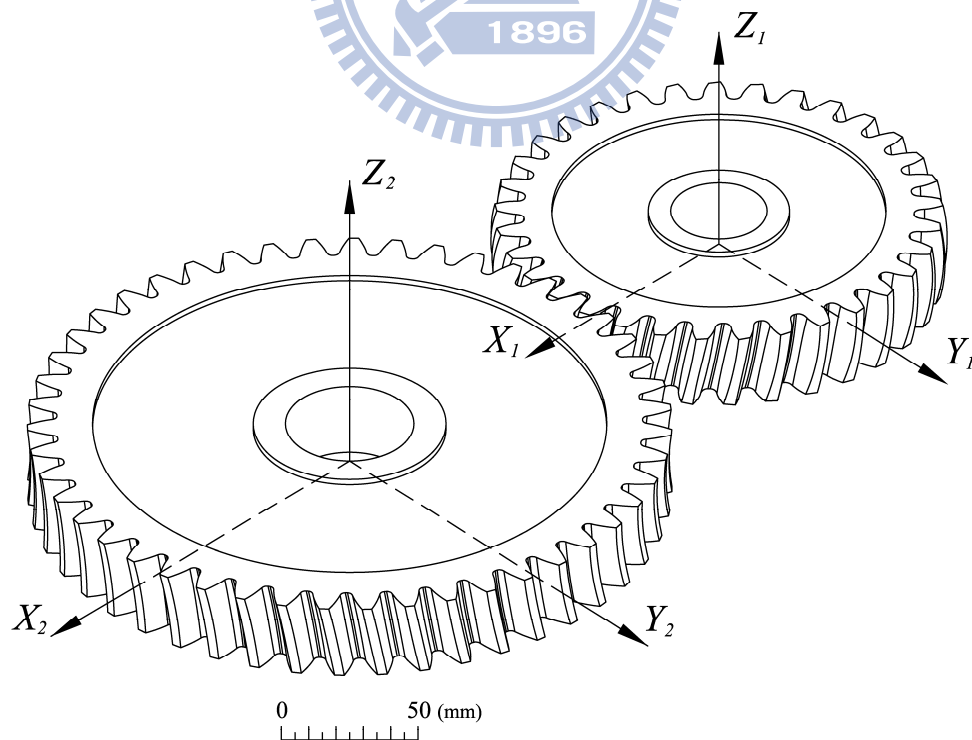


Fig. 2.8 Computer graph of the spherical helical gear set with convex pinion and concave gear

2.6 Transverse pitch chord thicknesses of convex, concave and conventional helical gears

Since the convex and concave spherical helical gears are considered as hobbing a conventional helical gears with continuous positive and negative profile shiftings from both end sides of face width of the gears to their middle sections, respectively, the working pitch circles of the gears are different under every Z-axis cross-section of face width of the gears. Thus the pitch chord thicknesses of the convex and concave spherical helical gears are different at every Z-axis cross-section of face width of the gears. According to the gears' design parameters of Table 2.2, Fig. 2.9 illustrates the transverse pitch chord thicknesses of the convex, concave and conventional helical gears under different Z-axis cross-sections of face width of the gears. It is found that the transverse pitch chord thickness of both ends of face width of the convex spherical helical gear is smaller than its central Z-axis cross-section of face width. Whereas, the inverse situation exists for that of the concave spherical helical gear. Moreover, the transverse pitch chord thicknesses of face width of the convex, concave and conventional helical gears under their central Z-axis cross-section are the same.

Table 2.2 Major design parameters of the hob cutter, convex, concave and conventional helical gears

Gear type	Hob cutter	Convex	Concave	Conventional helical
Normal module, m_n (mm/tooth)	4	4	4	4
Number of teeth, T_g	1	33	33	33
Normal pressure angle, α_n (deg.)	20	20	20	20
Lead angle λ_w, λ_g (deg.)	3.823 RH	75 RH	75 RH	75RH
Face width, W (mm)	-	20	20	20
Pitch radius, r_g (mm)	30	68.328	68.328	68.328
Spherical radius, R_s (mm)	-	68.328	68.328	-
Cutting radius, R_c (mm)	-	98.328	98.328	-

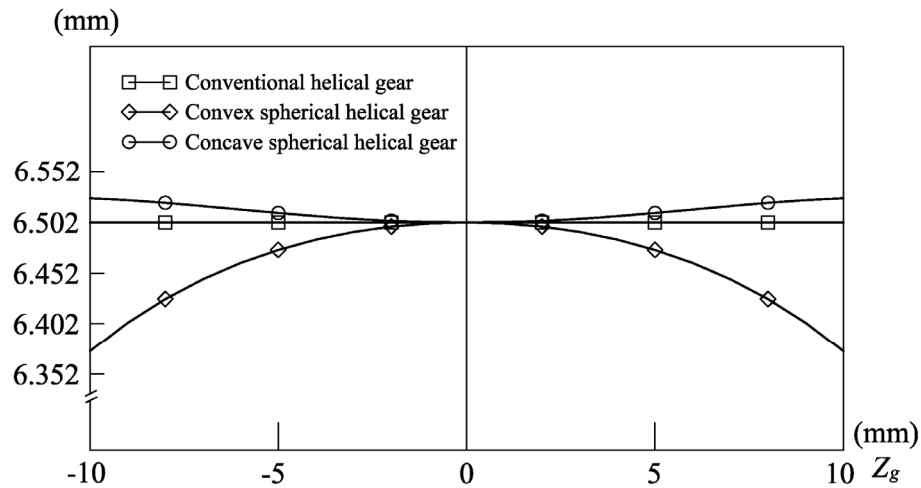


Fig. 2.9 Transverse pitch chord thicknesses of the convex, concave and conventional helical gears

2.7 Remarks

The mathematical models of spherical helical gears with convex and concave teeth have been developed on the basis of the CNC hobbing machine and the theory of gearing. The mathematical models can be derived as function of design parameters and motion parameters of a ZN-type hob cutter. Therefore, the design and motion parameters can provide us an efficient way to design and manufacture spherical helical gears. Moreover, the developed mathematical models of spherical helical gears with convex and concave teeth also help us to explore the possibility for further studies, such as sensitivity, kinematic errors, contact ratios and contact ellipses.

CHAPTER 3

Tooth Undercutting and Tooth Pointing Analyses

3.1. Introduction

Tooth undercutting is an important issue for gear design and manufacturing. When tooth undercutting occurs, the tooth thickness near the gear fillets will be decreased as shown in Fig. 3.1. It is well known that gears with tooth undercutting may result in a lower load capacity of a mating gear pair. Mathematically, the phenomenon of tooth undercutting is the appearance of singular points on an active tooth surface. Therefore, the concept for checking of the tooth undercutting of the active tooth surface is to verify the appearance of singular points on the generated tooth surface. If the active tooth surface is a regular surface, it means that there is no tooth undercutting on the active tooth surface. Moreover, the tooth undercutting usually occurs near the tooth root.

Different from the location of tooth undercutting occurrence, the tooth pointing of a gear occurs near the tooth top as shown in Fig. 3.2. If the phenomenon of tooth pointing occurs, the tooth thickness of the gear on tooth top land becomes zero. When the contact location of a mating gear pair with tooth pointing locates near the tooth top, the load capacity of the mating gear pair is weak in the contact period. Therefore, the tooth pointing is also an important issue for gear design and manufacturing.

Since the spherical helical gear is hobbled by a hob cutter, the convex and concave spherical helical gears can be considered as hobbing a helical gear with its hobbing path of continuous positive-direction or negative-direction profile-shiftings in a quadric form, beginning from both sides of the tooth face width to its middle section, respectively. Therefore, the occurrence of tooth undercuttings on both ends of face width is easier than that at the middle section for a convex spherical helical gear,

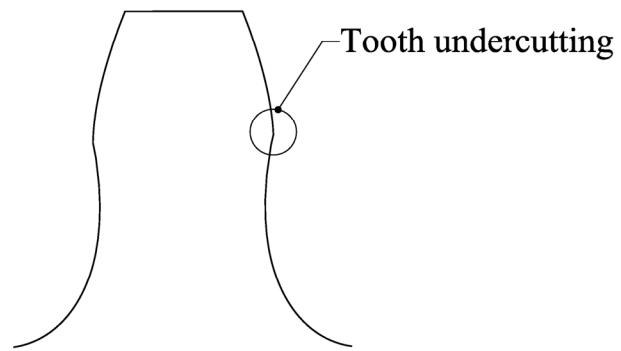


Fig. 3.1 The phenomenon of tooth undercutting

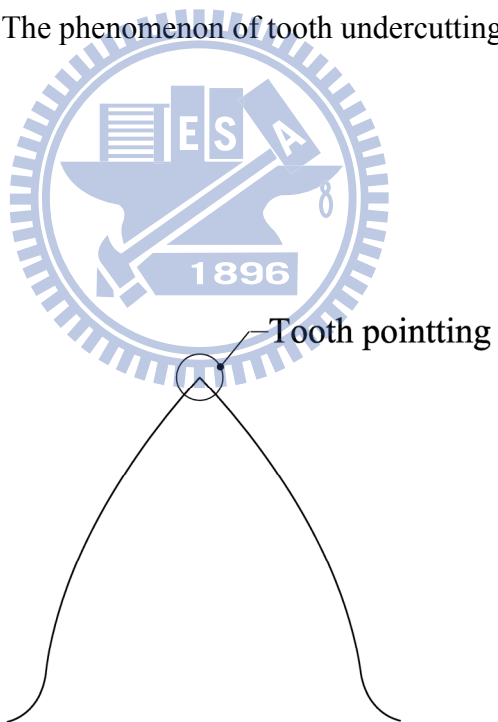


Fig. 3.2 The phenomenon of tooth pointing

whereas the inverse situation exists for the concave spherical helical gear tooth surfaces. Moreover, the occurrence of tooth pointings on both ends of face width is easier than that at the middle section for a concave spherical helical gear.

Based on the developed mathematical model and theory of gearing, the tooth undercutting of the convex spherical helical gear and the tooth pointing of the concave spherical helical gear are investigated and demonstrated by seven numerical examples in this chapter. Moreover, the limit curves and the beginning points of tooth undercutting of the convex spherical helical gear and the occurrence of tooth pointing of the concave spherical helical gear at the Z cross-section are also studied.

3.2. Tooth undercutting of convex spherical helical gear

A method proposed by Litvin [3-5], which considers the relative velocity and equation of meshing between the generating tool and generated gear, is applied in this section to determine the limit curve of tooth undercutting of the convex and concave spherical helical gears. Singularities of the generated surface occur when the relative velocity $\mathbf{V}_r^{(g)}$ of the contact point over the generated surface equals zero. The motion of the hob cutter surface that generates the envelope surface is considered as the two-parameter motion of a rigid body. In the case of two-parameter enveloping, the condition for the appearance of a singular point on the generated tooth surface can be described as follows [3-5]:

$$\frac{\partial \mathbf{R}^{(w)}}{\partial l_b} \frac{dl_b}{dt} + \frac{\partial \mathbf{R}^{(w)}}{\partial \phi_w} \frac{d\phi_w}{dt} + \mathbf{V}^{(wg,\psi)} + \mathbf{V}^{(wg,\theta_s)} = \mathbf{0}. \quad (3.1)$$

where symbol $\mathbf{R}^{(w)}$ represents the surface equation of the hob cutter, while symbols l_b and ϕ_w indicate the surface parameters of the hob cutter (see Eq. (2.3) of section 2.2). Superscripts w and g of Eq. (3.1) denote the generating tool and generated gear. Symbol $\mathbf{V}^{(wg,\psi)}$ considers that the rotational motion parameter of the hob cutter ψ

is a varied parameter and the moving motion parameter of spherical angle θ_s is fixed.

Consequently, symbol $V^{(wg,\theta_s)}$ has to be interpreted.

Differentiating Eqs. (2.29) and (2.30), two equations of meshing for the hob cutter and gear tooth surfaces, with respect to time yield that:

$$\frac{df_1(l_b, \phi_w, \psi, \theta_s)}{dt} = \frac{\partial f_1}{\partial l_b} \frac{dl_b}{dt} + \frac{\partial f_1}{\partial \phi_w} \frac{d\phi_w}{dt} + \frac{\partial f_1}{\partial \psi} \frac{d\psi}{dt} + \frac{\partial f_1}{\partial \theta_s} \frac{d\theta_s}{dt} = 0, \quad (3.2)$$

$$\text{and } \frac{df_2(l_b, \phi_w, \psi, \theta_s)}{dt} = \frac{\partial f_2}{\partial l_b} \frac{dl_b}{dt} + \frac{\partial f_2}{\partial \phi_w} \frac{d\phi_w}{dt} + \frac{\partial f_2}{\partial \psi} \frac{d\psi}{dt} + \frac{\partial f_2}{\partial \theta_s} \frac{d\theta_s}{dt} = 0. \quad (3.3)$$

Equations (3.1)-(3.3) represent a system of five equations in four unknowns: $\frac{dl_b}{dt}$, $\frac{d\phi_w}{dt}$, $\frac{d\psi}{dt}$ and $\frac{d\theta_s}{dt}$. The system of equations exists and provides a nontrivial solution if and only if the rank of the coefficient matrix for these five equations is three. Therefore, five determinants of order four for the coefficient matrix are equal to zero simultaneously. It can be proven that two of five determinants are equal to zero simultaneously, and the additional requirement is

$$\Delta_1 = \begin{vmatrix} \frac{\partial x^{(w)}}{\partial l_b} & \frac{\partial x^{(w)}}{\partial \phi_w} & V_x^{(wg,\psi)} & V_x^{(wg,\theta_s)} \\ \frac{\partial y^{(w)}}{\partial l_b} & \frac{\partial y^{(w)}}{\partial \phi_w} & V_y^{(wg,\psi)} & V_y^{(wg,\theta_s)} \\ \frac{\partial f_1}{\partial l_b} & \frac{\partial f_1}{\partial \phi_w} & \frac{\partial f_1}{\partial \psi} & \frac{\partial f_1}{\partial \theta_s} \\ \frac{\partial f_2}{\partial l_b} & \frac{\partial f_2}{\partial \phi_w} & \frac{\partial f_2}{\partial \psi} & \frac{\partial f_2}{\partial \theta_s} \end{vmatrix} = 0, \quad (3.4)$$

$$\Delta_2 = \begin{vmatrix} \frac{\partial x^{(w)}}{\partial l_b} & \frac{\partial x^{(w)}}{\partial \phi_w} & V_x^{(wg,\psi)} & V_x^{(wg,\theta_s)} \\ \frac{\partial z^{(w)}}{\partial l_b} & \frac{\partial z^{(w)}}{\partial \phi_w} & V_z^{(wg,\psi)} & V_z^{(wg,\theta_s)} \\ \frac{\partial f_1}{\partial l_b} & \frac{\partial f_1}{\partial \phi_w} & \frac{\partial f_1}{\partial \psi} & \frac{\partial f_1}{\partial \theta_s} \\ \frac{\partial f_2}{\partial l_b} & \frac{\partial f_2}{\partial \phi_w} & \frac{\partial f_2}{\partial \psi} & \frac{\partial f_2}{\partial \theta_s} \end{vmatrix} = 0, \quad (3.5)$$

$$\text{and } \Delta_3 = \begin{vmatrix} \frac{\partial y^{(w)}}{\partial l_b} & \frac{\partial y^{(w)}}{\partial \phi_w} & V_y^{(wg,\psi)} & V_y^{(wg,\theta_s)} \\ \frac{\partial z^{(w)}}{\partial l_b} & \frac{\partial z^{(w)}}{\partial \phi_w} & V_z^{(wg,\psi)} & V_z^{(wg,\theta_s)} \\ \frac{\partial f_1}{\partial l_b} & \frac{\partial f_1}{\partial \phi_w} & \frac{\partial f_1}{\partial \psi} & \frac{\partial f_1}{\partial \theta_s} \\ \frac{\partial f_2}{\partial l_b} & \frac{\partial f_2}{\partial \phi_w} & \frac{\partial f_2}{\partial \psi} & \frac{\partial f_2}{\partial \theta_s} \end{vmatrix} = 0. \quad (3.6)$$

To avoid the occurrence of tooth undercutting of the generated gear tooth surfaces, the generating hob cutter surface must be limited with the curve S_L . Considering Eqs. (3.4)-(3.6) and two equations of meshing, simultaneously, one can solve the limited curve S_L on the hob cutter surface that generates the singular points on the generated tooth surfaces. The limited curve S_L on the hob cutter surface can be determined by applying the following expressions:

$$F(l_b, \phi_w, \psi, \theta_s) = \Delta_1^2 + \Delta_2^2 + \Delta_3^2 = 0, \quad (3.7)$$

$$f_1(l_b, \phi_w, \psi, \theta_s) = 0, \quad (3.8)$$

$$\text{and } f_2(l_b, \phi_w, \psi, \theta_s) = 0. \quad (3.9)$$

Equations (3.7)-(3.9) form a system of three equations with four unknowns, l_b , ϕ_w , ψ and θ_s , one of these unknowns may be considered as an input variable, then solving three independent equations with three unknowns. Moreover, the differentiated equations of meshing, Eqs. (3.2) and (3.3), for the convex spherical helical gear can be rewritten respectively by

$$\frac{df_1}{dt} = \frac{d}{dt}(\mathbf{N}_q^{(w)} \cdot \mathbf{V}_q^{(wg,\psi)}) = \dot{\mathbf{N}}_q^{(w)} \cdot \mathbf{V}_q^{(wg,\psi)} + \mathbf{N}_q^{(w)} \cdot \dot{\mathbf{V}}_q^{(wg,\psi)} = 0, \quad (3.10)$$

$$\text{and } \frac{df_2}{dt} = \frac{d}{dt}(\mathbf{N}_q^{(w)} \cdot \mathbf{V}_q^{(wg,\theta_s)}) = \dot{\mathbf{N}}_q^{(w)} \cdot \mathbf{V}_q^{(wg,\theta_s)} + \mathbf{N}_q^{(w)} \cdot \dot{\mathbf{V}}_q^{(wg,\theta_s)} = 0, \quad (3.11)$$

where the subscript q denotes the fixed coordinate system S_q (see section 2.3).

In order to derive the differentiated equations of meshing (3.10) and (3.11), let's consider a coordinate relationship between the hob cutter and the generated gear as shown in Fig. 3.3. Axis Z_g represents the rotational axis of the generated gear. The motion of the hob cutter can be represented by two parameters, rotational angle ψ and spherical angle θ_s . Axis Z_c is the rotational axis of the hob cutter, and symbol O_c is the initial position of the hob cutter center. The point P is a common point to both rotating bodies. Moreover, $\mathbf{R}^{(w)}$ is the position vector drawn from point O_c to point P , while $\mathbf{R}^{(g)}$ represents a position vector drawn from an arbitrary point on the axis Z_g , e.g. O_g , to point P . Symbol \mathbf{d} is the relative-position vector drawn from point O_g to point O_c . The locations of original points O_c and O_g are specified by the position vectors $\mathbf{p}^{(w)}$ and $\mathbf{p}^{(g)}$, which are measured from the fixed coordinate system S_q .

According to Fig. 3.3, the velocity of point P attached to the body i ($i = w, g$) can be obtained by:

$$\mathbf{V}^{(i,j)} = \frac{\partial \mathbf{P}^{(i)}}{\partial j} \frac{dj}{dt} = \frac{\partial (\mathbf{p}^{(i)} + \mathbf{R}^{(i)})}{\partial j} \frac{dj}{dt} = \mathbf{V}^{(O_i,j)} + \boldsymbol{\omega}^{(i,j)} \times \mathbf{R}^{(i)}, \quad (3.12)$$

where symbol $\mathbf{V}^{(i,j)}$ indicates the velocity of point P attached to the body i ($i = w, g$) when parameter $j = \psi$ (or θ_s) is varied and another parameter θ_s (or ψ) is fixed. $\mathbf{V}^{(O_i,j)}$ is the velocity of point O_i ($i = w, g$) when parameter $j = \psi$ (or θ_s) is varied and parameter θ_s (or ψ) is fixed. Similarly, $\boldsymbol{\omega}^{(i,j)}$ depicts the angular velocity of body i when parameter $j = \psi$ (or θ_s) is varied and parameter θ_s (or ψ) is fixed. Therefore, the relative velocity of point P between the hob cutter ($i=w$) and generated gear ($i=g$) can be rewritten as

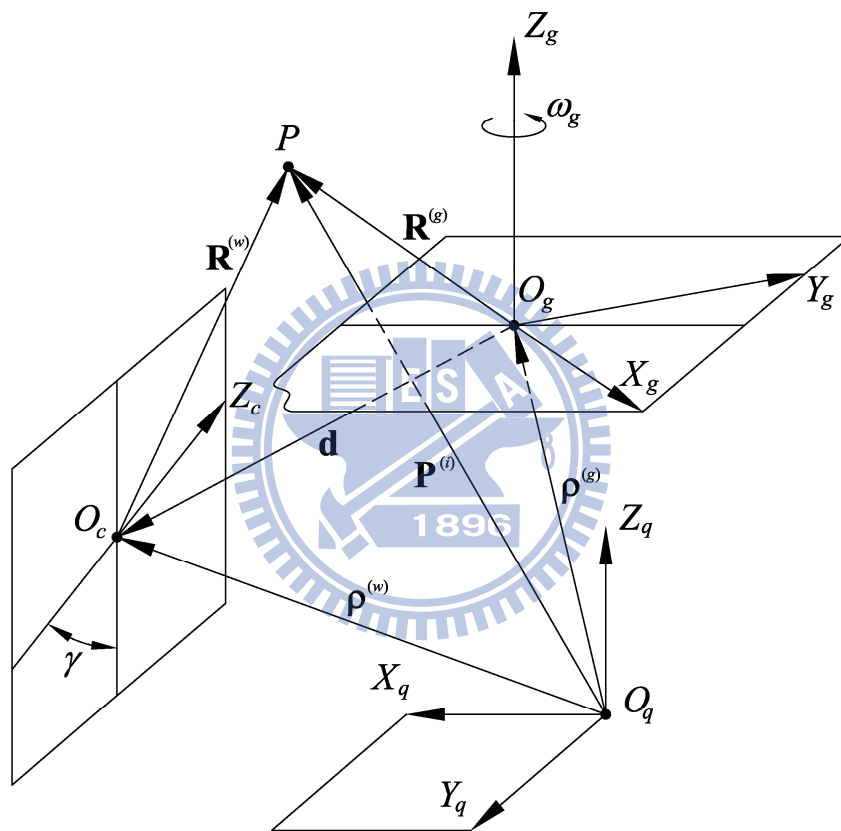


Fig. 3.3 Simulation of a generation mechanism with two-parameter motion

$$\begin{aligned}\mathbf{V}_q^{(wg,j)} &= \mathbf{V}_q^{(w,j)} - \mathbf{V}_q^{(g,j)} = (\mathbf{V}_q^{(O_w,j)} + \boldsymbol{\omega}_q^{(w,j)} \times \mathbf{R}^{(w)}) - (\mathbf{V}_q^{(O_g,j)} + \boldsymbol{\omega}_q^{(g,j)} \times \mathbf{R}^{(g)}) \\ &= (\boldsymbol{\omega}_q^{(w,j)} - \boldsymbol{\omega}_q^{(g,j)}) \times \mathbf{R}^{(w)} - \boldsymbol{\omega}_q^{(g,j)} \times \mathbf{d} + \mathbf{V}_q^{(O_w,j)} - \mathbf{V}_q^{(O_g,j)},\end{aligned}\quad (3.13)$$

where $\mathbf{R}^{(g)} = \mathbf{d} + \mathbf{R}^{(w)}$ (see Fig. 3.3).

The differentiation of Eq. (3.13) gives:

$$\begin{aligned}\frac{d}{dt} \mathbf{V}_q^{(wg,j)} &= \dot{\mathbf{V}}_q^{(wg,j)} = (\dot{\boldsymbol{\omega}}_q^{(w,j)} - \dot{\boldsymbol{\omega}}_q^{(g,j)}) \times \mathbf{R}^{(w)} + (\boldsymbol{\omega}_q^{(w,j)} - \boldsymbol{\omega}_q^{(g,j)}) \times \dot{\mathbf{R}}^{(w)} \\ &\quad - \dot{\boldsymbol{\omega}}_q^{(g,j)} \times \mathbf{d} - \boldsymbol{\omega}_q^{(g,j)} \times \dot{\mathbf{d}} + \dot{\mathbf{V}}_q^{(O_w,j)} - \dot{\mathbf{V}}_q^{(O_g,j)}.\end{aligned}\quad (3.14)$$

Differentiating the relative-position vector \mathbf{d} and $\mathbf{R}^{(w)}$ with respect to time yields:

$$\dot{\mathbf{d}} = \frac{d}{dt} \mathbf{d} = \frac{d}{dt} (\boldsymbol{\rho}^{(w)} - \boldsymbol{\rho}^{(g)}) = \mathbf{V}_q^{(O_w)} - \mathbf{V}_q^{(O_g)},\quad (3.15)$$

$$\text{and } \dot{\mathbf{R}}^{(w)} = \dot{\mathbf{P}}^{(w)} - \dot{\boldsymbol{\rho}}^{(w)} = \mathbf{V}_r^{(w)} + \mathbf{V}_{tr}^{(w)} - \mathbf{V}^{(O_w)} = \mathbf{V}_r^{(w)} + \boldsymbol{\omega}_q^{(w)} \times \mathbf{R}^{(w)}.\quad (3.16)$$

The absolute velocity of contact point P can be represented as:

$$\begin{aligned}\dot{\mathbf{P}}^{(w)} &= \mathbf{V}_{abs}^{(w)} = \mathbf{V}_r^{(w)} + \mathbf{V}_{tr}^{(w)} = \mathbf{V}_r^{(w)} + \dot{\boldsymbol{\rho}}^{(w)} + \boldsymbol{\omega}_q^{(w)} \times \mathbf{R}^{(w)} \\ &= \mathbf{V}_r^{(w)} + \mathbf{V}^{(O_w)} + \boldsymbol{\omega}_q^{(w)} \times \mathbf{R}^{(w)}.\end{aligned}\quad (3.17)$$

$$\text{where } \mathbf{V}_r^{(w)} = \frac{\partial \mathbf{R}^{(w)}}{\partial l_b} \frac{dl_b}{dt} + \frac{\partial \mathbf{R}^{(w)}}{\partial \phi_w} \frac{d\phi_w}{dt}.$$

Substituting Eqs. (3.15), (3.16) and (3.17) into Eq. (3.14), the differentiated relative velocity of point P can be represented in the coordinate system S_q as follows:

$$\begin{aligned}\dot{\mathbf{V}}_q^{(wg,j)} &= (\dot{\boldsymbol{\omega}}_q^{(w,j)} - \dot{\boldsymbol{\omega}}_q^{(g,j)}) \times \mathbf{R}^{(w)} + (\boldsymbol{\omega}_q^{(w,j)} - \boldsymbol{\omega}_q^{(g,j)}) \times (\mathbf{V}_r^{(w)} + \boldsymbol{\omega}_q^{(w)} \times \mathbf{R}^{(w)}) \\ &\quad - \dot{\boldsymbol{\omega}}_q^{(g,j)} \times \mathbf{d} - \boldsymbol{\omega}_q^{(g,j)} \times (\mathbf{V}_q^{(O_w)} - \mathbf{V}_q^{(O_g)}) + \dot{\mathbf{V}}_q^{(O_w,j)} - \dot{\mathbf{V}}_q^{(O_g,j)}.\end{aligned}\quad (3.18)$$

Similarly, the differentiation of normal vector at point P can be obtained as follows:

$$\dot{\mathbf{N}}_q^{(w)} = \frac{d}{dt} \mathbf{N}_q^{(w)} = \dot{\mathbf{N}}_r^{(w)} + \dot{\mathbf{N}}_{tr}^{(w)} = \dot{\mathbf{N}}_r^{(w)} + \boldsymbol{\omega}_q^{(w)} \times \mathbf{N}_q^{(w)},\quad (3.19)$$

$$\text{where } \dot{\mathbf{N}}_r^{(w)} = \frac{\partial \mathbf{N}_q^{(w)}}{\partial l_b} \frac{dl_b}{dt} + \frac{\partial \mathbf{N}_q^{(w)}}{\partial \phi_w} \frac{d\phi_w}{dt}.$$

Substituting Eqs. (3.18) and (3.19) into Eqs. (3.10) and (3.11), the differentiated equations of meshing of the spherical helical gear can be rewritten as follows:

$$\begin{aligned} \dot{f}_1 = & \dot{\mathbf{N}}_r^{(w)} \cdot \mathbf{V}_q^{(wg,\psi)} + (\boldsymbol{\omega}_q^{(w)} \times \mathbf{N}_q^{(w)}) \cdot \mathbf{V}_q^{(wg,\psi)} + \mathbf{N}_q^{(w)} \cdot [(\dot{\boldsymbol{\omega}}_q^{(w,\psi)} - \dot{\boldsymbol{\omega}}_q^{(g,\psi)}) \times \mathbf{d}^{(w)}] \\ & + \mathbf{N}_q^{(w)} \cdot [(\boldsymbol{\omega}_q^{(w,\psi)} - \boldsymbol{\omega}_q^{(g,\psi)}) \times (\mathbf{V}_r^{(w)} + \boldsymbol{\omega}_q^{(w)} \times \mathbf{d}^{(w)})] - \mathbf{N}_q^{(w)} \cdot (\dot{\boldsymbol{\omega}}_q^{(g,\psi)} \times \mathbf{d}) \\ & - \mathbf{N}_q^{(w)} \cdot [\boldsymbol{\omega}_q^{(g,\psi)} \times (\mathbf{V}_q^{(O_w)} - \mathbf{V}_q^{(O_g)})] + \mathbf{N}_q^{(w)} \cdot (\dot{\mathbf{V}}_q^{(O_w,\psi)} - \dot{\mathbf{V}}_q^{(O_g,\psi)}) = 0, \end{aligned} \quad (3.20)$$

and

$$\begin{aligned} \dot{f}_2 = & \dot{\mathbf{N}}_r^{(w)} \cdot \mathbf{V}_q^{(wg,\theta_s)} + (\boldsymbol{\omega}_q^{(w)} \times \mathbf{N}_q^{(w)}) \cdot \mathbf{V}_q^{(wg,\theta_s)} + \mathbf{N}_q^{(w)} \cdot [(\dot{\boldsymbol{\omega}}_q^{(w,\theta_s)} - \dot{\boldsymbol{\omega}}_q^{(g,\theta_s)}) \times \mathbf{d}^{(w)}] \\ & + \mathbf{N}_q^{(w)} \cdot [(\boldsymbol{\omega}_q^{(w,\theta_s)} - \boldsymbol{\omega}_q^{(g,\theta_s)}) \times (\mathbf{V}_r^{(w)} + \boldsymbol{\omega}_q^{(w)} \times \mathbf{d}^{(w)})] - \mathbf{N}_q^{(w)} \cdot (\dot{\boldsymbol{\omega}}_q^{(g,\theta_s)} \times \mathbf{d}) \\ & - \mathbf{N}_q^{(w)} \cdot [\boldsymbol{\omega}_q^{(g,\theta_s)} \times (\mathbf{V}_q^{(O_w)} - \mathbf{V}_q^{(O_g)})] + \mathbf{N}_q^{(w)} \cdot (\dot{\mathbf{V}}_q^{(O_w,\theta_s)} - \dot{\mathbf{V}}_q^{(O_g,\theta_s)}) = 0. \end{aligned} \quad (3.21)$$

It is noted that the schematic mechanism of a CNC hobbing machine for the spherical helical gear generation can be referred to Fig. 2.5. Coordinate system $S_w(X_w, Y_w, Z_w)$ is attached to the hob cutter while coordinate system $S_g(X_g, Y_g, Z_g)$ is attached to the gear blank. Coordinate system $S_h(X_h, Y_h, Z_h)$ is the reference coordinate system and coordinate system $S_q(X_q, Y_q, Z_q)$ is the fixed coordinate system attached to the machine housing. Symbols ψ and ϕ_g are rotational angles of the hob cutter and gear blank, respectively. θ_s indicates the spherical angle. By compared Fig. 2.5 with Fig. 3.3, the schematic gear generation mechanism, the following position vectors can be found as:

$$\boldsymbol{\rho}^{(w)} = \mathbf{d} = [l_c - l_x \quad 0 \quad l_z]^T, \quad (3.22)$$

$$\boldsymbol{\rho}^{(w)} = \mathbf{0}, \quad (3.23)$$

$$\text{and } \mathbf{R}^{(w)} = \mathbf{R}^{(g)} - \mathbf{d} = [x_q - (l_c - l_x) \quad y_q \quad z_q - l_z]^T, \quad (3.24)$$

where the position vector $\mathbf{R}^{(g)} = [x_q \quad y_q \quad z_q]^T$, while symbols $l_x = R_c(1 - \cos\theta_s)$,

$$l_z = R_c \sin \theta_s \quad \text{and} \quad l_c = r_w + r_g.$$

The velocity of the points O_w and O_g can be obtained as

$$\mathbf{V}_q^{(O_w)} = \dot{\mathbf{p}}^{(w)} = \dot{\mathbf{d}} = [-R_c \sin \theta_s \quad 0 \quad R_c \cos \theta_s]^T \frac{d\theta_s}{dt}, \quad (3.25)$$

$$\text{and} \quad \mathbf{V}_q^{(O_g)} = \dot{\mathbf{p}}^{(g)} = \mathbf{0}, \quad (3.26)$$

respectively.

Differentiate Eq. (3.25) with respect to time by considering that $\frac{d\theta_s}{dt}$ and $\frac{d\psi}{dt}$ are constants. It yields:

$$\dot{\mathbf{V}}_q^{(O_w)} = \frac{d\mathbf{V}_q^{(O_w)}}{dt} = \frac{\partial \mathbf{V}_q^{(O_w)}}{\partial \psi} \frac{\partial \psi}{\partial t} + \frac{\partial \mathbf{V}_q^{(O_w)}}{\partial \theta_s} \frac{\partial \theta_s}{\partial t} = \dot{\mathbf{V}}_q^{(O_w, \psi)} + \dot{\mathbf{V}}_q^{(O_w, \theta_s)}, \quad (3.27)$$

where $\dot{\mathbf{V}}_q^{(O_w, \psi)} = \mathbf{0}$ and $\dot{\mathbf{V}}_q^{(O_w, \theta_s)} = [-R_c \cos \theta_s \quad 0 \quad -R_c \sin \theta_s]^T \left(\frac{d\theta_s}{dt}\right)^2$.

Similarly, the differentiated form of Eq. (3.26) with respect to time can be represented by

$$\dot{\mathbf{V}}_q^{(O_g)} = \frac{d\mathbf{V}_q^{(O_g)}}{dt} = \frac{\partial \mathbf{V}_q^{(O_g)}}{\partial \psi} \frac{\partial \psi}{\partial t} + \frac{\partial \mathbf{V}_q^{(O_g)}}{\partial \theta_s} \frac{\partial \theta_s}{\partial t} = \dot{\mathbf{V}}_q^{(O_g, \psi)} + \dot{\mathbf{V}}_q^{(O_g, \theta_s)}, \quad (3.28)$$

where $\dot{\mathbf{V}}_q^{(O_g, \psi)} = \mathbf{0}$ and $\dot{\mathbf{V}}_q^{(O_g, \theta_s)} = \mathbf{0}$.

According to the hobbing mechanism of the spherical helical gear, mentioned in section 2.4, the angular velocity of the hob cutter $\boldsymbol{\omega}^{(w)}$ and the generated gear $\boldsymbol{\omega}^{(g)}$ can be represented as follows:

$$\boldsymbol{\omega}_q^{(w)} = \mathbf{L}_{qc} \boldsymbol{\omega}_c^{(w)} = [0 \quad -\sin \gamma \quad \cos \gamma]^T \frac{d\psi}{dt}, \quad (3.29)$$

$$\text{and} \quad \boldsymbol{\omega}_q^{(g)} = [0 \quad 0 \quad m_{wg}]^T \frac{d\psi}{dt} + [0 \quad 0 \quad \frac{R_c \cos \theta_s}{p_g}]^T \frac{d\theta_s}{dt}. \quad (3.30)$$

Similarly, by considering $\frac{d\theta}{dt}$ and $\frac{d\psi}{dt}$ as constants, the differentiation of angular velocity of the hob cutter $\dot{\boldsymbol{\omega}}_q^{(w)}$ and generated gear $\dot{\boldsymbol{\omega}}_q^{(g)}$ can be obtained by:

$$\dot{\boldsymbol{\omega}}_q^{(w)} = \frac{d\boldsymbol{\omega}_q^{(w)}}{dt} = \frac{\partial \boldsymbol{\omega}_q^{(w)}}{\partial \psi} \frac{\partial \psi}{\partial t} + \frac{\partial \boldsymbol{\omega}_q^{(w)}}{\partial \theta_s} \frac{\partial \theta_s}{\partial t} = \dot{\boldsymbol{\omega}}_q^{(w,\psi)} + \dot{\boldsymbol{\omega}}_q^{(w,\theta_s)}, \quad (3.31)$$

$$\text{and } \dot{\boldsymbol{\omega}}_q^{(g)} = \frac{d\boldsymbol{\omega}_q^{(g)}}{dt} = \frac{\partial \boldsymbol{\omega}_q^{(g)}}{\partial \psi} \frac{\partial \psi}{\partial t} + \frac{\partial \boldsymbol{\omega}_q^{(g)}}{\partial \theta_s} \frac{\partial \theta_s}{\partial t} = \dot{\boldsymbol{\omega}}_q^{(g,\psi)} + \dot{\boldsymbol{\omega}}_q^{(g,\theta_s)}, \quad (3.32)$$

where $\dot{\boldsymbol{\omega}}_q^{(w,\psi)} = \mathbf{0}$, $\dot{\boldsymbol{\omega}}_q^{(w,\theta_s)} = \mathbf{0}$, $\dot{\boldsymbol{\omega}}_q^{(g,\psi)} = \mathbf{0}$ and $\dot{\boldsymbol{\omega}}_q^{(g,\theta_s)} = [0 \quad 0 \quad \frac{-R_c \sin \theta_s}{p_g}]^T (\frac{d\theta_s}{dt})^2$.

According to the hobbing mechanism of the spherical helical gear, the relative velocity $\mathbf{V}_q^{(wg,\psi)}$ and $\mathbf{V}_q^{(wg,\theta_s)}$ can be obtained by

$$\begin{aligned} \mathbf{V}_q^{(wg,\psi)} &= (\boldsymbol{\omega}_q^{(w,\psi)} - \boldsymbol{\omega}_q^{(g,\psi)}) \times \mathbf{R}^{(w)} - \boldsymbol{\omega}_q^{(g,\psi)} \times \mathbf{d} + \mathbf{V}_q^{(O_w,\psi)} - \mathbf{V}_q^{(O_g,\psi)} \\ &= \begin{bmatrix} (l_z - z_q) \sin \gamma - y_q (\cos \gamma - m_{wg}) \\ (x_q - l_c + l_x) \cos \gamma - x_q m_{wg} \\ (x_q - l_c + l_x) \sin \gamma \end{bmatrix} \frac{d\psi}{dt}, \end{aligned} \quad (3.33)$$

and

$$\begin{aligned} \mathbf{V}_q^{(wg,\theta_s)} &= (\boldsymbol{\omega}_q^{(w,\theta_s)} - \boldsymbol{\omega}_q^{(g,\theta_s)}) \times \mathbf{R}^{(w)} - \boldsymbol{\omega}_q^{(g,\theta_s)} \times \mathbf{d} + \mathbf{V}_q^{(O_w,\theta_s)} - \mathbf{V}_q^{(O_g,\theta_s)} \\ &= \begin{bmatrix} R_c (\sin \theta_s + y_q \cos \theta_s / p_g) \\ -x_q R_c \cos \theta_s / p_g \\ -R_c \cos \theta_s \end{bmatrix} \frac{d\theta_s}{dt}. \end{aligned} \quad (3.34)$$

3.3. Tooth pointing of concave spherical helical gear

Tooth pointing of a gear means that the tooth thickness of the tooth top-land becomes zero. In other words, the tooth pointing can also be considered as the left-side and right-side tooth profiles of a gear intersect as a point at its tooth top-land in a cross-section of face width. Since the concave spherical helical gear can be

considered as hobbing a helical gear with its hobbing path of continuous negative-direction profile-shiftings in a quadric form, beginning from both sides of the tooth face width to its middle section. Therefore, the occurrence of tooth pointing on both ends of face width is easier than that at the middle section for a concave spherical helical gear. Figure 3.4 illustrates the tooth pointing occurs on the tooth top-land of a concave spherical helical gear. Symbol d_t of Fig. 3.4 denotes the tooth thickness of the tooth top-land at any Z_g cross-section of face width of the concave spherical helical gear. According to the concept of tooth pointing, the condition equations of tooth pointing at the Z_g cross-section of face width of the concave spherical helical gear can be considered as follows:

$$\mathbf{R}_{g,left} = \mathbf{R}_{g,right} \quad (3.35)$$

$$\sqrt{X_{g,left}^2 + Y_{g,left}^2} = \sqrt{X_{g,right}^2 + Y_{g,right}^2} = r_{tl} \quad (3.36)$$

$$f_{1,left}(l_{b,left}, \phi_{w,left}, \psi_{left}, \theta_{s,left}) = 0, \quad (3.37)$$

$$f_{2,left}(l_{b,left}, \phi_{w,left}, \psi_{left}, \theta_{s,left}) = 0, \quad (3.38)$$

$$f_{1,right}(l_{b,right}, \phi_{w,right}, \psi_{right}, \theta_{s,right}) = 0, \quad (3.39)$$

$$\text{and } f_{2,right}(l_{b,right}, \phi_{w,right}, \psi_{right}, \theta_{s,right}) = 0, \quad (3.40)$$

where, subscripts “left” and “right” of Eqs. (3.35)-(3.40) denote the left-side and right-side tooth profiles of the concave spherical helical gear, respectively, while symbol r_{tl} indicates the radius of the tooth top circle. Symbols X_g and Y_g denote the X and Y components of position vector \mathbf{R}_g , respectively. Equation (3.35) explains that the left-side and right-side tooth flank profiles of the concave spherical helical

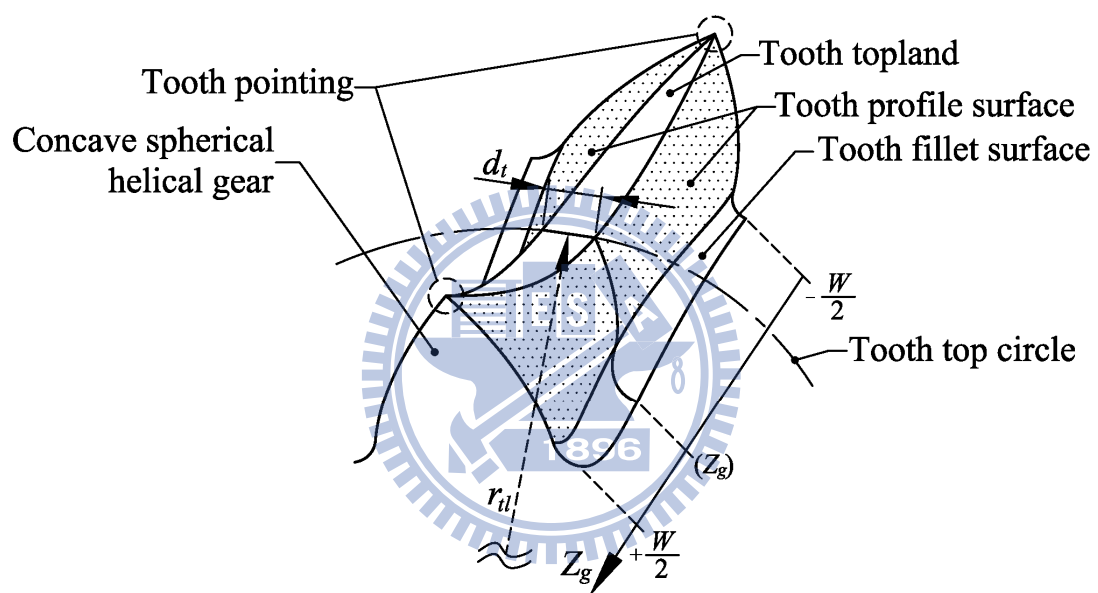


Fig. 3.4 Tooth pointing of concave spherical helical gear

gear intersected as a point at the Z_g cross-section of the gear fact width. Equation (3.36) denotes the crossing point formed by the left-side and right-side tooth profiles of the concave spherical helical gear locates on the tooth top-land. Moreover, Eqs.(3.37) and (3.38) are the equations of meshing of left-side tooth profile of the concave spherical helical gear, while Eqs.(3.39) and (3.40) are the equations of meshing of right-side tooth profile of the gear. Since Eq. (3.35) includes three independent nonlinear equations, Eqs. (3.35)-(3.40) yields a system of eight independent equations with eight variables $l_{b,left}$, $\phi_{w,left}$, ψ_{left} , $\theta_{s,left}$, $l_{b,right}$, $\phi_{w,right}$, ψ_{right} and $\theta_{s,right}$.

3.4. Numerical examples

According to the developed tooth undercutting condition equations of the convex spherical helical gear (Eqs. (3.7)-(3.9)), the tooth undercutting analysis of the proposed convex spherical helical gear is investigated. Moreover, the tooth pointing analysis of the concave spherical helical gear is also discussed based on the development tooth pointing condition equations (Eqs. (3.35)-(3.40)) of the gear. All analysis results of the tooth undercutting and tooth pointing are illustrated by the following numerical examples. Furthermore, some major design parameters of the proposed convex and concave spherical helical gears for the numerical examples are given in Table 3.1.

Example 3.1: Tooth profiles of the convex spherical helical gear with tooth undercutting under different Z_g cross-sections.

This example investigates the tooth profiles of the convex spherical helical gear with tooth undercutting under different Z_g cross-sections. Where the Z_g cross-section denotes the cross-section along the rotation axis (Z_g -axis) of the convex spherical

Table 3.1 Major design parameters of the hob cutter, convex spherical helical gear

	Hob cutter	Convex tooth	Concave tooth
Normal module, m_n (mm/tooth)	4	4	4
Number of teeth, T	1	22	22
Normal pressure angle, α_n (deg.)	20	20	20
Lead angle (deg.)	3.823 RH	75 RH	75 RH
Face width, W (mm)	-	20	20
Pitch radius, r_j (mm)	30	45.552	45.552
Spherical radius, R_s (mm)	-	45.552	45.552
Cutting radius, R_c (mm)	-	75.552	15.552

helical gear. The analysis results are obtained based on the convex spherical helical gear data given in Table 3.1.

Figure 3.5 illustrates the tooth profiles of the convex spherical helical gear with tooth undercutting under different Z_g cross-sections of the gear. It can be found that the convex spherical helical gear have tooth undercuts on the left-side tooth profiles of $Z_g=+10\text{mm}$ and $Z_g=+5\text{mm}$ of the face width and on the right-side tooth profiles of $Z_g=-10\text{mm}$ and $Z_g=-5\text{mm}$ of the face width. Therefore, the tooth undercutting curves on the left- and right-side tooth surfaces of the convex spherical gear are not symmetric. Table 3.2 lists the coordinate positions of the left- and right-side tooth profiles of the convex spherical helical gear at $Z_g=0\text{mm}$ cross-section of face width of the gear, while each coordinate position of the tooth profiles of the gear can be generated by the corresponding hob cutter's parameter l_b under its working interval $l_{b,min} \leq l_b \leq l_{b,max}$. According to Table 3.2, the left- and right-side tooth profiles of the convex spherical helical gear are geometrical symmetry at central cross-section ($Z_g=0\text{mm}$) of face width of the gear.

Example 3.2: Limit curves of tooth undercutting of convex spherical helical gears under different number of gear teeth

Table 3.2 The coordinates of left- and right-side tooth profiles of the convex spherical helical gear at $Z_g=0$ mm cross-section

(unit: mm)

l_b	Left-side			Right-side		
	X_g	Y_g	Z_g	X_g	Y_g	Z_g
5.758	49.530	-1.470	0.0	49.530	+ 1.470	0.0
7.294	47.514	-2.482		47.514	+ 2.482	
8.831	45.787	-3.141		45.787	+ 3.141	
10.368	44.410	-3.512		44.410	+ 3.512	
11.905	43.442	-3.669		43.442	+ 3.669	
13.441	42.938	-3.699		42.938	+ 3.699	

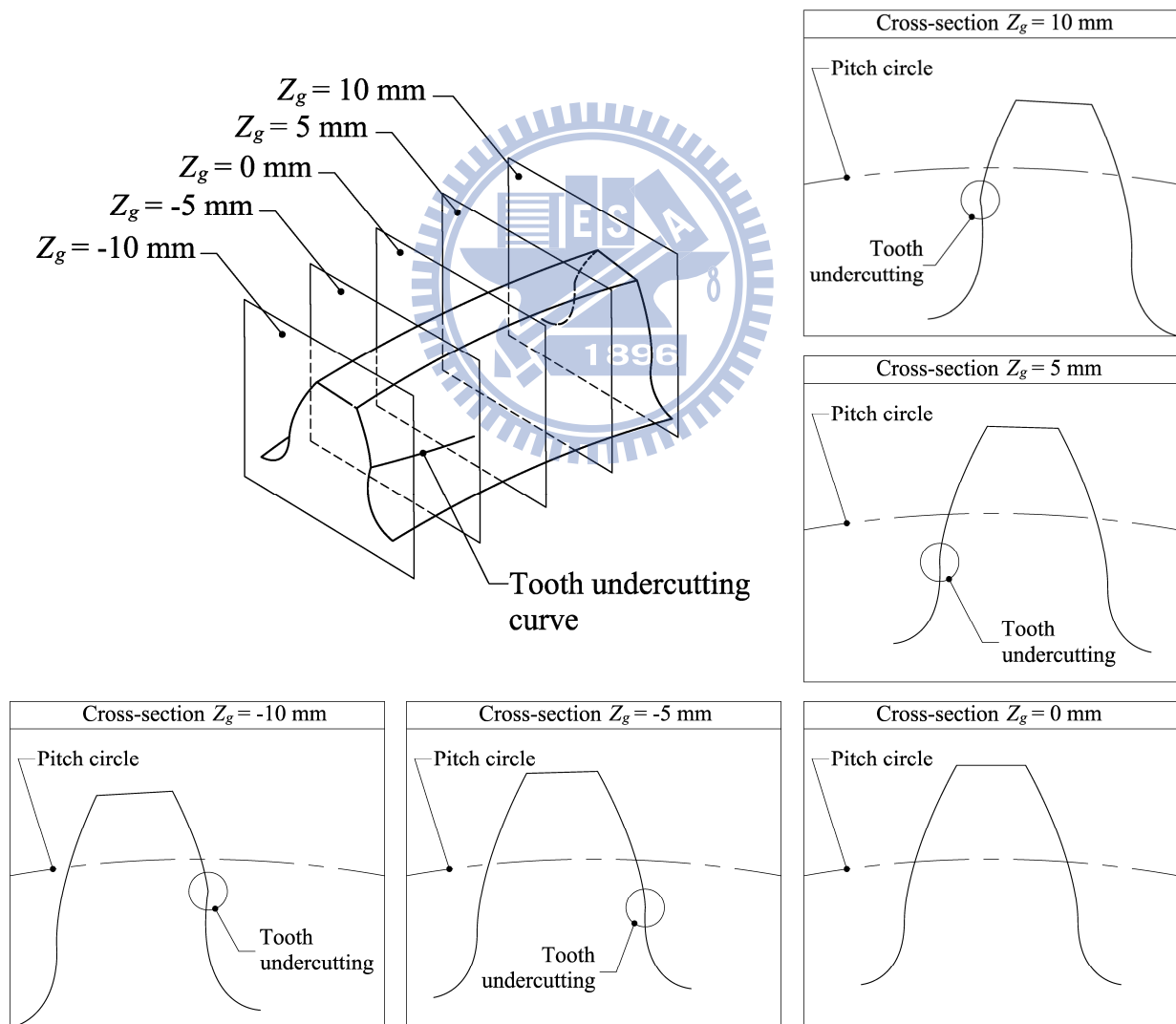


Fig. 3.5 Tooth profile of the convex spherical helical gear with tooth undercutting under different Z_g cross-sections

This example shows the positions of singular points appeared along the Z_g -axis of the convex spherical helical gears under different number of gear teeth T_g ($T_g=22, 24, 26, 28$ and 30 teeth). A set of singular points appeared on the generated gear tooth flank which corresponds to a set of points located on hob cutter working surface is called the limit curve of tooth undercutting. The analysis results are obtained based on the convex spherical helical gear data given in Table 3.1.

Figure 3.6 shows the locations of limit curves of tooth undercutting appeared on the left-side tooth flank along the Z_g -axis of the convex spherical helical gear in terms of hob cutter's surface parameter l_b under different number of gear teeth T_g . Symbols $l_{b,max}$ and $l_{b,min}$ denote the maximum and minimum working intervals of the hob cutter's surface parameter l_b , respectively (see Fig. 2.2(b)). If the limit curve of tooth undercutting locates inside the working interval of hob cutter's surface parameter l_b , it means that the tooth undercutting occurs on the tooth flank of the

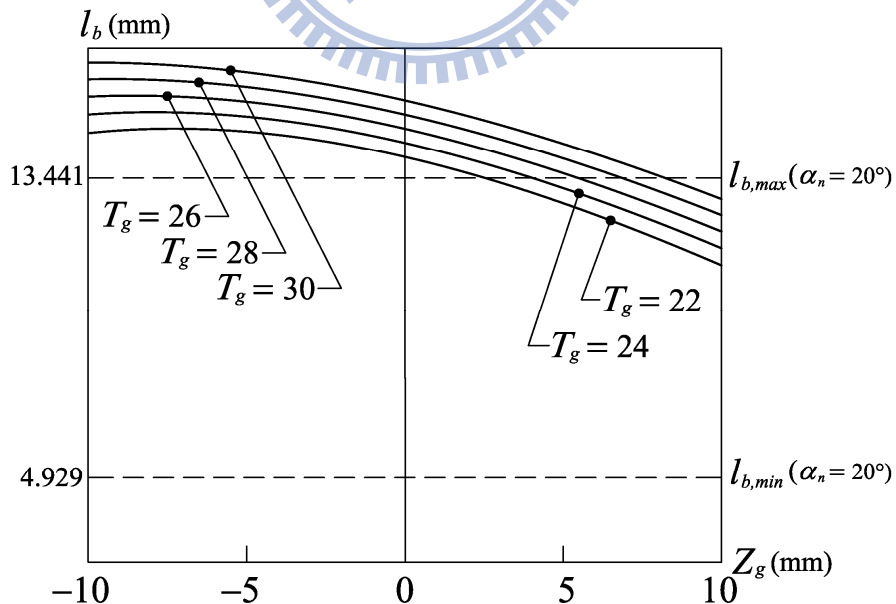


Fig. 3.6 Locations of limit curves of the convex spherical helical gear under different number of teeth T_g

convex spherical helical gear. When the number of teeth of the convex spherical helical gear is 22 teeth, there is a more severe tooth undercutting at its end section ($Z_g=+10\text{mm}$) of tooth face width. Moreover, it can be obtained that the locations of the limit curves of tooth undercutting of the convex spherical helical gear are moving away from the working interval ($l_{b,min} \leq l_b \leq l_{b,max}$) of hob cutter's surface parameter l_b by increasing the number of gear teeth. It means that the tooth undercutting phenomenon of the convex spherical helical gear can also be improved by increasing the number of gear teeth.

Example 3.3: Limit curves of tooth undercutting of convex spherical helical gears under different gear's lead angles

This example discusses the positions of singular points appeared along the Z_g -axis of the convex spherical helical gears under different gear's lead angle λ_g ($\lambda_g=75^\circ, 80^\circ, 85^\circ$ and 90°). The analysis results are obtained based on the convex spherical helical gear data given in Table 3.1.

Figure 3.7 illustrates the locations of limit curves of tooth undercutting appeared on the left-side tooth flank along the Z_g -axis of the convex spherical helical gear in terms of hob cutter's surface parameter l_b under different gear's lead angle λ_g . It can be obtained that the lead angle of the convex spherical helical gear affects the trend of limit curve of gear's tooth undercutting. When the lead angle of the convex spherical helical gear is equal to 90° (helix angle becomes 0°), the limit curve of tooth undercutting of the gear becomes symmetry in the central section of face width of the gear ($Z_g=0\text{mm}$).

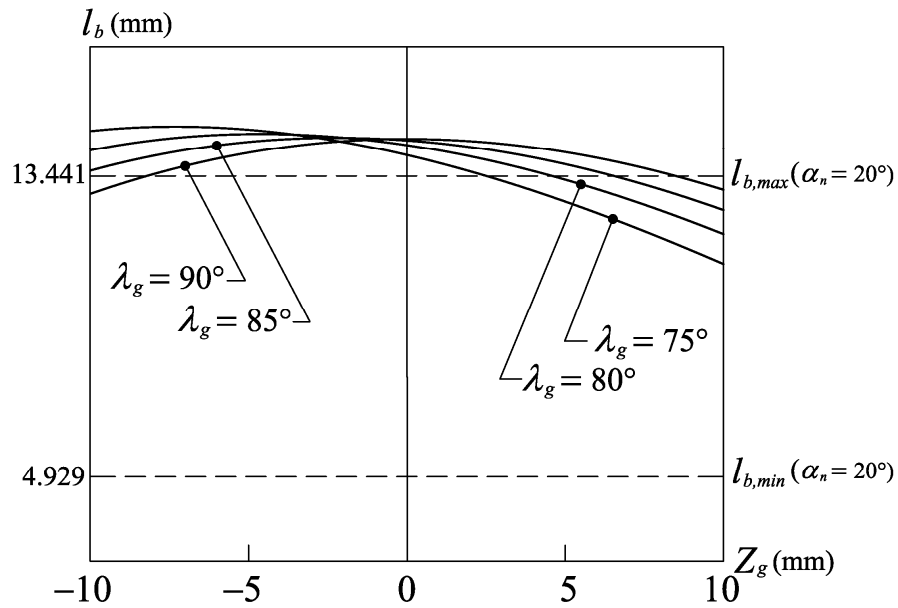


Fig. 3.7 Locations of limit curves of the convex spherical helical gear under different gear's lead angle λ_g

Example 3.4: Limit curves of tooth undercutting of convex spherical helical gears under different hob cutter's pitch radii

This example discusses the positions of singular points appeared along the Z_g -axis of the convex spherical helical gears under different hob cutter's pitch radius r_w ($r_w=30\text{mm}$, 45mm and 60mm). The analysis results are obtained based on the convex spherical helical gear data given in Table 3.1.

Figure 3.8 illustrates the locations of limit curves of tooth undercutting appeared on the left-side tooth flank along the Z_g -axis of the convex spherical helical gear in terms of hob cutter's surface parameter l_b under different hob cutter's pitch radius r_w . It is formed that decreasing the hob cutter's pitch radius can improve the tooth undercutting of the convex spherical helical gear at the end of gear's face width. However, the size of hob cutter's pitch radius depends on the strength and the shaft size of the hob cutter.

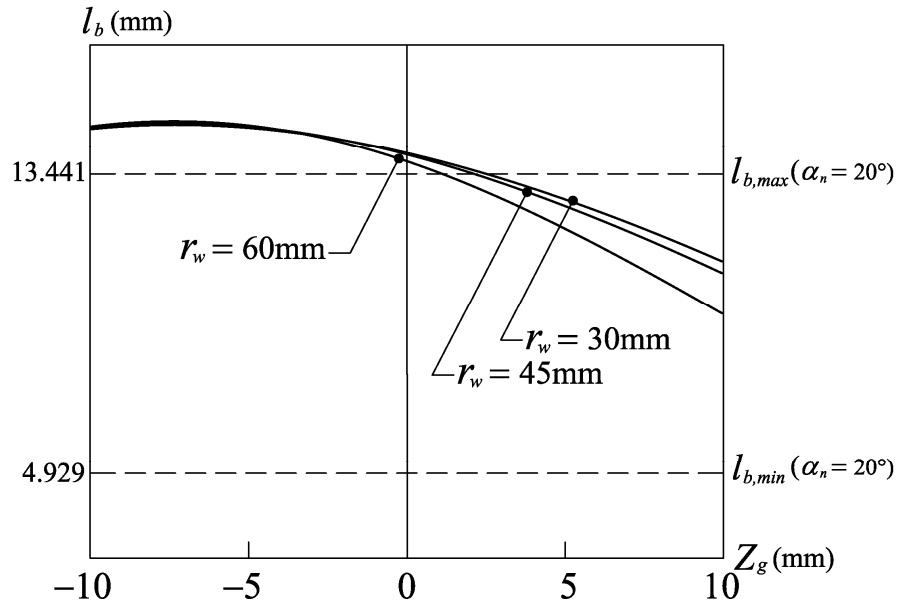


Fig. 3.8 Locations of limit curves of the convex spherical helical gear under different hob cutter's pitch radius r_w

Example 3.5: Limit curves of tooth undercutting of convex spherical helical gears under different gear's normal pressure angles

This example discusses the positions of singular points appeared along the Z_g -axis of the convex spherical helical gears under different gear's normal pressure angle α_n ($\alpha_n=14.5^\circ$, 20° and 25°). The analysis results are obtained based on the convex spherical helical gear data given in Table 3.1.

Figure 3.9 illustrates the locations of limit curves of tooth undercutting appeared on the left-side tooth flank along the Z_g -axis of the convex spherical helical gear in terms of hob cutter's surface parameter l_b under different gear's normal pressure angle α_n . The red, black and blue curves of Fig. 3.9 indicate the limit curves of tooth undercutting of the convex spherical helical gear under the gear's normal pressure angles 14.5° , 20° and 25° , respectively. Since different normal pressure angles of the convex spherical helical gear result in different working intervals of hob cutter's surface parameter l_b , the red, black and blue limit curves of Fig. 3.9 correspond to

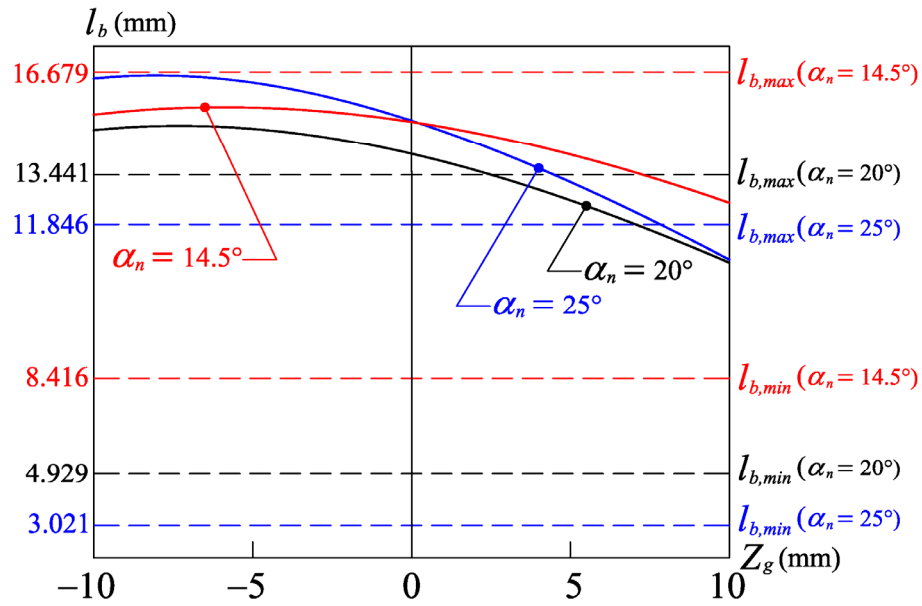


Fig. 3.9 Locations of limit curves of the convex spherical helical gear under different normal pressure angle α_n

the red, black and blue hidden lines of the working intervals ($l_{b,min} \leq l_b \leq l_{b,max}$), respectively. According to Fig. 3.9, increasing the normal pressure angle of the convex spherical helical gear can improve the gear's tooth undercutting.

Example 3.6: Investigation on tooth pointing of concave spherical helical gears by checking along Z_g cross-sections under different hob cutter's pitch radii and number of gear teeth

Based on the developed condition equations (Eqs. (3.35)-(3.40)) of tooth pointing of the proposed concave spherical helical gear, this example discusses the Z_g cross-section of tooth pointing beginning of the concave spherical helical gear under different hob cutter's pitch radius r_w ($r_w=30\text{mm}$, 45mm and 60mm) and different number of teeth T_g ($T_g =15\sim35$ teeth). Where the Z_g cross-section denotes the cross-section along the rotation axis (Z_g -axis) of the concave spherical helical gear. The analysis results are obtained based on the concave spherical helical gear data

given in Table 3.1.

Figure 3.10 illustrates the beginning tooth pointing at $\pm Z_g$ cross-sections of the concave spherical helical gear under different hob cutter's pitch radii and different number of teeth. The purple hidden curves of Fig. 3.10 indicate the $\pm Z_g$ cross-sections of tooth pointing beginning of the concave spherical helical gear generated by the hob cutter's pitch radius $r_w=30\text{mm}$ under different number of teeth, while the blue and red ones denote those of the hob cutter's pitch radii $r_w=45\text{mm}$ and 60mm , respectively. Since the spherical radius R_s of the concave spherical helical gear is limited by the hob cutter's pitch radius r_w (see Fig. 2.6) and the spherical radius R_s depends on the number of the gear teeth ($R_s=r_g$), the initial number of teeth of the gear for the tooth pointing beginning at Z_g cross-section is limited by the hob cutter's pitch radius. For the gear design parameters given in Table 3.1 and hob cutter's pitch radii $r_w=30\text{mm}$, 45mm and 60mm , the initial number of teeth of the concave spherical helical gear are

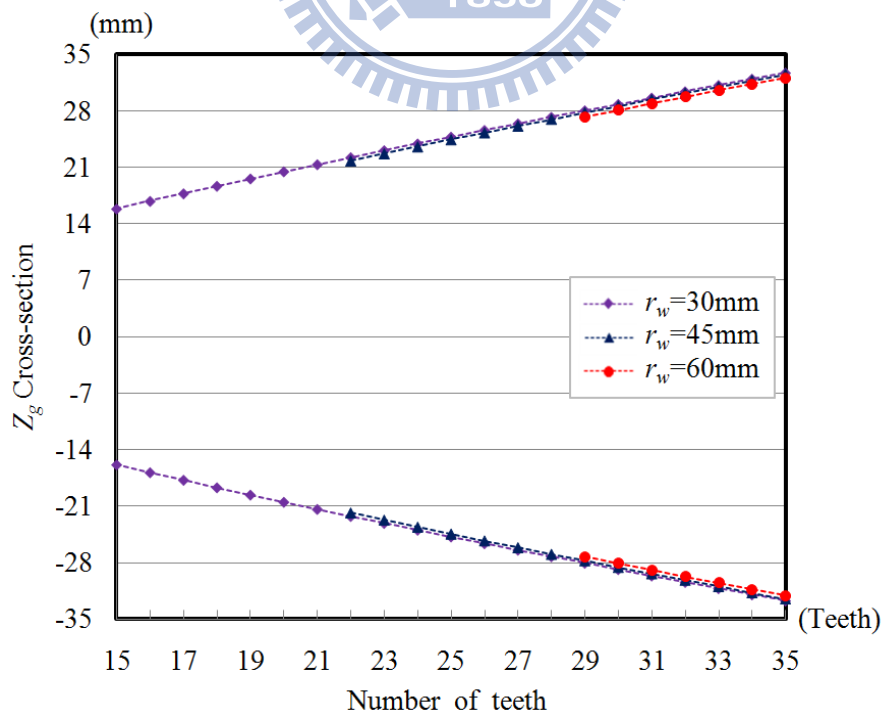


Fig. 3.10 The Z_g cross-sections of tooth pointing beginning of the concave spherical helical gear

15, 22 and 29 teeth, respectively. According to Fig. 3.10, the size of the hob cutter's pitch radius only has a small effect on the tooth pointing beginning at Z_g cross-section of the concave spherical helical gear. Moreover, it can also be found that the $\pm Z_g$ cross-sections of tooth pointing beginning of the concave spherical helical gear depend on the number of the gear teeth. Therefore, the suitable face width of the concave spherical helical gear with tooth non-pointing can be designed by $W < | +Z_g | + | -Z_g |$.

Example 3.7: Tooth pointing of concave spherical helical gears under different normal pressure angles and different gear's lead angles by checking along Z_g cross-sections

This example investigates the Z_g cross-section of tooth pointing beginning of the concave spherical helical gear under different normal pressure angle α_n ($\alpha_n=14.5^\circ$, 20° and 25°) and different gear's lead angle λ_g ($\lambda_g=75^\circ$, 80° , 85° and 90°). Again, the Z_g cross-section denotes the cross-section along the rotation axis (Z_g -axis) of the concave spherical helical gear. The analysis results are obtained based on the concave spherical helical gear data given in Table 3.1.

Tables 3.3 and 3.4 list the $\pm Z_g$ cross-sections of tooth pointing beginning of the concave spherical helical gear under different normal pressure angles and gear's lead angles, respectively. It is found that the concave spherical helical gear with a larger normal pressure angle and gear lead angle allows a smaller value of face width of the gear. However, the effects of increasing the normal pressure and the gear lead angle on the value of face width of the concave spherical helical gear are small.

3.5. Remarks

Since the tooth surfaces of the proposed convex spherical helical gear are the

Table 3.3 The Z_g cross-section of tooth pointing beginning of the concave spherical helical gear under different normal pressure angle α_n

Basic gear parameters: $\lambda_g=75^\circ$, $T_g=22$ teeth, $r_w=30\text{mm}$			
Normal pressure angle α_n (deg.)	14.5	20	25
Z_g cross-sections (mm)	± 22.29	± 22.25	± 21.48
Suitable face width W (mm)	< 44.58	< 44.50	< 42.96

Table 3.4 The Z_g cross-section of tooth pointing beginning of the concave spherical helical gear under different gear's lead angle λ_g

Basic gear parameters: $\alpha_n=20^\circ$, $T_g=22$ teeth, $r_w=30\text{mm}$				
Gear lead angle λ_g (deg.)	75	80	85	90
Z_g cross-sections (mm)	± 22.25	± 21.57	± 21.16	± 21
Suitable face width W (mm)	< 44.50	< 43.14	< 42.32	< 42

envelope to the two-parameter family of surfaces, the kinematic method to find the differentiated equations of meshing (Eqs. (3.20) and (3.21)) has been developed for investigating tooth undercutting of the proposed convex spherical helical gear. The characteristics and limit curves of tooth undercuts of the convex spherical helical gear under different design parameters were also studied and verified by five numerical examples (Examples 3.1~3.5). The tooth undercutting of the convex spherical helical gear can be avoided by design a gear set with a larger number of teeth or a larger pressure angle. Moreover, the condition equations of tooth pointing of the concave spherical helical gear had been developed. Based on the development condition equations of tooth pointing of the concave spherical helical gear, the Z_g cross-section of tooth pointing beginning of the gear under different design parameters were also investigated and verified by two numerical examples (Examples 3.6 and 3.7). Furthermore, the value of suitable face width of the concave spherical helical gear with tooth non-pointing had been also determined.

CHAPTER 4

Tooth Contact Analysis

4.1. Introduction

Gear sets are important machine elements used for power transmissions. The profile and assembly errors are two major factors that effect the gear kinematic errors. The profile errors include the errors of pressure angle, lead angle, tooth profile, etc. These errors relate to the manufacture of gears. Therefore, improving the precision of manufacture is an important issue to increase the gear transmission performance. Another important factor that effects the kinematic errors of the gear set is assembly errors. Assembly errors include the errors of center distance, axial shifted error along the tooth face width, vertical axial misalignment and horizontal axial misalignment. The tooth contact analysis (TCA) method was proposed by Litvin [3,4] and Litvin and Fuentes [5], and it had been applied to simulate the meshing situations of a gear set. The TCA results can provide useful information on the tooth contact loci, contact ratios and kinematic errors (KEs) of gear sets.

Due to the elasticity of gear tooth surfaces, the tooth surface contact point is spread over an elliptical area. It is known that the instantaneous contact point of the mating gear pair can be determined from the TCA results. When gear drives transmit a power or motion, a set of contact ellipses forms the bearing contacts on the tooth surfaces. Simulation methods for the analysis of contact ellipses can be classified into the elastic body method and the rigid body method. The finite element method belongs to the elastic body method for analyzing the contact area with consideration of elastic deformation of tooth surfaces due to the contact stress, thermal stress, and so on. On the other hand, the rigid body method for contact ellipse analysis includes the curvature analysis method [3-5] and the surface separation topology method [37].

In this chapter, based on the mathematical models of the spherical helical gear developed in Chapter 2, the influences of assembly errors of the spherical helical gear sets under parallel and crossed axes mounting modes and three mating combinations on kinematics errors are investigated. Moreover, the contact ellipses of the gear sets with assembly errors under two axes mounting modes and three mating combinations are obtained by using the surface separation topology method [37].

4.2. Meshing model for spherical helical gear set

Figure 4.1 shows the schematic diagram that the spherical helical pinion and gear are meshed with assembly errors. The crossed axes mounting mode of the spherical helical gear set can be considered by the relationship of coordinate systems $S_o(X_o, Y_o, Z_o)$ and $S_f(X_f, Y_f, Z_f)$. Moreover, the assembly errors can be simulated by changing the settings and orientations of the reference coordinate systems $S_h(X_h, Y_h, Z_h)$ and $S_v(X_v, Y_v, Z_v)$ with respect to the coordinate system $S_o(X_o, Y_o, Z_o)$. Coordinate systems $S_1(X_1, Y_1, Z_1)$ and $S_2(X_2, Y_2, Z_2)$ are attached to the spherical helical pinion and gear, respectively. When the spherical helical pinion and gear tooth surfaces are meshed with each other, ϕ'_1 and ϕ'_2 are the actual rotation angles of the spherical helical pinion and gear on the rotational axes Z_1 and Z_2 , respectively. The spherical helical pinion and gear are mounted as crossed axes mode with an angle γ_o called the crossing angle. The crossing angle γ_o is formed by pinion's and gear's rotation axes Z_1 and Z_2 . When the crossing angle γ_o of the spherical helical gear set equals zero degree, the gear set becomes mating under a parallel axes mounting mode. Moreover, to simulate the horizontal axial misalignment of pinion, it can be performed by rotating the coordinate system S_h about axis X_h through a misaligned angle $\Delta\gamma_h$ with respect to coordinate system S_f .

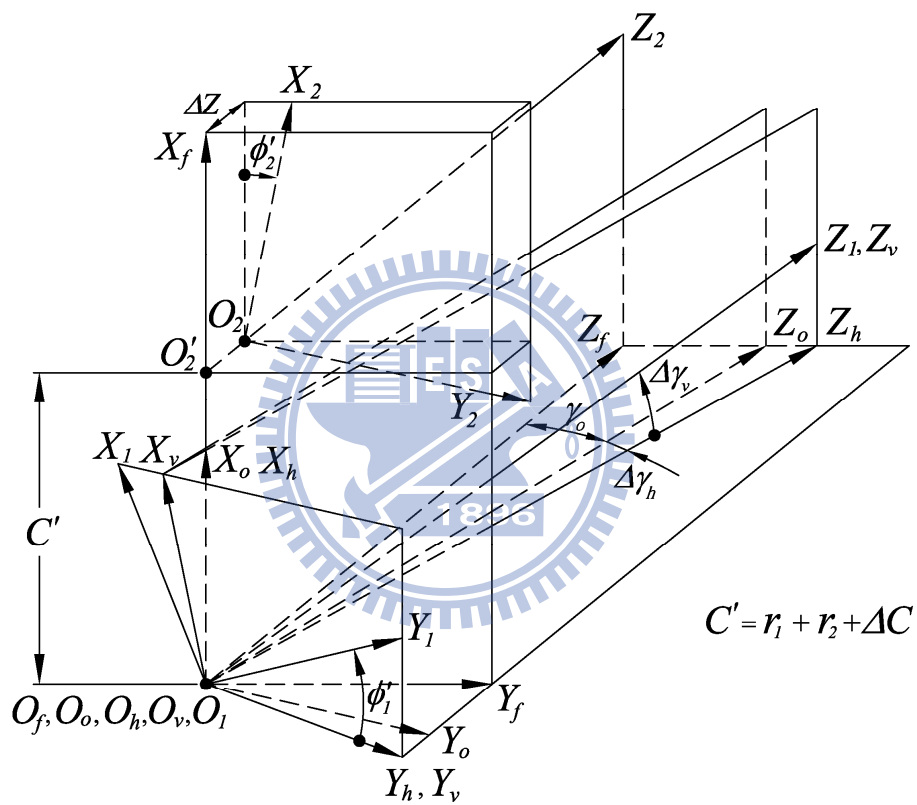


Fig. 4.1 Simulation of meshing for spherical helical gear set with assembly errors

Similarly, simulation of the vertical axial misalignment of pinion can be achieved by rotating the coordinate system S_v about axis X_v through a misaligned angle $\Delta\gamma_v$. Moreover, the center distance error of the spherical helical set can be performed by moving the coordinate system S_2 along axis X_f through a distance ΔC . Symbol ΔZ denotes the axial shifted error of the face width between the spherical helical pinion and gear tooth surfaces measured from point O'_2 to O_2 along the gear's rotation axis Z_2 . Where symbols $\Delta\gamma_h$, $\Delta\gamma_v$, ΔC and ΔZ represent the horizontal axial misaligned angle, vertical axial misaligned angle, center distance error and axial shifted error of the tooth face width of the gear set, respectively.

According to the TCA method [3-5], the position vectors and unit surface normal vectors of both pinion and gear should be represented in the same coordinate system, say S_f . Therefore, the instantaneous common contact point on the pinion and gear tooth surfaces is the same point in the fixed coordinate system S_f , as shown in Fig. 4.2. Moreover, the unit surface normal vectors of the pinion and gear must be collinear to each other. Therefore, the following equations must be observed at the point of tangency of the mating gear pair represented in the same fixed coordinate system:

$$\mathbf{R}_f^{(1)} - \mathbf{R}_f^{(2)} = \mathbf{0}, \quad (4.1)$$

$$\text{and } \mathbf{n}_f^{(1)} \times \mathbf{n}_f^{(2)} = \mathbf{0}, \quad (4.2)$$

where symbol $\mathbf{R}_f^{(j)}$ ($j=1$ and 2) denotes the position vector, while symbol $\mathbf{n}_f^{(j)}$ ($j=1$ and 2) indicates the unit surface normal vector of the spherical helical pinion and gear represented in coordinate system S_f . The position vector and unit surface normal vector of the spherical helical pinion represented in coordinate system S_g can be transformed to the fixed coordinate system S_f by applying the following homogeneous coordinate transformation matrix equations:

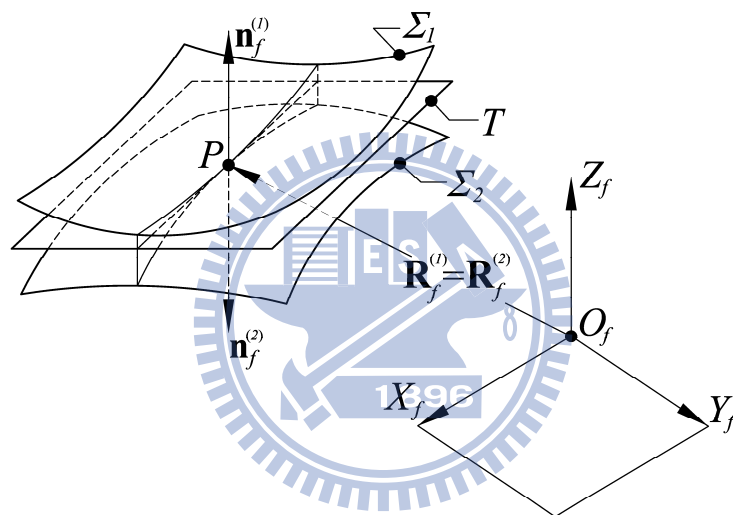


Fig. 4.2 Relationship among two contact teeth and their common tangent plane

$$\mathbf{R}_f^{(1)} = \mathbf{M}_{fo} \mathbf{M}_{oh} \mathbf{M}_{hv} \mathbf{M}_{vg} \mathbf{R}_g^{(1)}, \quad (4.3)$$

and

$$\mathbf{n}_f^{(1)} = \mathbf{L}_{fo} \mathbf{L}_{oh} \mathbf{L}_{hv} \mathbf{L}_{vg} \mathbf{n}_g^{(1)}, \quad (4.4)$$

where

$$\mathbf{M}_{vg} = \begin{bmatrix} \cos \phi'_l & \sin \phi'_l & 0 & 0 \\ -\sin \phi'_l & \cos \phi'_l & 0 & 0 \\ 0 & 0 & 1 & 0 \\ 0 & 0 & 0 & 1 \end{bmatrix}, \quad (4.5)$$

$$\mathbf{M}_{hv} = \begin{bmatrix} \cos \Delta\gamma_v & 0 & \sin \Delta\gamma_v & 0 \\ 0 & 1 & 0 & 0 \\ -\sin \Delta\gamma_v & 0 & \cos \Delta\gamma_v & 0 \\ 0 & 0 & 0 & 1 \end{bmatrix}, \quad (4.6)$$

$$\mathbf{M}_{oh} = \begin{bmatrix} 1 & 0 & 0 & 0 \\ 0 & \cos \Delta\gamma_h & \sin \Delta\gamma_h & 0 \\ 0 & -\sin \Delta\gamma_h & \cos \Delta\gamma_h & 0 \\ 0 & 0 & 0 & 1 \end{bmatrix}, \quad (4.7)$$

$$\mathbf{M}_{fo} = \begin{bmatrix} 1 & 0 & 0 & 0 \\ 0 & \cos \gamma_o & \sin \gamma_o & 0 \\ 0 & -\sin \gamma_o & \cos \gamma_o & 0 \\ 0 & 0 & 0 & 1 \end{bmatrix}, \quad (4.8)$$

$$\mathbf{L}_{vg} = \begin{bmatrix} \cos \phi'_l & \sin \phi'_l & 0 \\ -\sin \phi'_l & \cos \phi'_l & 0 \\ 0 & 0 & 1 \end{bmatrix}, \quad (4.9)$$

$$\mathbf{L}_{hv} = \begin{bmatrix} \cos \Delta\gamma_v & 0 & \sin \Delta\gamma_v \\ 0 & 1 & 0 \\ -\sin \Delta\gamma_v & 0 & \cos \Delta\gamma_v \end{bmatrix}, \quad (4.10)$$

$$\mathbf{L}_{oh} = \begin{bmatrix} 1 & 0 & 0 \\ 0 & \cos \Delta\gamma_h & \sin \Delta\gamma_h \\ 0 & -\sin \Delta\gamma_h & \cos \Delta\gamma_h \end{bmatrix}, \quad (4.11)$$

$$\text{and } \mathbf{L}_{f_o} = \begin{bmatrix} 1 & 0 & 0 \\ 0 & \cos \gamma_o & \sin \gamma_o \\ 0 & -\sin \gamma_o & \cos \gamma_o \end{bmatrix}. \quad (4.12)$$

Similarly, the position vector and unit surface normal vector of the spherical helical gear represented in coordinate system S_2 can be transformed to the fixed coordinate system S_f by applying the following homogeneous coordinate transformation matrix equations:

$$\mathbf{R}_f^{(2)} = \mathbf{M}_{fg} \mathbf{R}_g^{(2)}, \quad (4.13)$$

$$\text{and } \mathbf{n}_f^{(2)} = \mathbf{L}_{fg} \mathbf{n}_g^{(2)}, \quad (4.14)$$

where

$$\mathbf{M}_{fg} = \begin{bmatrix} \cos \phi'_2 & -\sin \phi'_2 & 0 & C' \\ \sin \phi'_2 & \cos \phi'_2 & 0 & 0 \\ 0 & 0 & 1 & \Delta Z \\ 0 & 0 & 0 & 1 \end{bmatrix}, \quad (4.15)$$

$$\text{and } \mathbf{L}_{fg} = \begin{bmatrix} \cos \phi'_2 & -\sin \phi'_2 & 0 \\ \sin \phi'_2 & \cos \phi'_2 & 0 \\ 0 & 0 & 1 \end{bmatrix}, \quad (4.16)$$

where symbol C' denotes the operational center distance of the spherical helical gear set with center distance error ΔC (i.e. $C' = r_g^{(1)} + r_g^{(2)} + \Delta C$).

Equations (4.1) and (4.2) give a general form of meshing model of the gear set with assembly errors under the parallel and crossed axes mounting modes. The mounting spherical helical pinion and gear may have their helices either with the same or the opposite direction, as shown in Fig. 4.3. Where symbols $\beta_g^{(l)}$ and $\lambda_g^{(l)}$

denoted in Fig. 4.3 indicate the helix and lead angle of the spherical helical pinion, while symbols $\beta_g^{(2)}$ and $\lambda_g^{(2)}$ denote the helix and lead angle of the spherical helical gear. Symbol γ_o of Fig. 4.3 denotes the crossing angle of the spherical helical gear set under crossed axes mounting mode. Moreover, the helix angles $\beta_g^{(1)}$ and $\beta_g^{(2)}$, if they are in opposite directions, are not equal as in the case of spherical helical gears with parallel axes mounting mode. The helix angles $\beta_g^{(1)}$ and $\beta_g^{(2)}$ and the crossing angle γ_o are related as [3-5]

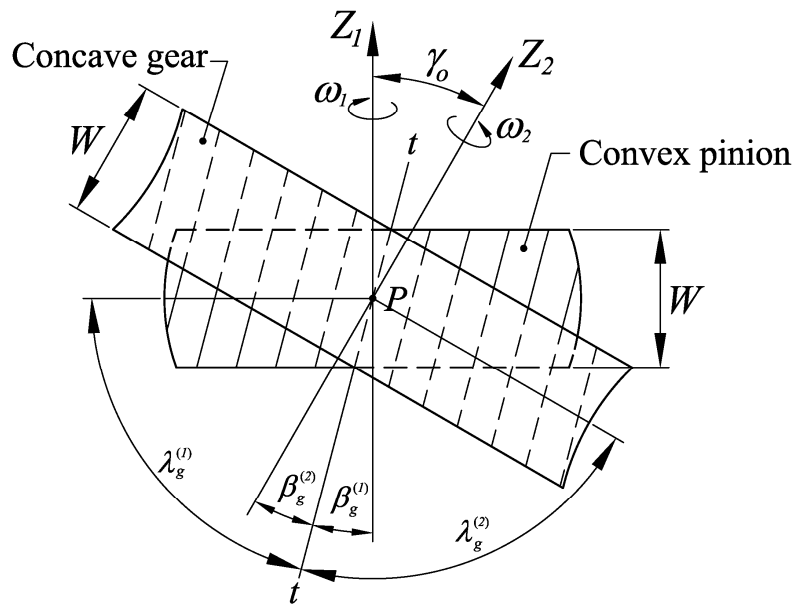
$$\gamma_o = \beta_g^{(1)} \pm \beta_g^{(2)}, \quad (4.17)$$

where the upper and lower “ \pm ” signs of Eq. (4.17) denote the spherical helical pinion and gear with the same and opposite helix directions, respectively.

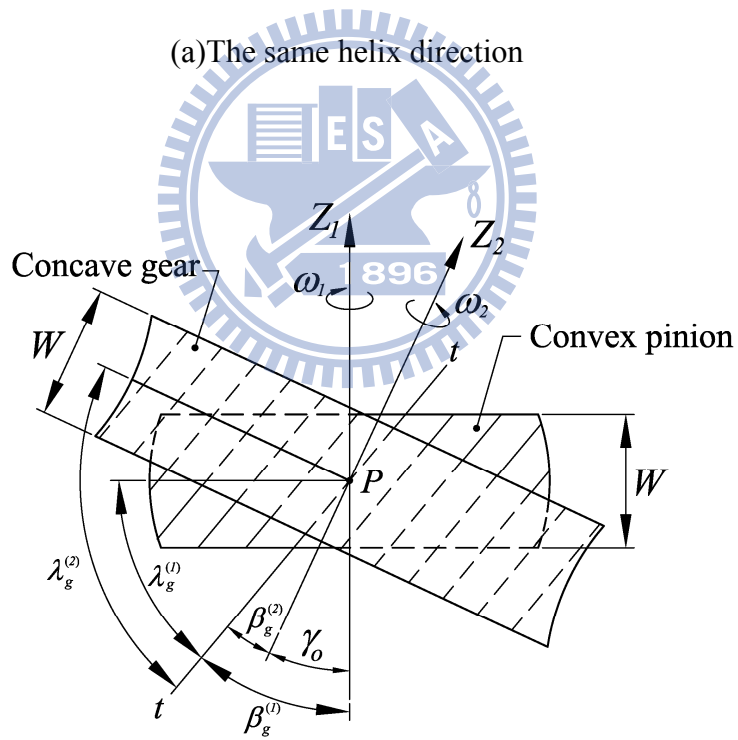
4.3. Kinematic errors

Considering two equations of meshing for the spherical helical pinion tooth surfaces, two equations of meshing for the spherical helical gear tooth surfaces, and Eqs. (4.1) and (4.2), these equations yield a system of nine independent equations with ten variables $l_b^{(1)}$, $l_b^{(2)}$, $\phi_w^{(1)}$, $\phi_w^{(2)}$, $\psi^{(1)}$, $\psi^{(2)}$, $\theta_s^{(1)}$, $\theta_s^{(2)}$, ϕ'_1 and ϕ'_2 , since $|\mathbf{n}_f^{(1)}| = |\mathbf{n}_f^{(2)}| = 1$. Superscripts 1 and 2 of the variables indicate the spherical helical pinion and gear, respectively. If the pinion's input rotation angle ϕ'_1 is given, another nine variables can be solved by using a nonlinear solver. By substituting the solved independent nine variables and the given spherical pinion's input rotation angle ϕ'_1 into Eqs. (4.3) and (4.5), the contact points on the spherical helical pinion and gear tooth surfaces can be obtained, respectively.

The kinematic error (KE) of the spherical helical gear set with assembly errors



(a) The same helix direction



(b) The opposite helix direction

Fig. 4.3 Mounting relationships of the spherical helical gear set under the crossed axes mounting mode

can be calculated by applying the following equation:

$$\Delta\phi'_2(\phi'_1) = \phi'_2(\phi'_1) - \frac{T_g^{(1)}}{T_g^{(2)}}\phi'_1, \quad (4.18)$$

where $T_g^{(j)}$ denotes the number of teeth of the spherical helical pinion ($j=1$) and gear ($j=2$), respectively.

4.4. Contact ratio

The contact ratio (CR) of a gear set can be defined by the gear's rotation angle, measured from the starting contact point to the end contact point, to be divided by the angle formed by two adjacent teeth. Therefore, the contact ratio m_c of the spherical helical gear set can be expressed by the following equation [3-5]:

$$m_c = \frac{\phi'_{IE} - \phi'_{IS}}{360^\circ T_1}, \quad (4.19)$$

where symbol ϕ'_{IS} denotes the rotational angle of the spherical helical pinion that corresponds to the starting contact point of the spherical helical gear set during meshing, while symbol ϕ'_{IE} indicates the rotational angle at the end of contact point for the same pinion tooth profile. The rotational angles ϕ'_{IS} and ϕ'_{IE} can be obtained by TCA simulations discussed in section 4.3.

4.5. Contact ellipses

According to the surface separation topology method [37], the tooth surfaces of the spherical helical pinion and gear must be transformed from the fixed coordinate system S_f of meshing model to the coordinate system $S_t(X_t, Y_t, Z_t)$. Herein, the coordinate system S_t is attached to the common tangent plane of the two contact tooth

surfaces at every contact instant. Figure 4.4 shows the relationship between the fixed coordinate system S_f and the common tangent plane coordinate system S_t . The coordinate system $S_m(X_m, Y_m, Z_m)$ and $S_n(X_n, Y_n, Z_n)$ are two auxiliary coordinate systems that are rotated about the axes X_m and Y_n through angles δ and ε , respectively. Therefore, the position vectors of the spherical helical pinion and gear tooth surfaces, represented in coordinate system S_t , can be obtained by the following homogenous coordinate transformation matrix equation:

$$\mathbf{R}_t^{(j)} = \mathbf{M}_m \mathbf{M}_{nm} \mathbf{M}_{mf} \mathbf{R}_f^{(j)}, \quad (4.20)$$

where

$$\mathbf{M}_{mf} = \begin{bmatrix} 1 & 0 & 0 & -p_x \\ 0 & 1 & 0 & -p_y \\ 0 & 0 & 1 & -p_z \\ 0 & 0 & 0 & 1 \end{bmatrix}, \quad (4.21)$$

$$\mathbf{M}_{nm} = \begin{bmatrix} 1 & 0 & 0 & 0 \\ 0 & \cos \delta & -\sin \delta & 0 \\ 0 & \sin \delta & \cos \delta & 0 \\ 0 & 0 & 0 & 1 \end{bmatrix}, \quad (4.22)$$

$$\text{and } \mathbf{M}_m = \begin{bmatrix} \cos \varepsilon & 0 & -\sin \varepsilon & 0 \\ 0 & 1 & 0 & 0 \\ \sin \varepsilon & 0 & \cos \varepsilon & 0 \\ 0 & 0 & 0 & 1 \end{bmatrix}. \quad (4.23)$$

Where superscript j appeared in Eq. (4.20) denotes the spherical helical pinion ($j=1$) and gear ($j=2$). Symbols p_x , p_y and p_z are three coordinate components of the instantaneous contact point of the two mating tooth surfaces expressed in the fixed coordinate system S_f . Moreover, the angle δ is formed by axes Z_m and Z_n , while the angle ε is formed by axes Z_n and Z_t . Therefore, the angles δ and ε can be obtained by:

$$\delta = \tan^{-1} \left(\frac{n_{f_y}^{(j)}}{n_{f_z}^{(j)}} \right), \quad (4.24)$$

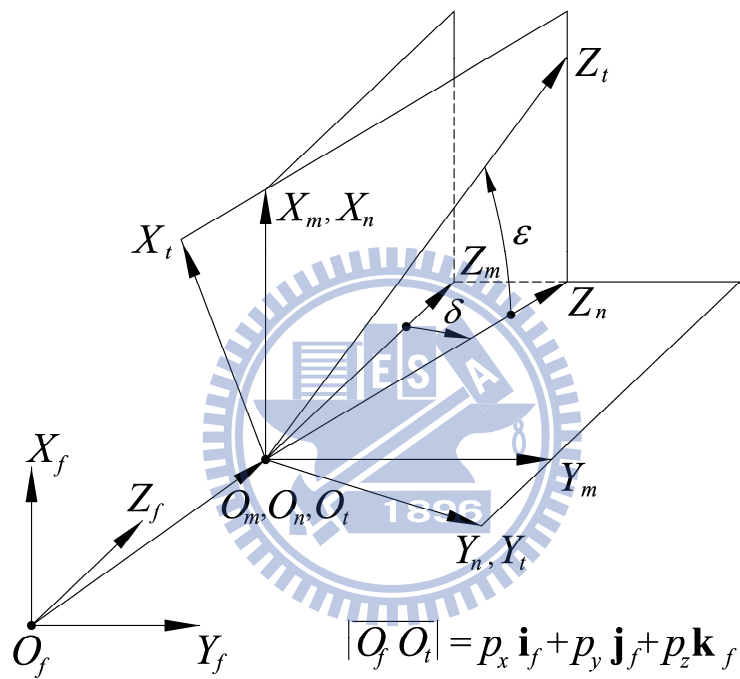
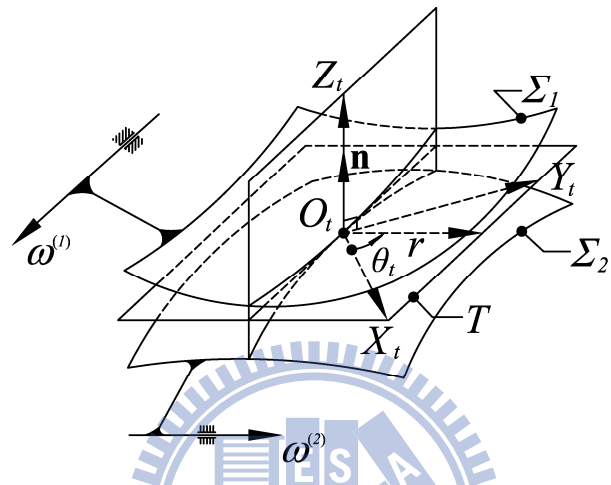


Fig. 4.4 Coordinate system relationship of the contact point and tangent plane

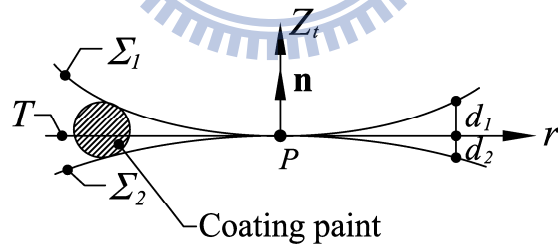
$$\text{and } \varepsilon = \tan^{-1} \left(\frac{n_{fx}^{(j)}}{\sqrt{n_{fy}^{(j)2} + n_{fz}^{(j)2}}} \right), \quad (4.25)$$

where $n_{fx}^{(j)}$, $n_{fy}^{(j)}$ and $n_{fz}^{(j)}$ symbolize the three components of the unit tooth surface normal vector $\mathbf{n}_f^{(j)}$ of the spherical helical pinion ($j=1$) and gear ($j=2$) at their instantaneous common contact point expressed in the fixed coordinate system S_f .

Figure 4.5 shows the contact tooth surfaces of pinion Σ_1 and gear Σ_2 which tangent to each other at their instantaneous contact point O_t . It is noted that the instantaneous contact point O_t can be determined by the TCA computation. In Fig. 4.5, symbol \mathbf{n} represents the unit surface normal vector of the pinion Σ_1 represented in coordinate system S_t and coincides with the Z_t axis. The calculation of the contact ellipses is based on the TCA results and polar coordinates concept. The geometric center of a contact ellipse is the instantaneous contact point of two mating tooth surfaces, determined by the TCA simulations. The geometric center is considered as the origin of the polar coordinate system. To determine a family of contour points of the contact ellipse, one should search a pair of polar coordinates (r, θ) , as shown in Fig. 4.5(a), beginning from axis X_t with an increment angle for θ , e.g. 2 degrees. The symbol r represents the position (polar coordinate) of the contact ellipse at the corresponding polar coordinate θ , expressed in the coordinate system S_t , and is located on the common tangent plane. The value of every position point r of the contact ellipse must satisfy the separation distance $(d_1+d_2)=0.00632\text{mm}$. Since the coating paint on the pinion tooth surfaces for bearing contact test will be scraped away and printed on the gear tooth surfaces when the distance, measured along Z_t axis, of two mating tooth surfaces (Σ_1 and Σ_2) is less than the paint's diameter, as shown in Fig. 4.5(b). Since the diameter of coating paint for bearing contact test is 0.00632mm , the separation distance is set to equal the diameter of the coating paint for simplicity.



(a) Common tangent plane and polar coordinates



(b) Separation distances between pinion and gear surfaces

Fig. 4.5 Schematic diagram for surface topology measurement

Herein, the symbol d_1 is the distance, measured along Z_1 direction, of Σ_1 and common tangent plane T , whereas the symbol d_2 is the distance between Σ_2 and common tangent plane T . Therefore, the contact ellipses of the spherical helical gear set can be determined by applying the following equations:

$$X_t^{(1)} = X_t^{(2)} = r \cos \theta_t \quad (-\pi \leq \theta_t \leq \pi), \quad (4.26)$$

$$Y_t^{(1)} = Y_t^{(2)} = r \sin \theta_t \quad (-\pi \leq \theta_t \leq \pi), \quad (4.27)$$

$$\text{and } |Z_t^{(1)} - Z_t^{(2)}| = 0.00632 \text{ mm}. \quad (4.28)$$

Thus, the position and size of contact ellipses of the spherical helical gear set can be determined by using Eqs. (4.26)~(4.28).

4.6. Numerical examples for gear meshing simulations

In this section, the contact situations (KEs, CRs, contact loci and bearing contacts) of the spherical helical gear sets under two axes mounting modes and three mating combinations have been discussed by the following numerical examples. Figures 4.6(a) and 4.6(b) show two axes modes of gear mounting for spherical helical gear sets with parallel and crossed axes mounting modes, respectively. Moreover, the effects of gear assembly errors ($\Delta\gamma_h$, $\Delta\gamma_v$, ΔC and ΔZ) on the contact situations of the spherical helical gear sets are also studied by the numerical examples. The gear meshing simulations for the spherical helical gear sets under two axes mounting modes are discussed in subsections 4.6.1 and 4.6.2, respectively.

4.6.1 Spherical helical gear sets under parallel axes mounting mode

In this subsection, the KEs, contact ratios (CRs), contact loci and bearing contacts of the spherical helical gear sets under parallel axes mounting mode and

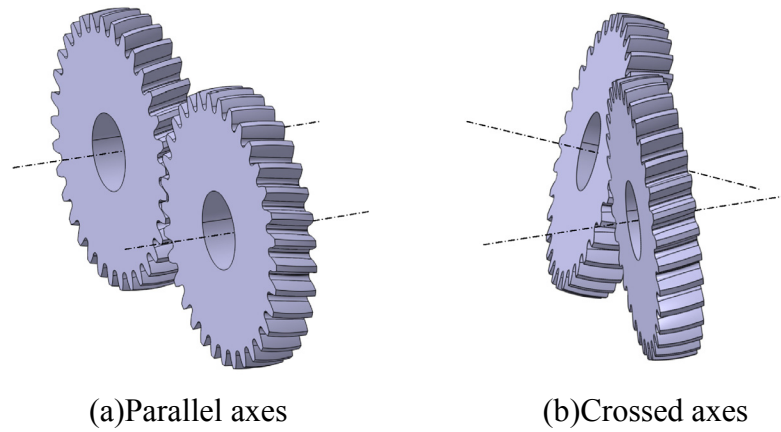


Fig. 4.6 Two axes mounting modes of the spherical helical gear sets

three mating combinations are studied by five numerical examples (Examples 4.1~4.5).

Example 4.1: KEs and contact ellipses of a spherical helical gear set with convex pinion and convex gear meshing under parallel axes mounting mode and different assembly conditions

The major design parameters of the hob cutter, convex pinion and convex gear are given in Table 4.1. In addition, the spherical helical gear set under parallel axes mounting mode is assembled with four conditions as follows:

Case 1: $\Delta\gamma_v = \Delta\gamma_h = 0^\circ$ and $\Delta C = \Delta Z = 0$ mm (ideal assembly condition)

Case 2: $\Delta\gamma_v = \Delta\gamma_h = 0^\circ$, $\Delta Z = 0$ mm and $\Delta C = 0.5$ mm (0.3% of center distance variation)

Case 3: $\Delta\gamma_v = \Delta\gamma_h = 0^\circ$, $\Delta C = 0$ mm and $\Delta Z = 0.5$ mm (2.5% of axial shifting variation)

Case 4: $\Delta\gamma_v = 2^\circ$, $\Delta\gamma_h = 0.5^\circ$, $\Delta C = 0$ mm and $\Delta Z = 0$ mm

Case 1 is an ideal assembly condition, it means that there are no assembly errors for the spherical helical gear set with convex pinion and convex gear. Case 2 indicates

Table 4.1 Major design parameters of hob cutter, pinion and gear for spherical helical gear sets under parallel axes mounting mode

Types of gear	Hob	Pinion Gear			
		Convex	Convex	Concave	Helical
Normal module m_n (mm/tooth)	4	4	4	4	4
Number of teeth T_j	1	33	47	47	47
Normal pressure angle α_n (deg.)	20	20	20	20	20
Lead angle λ_g (deg.)	3.823 RH	75 RH	75 LH	75 LH	75 LH
Face width W (mm)	-	20	20	20	20
Pitch radius r_j (mm)	30	68.328	97.316	97.316	97.316
Spherical radius R_s (mm)	-	68.328	97.316	97.316	-
Cutting radius R_c (mm)	-	98.328	127.316	67.316	-
Center distance C (mm)	-	-	165.644	165.644	165.644

that the spherical helical gear set has center distance assembly error. Case 3 denotes the axial shifting of the face width between the pinion and gear tooth surfaces. Case 4 indicates that the gear set has both vertical and horizontal axial misalignments. Figure 4.7 illustrates the KEs of the spherical helical gear set with convex pinion and convex gear under above-mentioned four assembly conditions (i.e. Cases 1~4). Meanwhile, Fig. 4.8 reveals a set of contact ellipses and loci on the pinion (Fig. 4.8(a)) and gear (Fig. 4.8(b)) tooth surfaces of the spherical helical gear set called the bearing contacts.

It is found that the spherical helical gear set with convex pinion and convex gear has a lower level of KEs under the ideal assembly condition (Case 1), and the bearing contacts are located on the middle region of the pinion's and gear's face width. The contact loci are all near to the central section of the pinion's and gear's face width. If the spherical helical gear set is assembled with a center distance variation (Case 2), there is also a lower level of KEs in meshing. By comparing Case 2 with Case 1, the bearing contact and the contact locus of the spherical helical gear set of Case 2 have a small shift to the top land of pinion. However, the bearing contact of the spherical helical gear set shown in Case 2 is still located on the middle region of the face width.

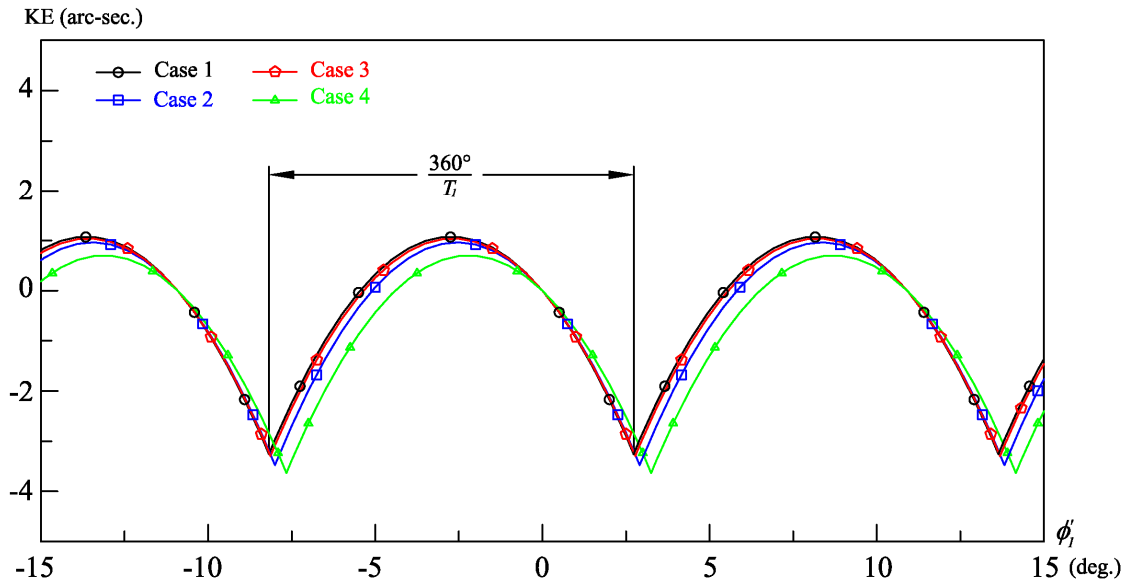


Fig. 4.7 KEs of the spherical helical gear set with convex pinion and convex gear under parallel axes mounting mode and different assembly conditions

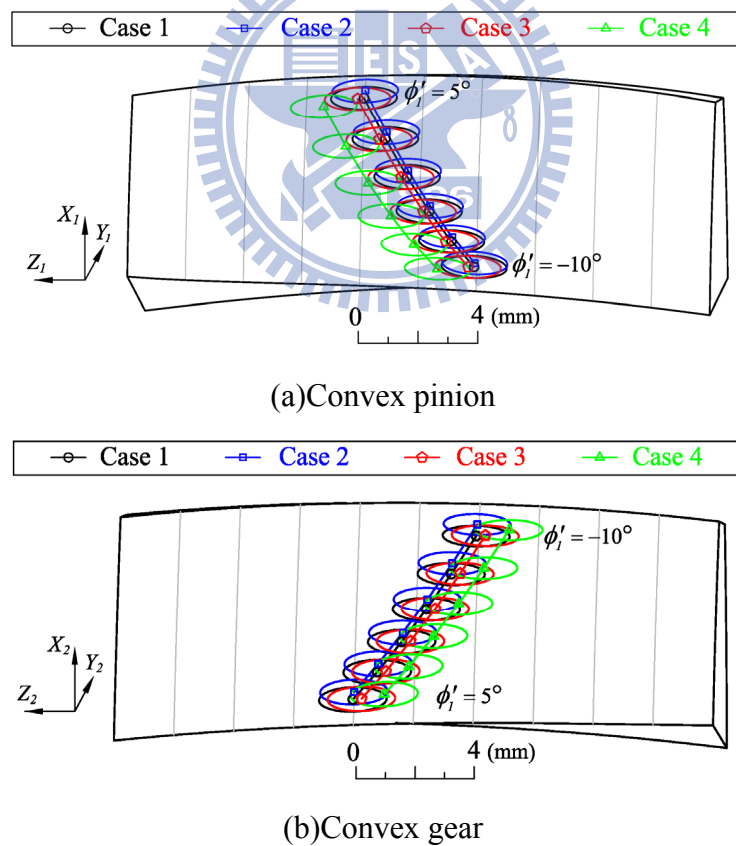


Fig. 4.8 Contact ellipses and contact loci on tooth surfaces of the spherical helical gear set under parallel axes mounting mode and different assembly conditions

According to the simulation results shown in Fig. 4.7, the assembly condition of Case 3 also results in a lower level KEs, while the bearing contacts and the contact loci are all shifted a small distance away from the middle region, as shown in Fig. 4.8. Case 4 has a little higher level of KEs and a larger amount of shifting of the bearing contact than other three assembly conditions (Cases 1~3). However, the bearing contacts of Case 4 are still located near by the middle region of the face width. Moreover, the positions of contact loci and bearing contacts of the spherical helical gear set of Cases 1, 2 and 3 are almost the same.

Example 4.2: KEs and contact ellipses of a spherical helical gear set with convex pinion and concave gear under parallel axes mounting mode and different assembly conditions

The major design parameters of the hob cutter, convex pinion and concave gear are also given in Table 4.1. Moreover, the spherical helical gear set is assembled with four conditions as follows:

Case 5: $\Delta\gamma_v = \Delta\gamma_h = 0^\circ$ and $\Delta C = \Delta Z = 0 \text{ mm}$ (ideal assembly condition)

Case 6: $\Delta\gamma_v = \Delta\gamma_h = 0^\circ$, $\Delta Z = 0 \text{ mm}$ and $\Delta C = 0.5 \text{ mm}$ (0.3% of center distance variation)

Case 7: $\Delta\gamma_v = \Delta\gamma_h = 0^\circ$, $\Delta C = 0 \text{ mm}$ and $\Delta Z = 0.5 \text{ mm}$ (2.5% of axial shifting variation)

Case 8: $\Delta\gamma_v = 2^\circ$, $\Delta\gamma_h = 0.5^\circ$, $\Delta C = 0 \text{ mm}$ and $\Delta Z = 0 \text{ mm}$

Case 5 is the ideal assembly condition, and it means that there are no assembly errors for the spherical helical gear set with convex pinion and concave gear. Case 6 indicates that the spherical helical gear set has a center distance assembly error. Case 7 denotes an axial shifting of the face width between the pinion and gear tooth

surfaces. Case 8 indicates that the gear set has both vertical and horizontal axial misalignments. Figure 4.9 illustrates the KEs of the spherical helical gear set with convex pinion and concave gear meshing under four assembly conditions (i.e. Cases 5~8), while Fig. 4.10 shows a set of contact ellipses and loci on the pinion tooth surface of the spherical helical gear set.

Observing Case 5 of Figs. 4.9 and 4.10, there is a lower level of KEs (ideal assembly condition), and the bearing contacts are located near by the middle region of the face width. Cases 6 and 7 also reveal a lower level of KEs, and the bearing contacts of the mating gear sets (Cases 6 and 7) are still located near by the middle region of the face width. However, when compared with that of Case 5, the bearing contact of Case 7 has a larger shifting than that of Case 6. Moreover, Case 8 has the largest position shifting of bearing contact in this example. The KEs of Case 8 are almost the same as those of other three assembly conditions in this example.

Example 4.3: KEs and contact ellipses of a gear set with convex spherical helical pinion and conventional helical gear under parallel axes mounting mode and different assembly conditions

The major design parameters of the hob cutter, convex spherical helical pinion and helical gear are also given in Table 4.1. In addition, the gear set is assembled with four conditions as follows:

Case 9: $\Delta\gamma_v = \Delta\gamma_h = 0^\circ$ and $\Delta C = \Delta Z = 0 \text{ mm}$ (ideal assembly condition)

Case 10: $\Delta\gamma_v = \Delta\gamma_h = 0^\circ$, $\Delta Z = 0 \text{ mm}$ and $\Delta C = 0.5 \text{ mm}$ (0.3% of center distance variation)

Case 11: $\Delta\gamma_v = \Delta\gamma_h = 0^\circ$, $\Delta C = 0 \text{ mm}$ and $\Delta Z = 0.5 \text{ mm}$ (2.5% of axial shifting variation)

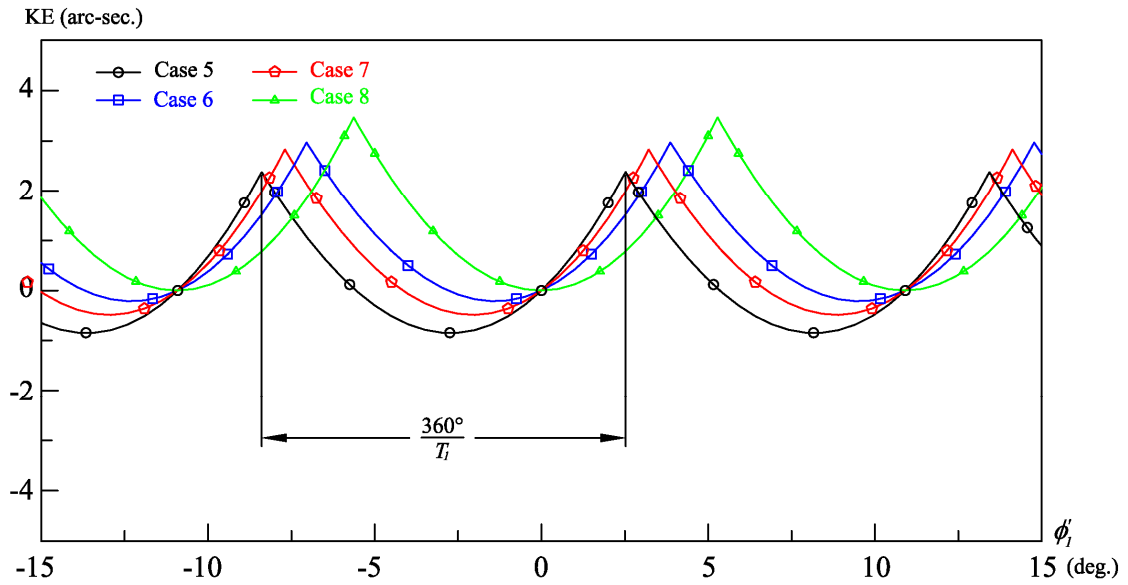


Fig. 4.9 KEs of the spherical helical gear set with convex pinion and concave gear under parallel axes mounting mode and different assembly conditions

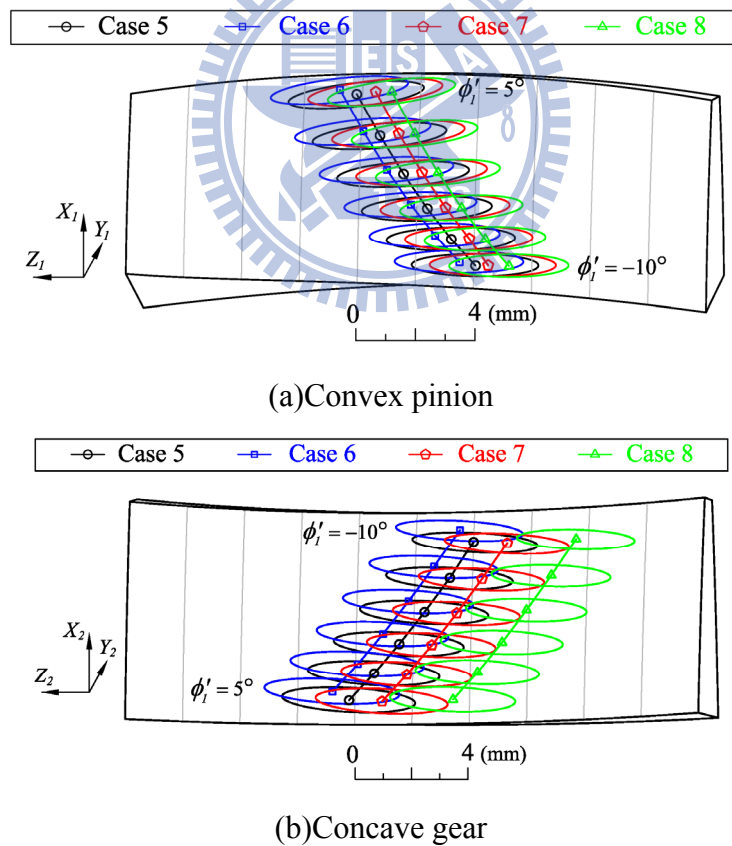


Fig. 4.10 Contact ellipses and contact loci on tooth surfaces of the spherical helical gear set under parallel axes mounting mode and different assembly conditions

Case 12: $\Delta\gamma_v = 2^\circ$, $\Delta\gamma_h = 0.5^\circ$, $\Delta C = 0\text{mm}$ and $\Delta Z = 0\text{mm}$

Case 9 is the ideal assembly condition, and it means that there are no assembly errors for the gear set with convex spherical helical pinion and conventional helical gear. Case 10 indicates that the gear set has a center distance assembly error. Case 11 denotes an axial shifting of the face width between the pinion and gear tooth surfaces. Case 12 indicates that the gear set has both axial vertical and horizontal misalignments. Figure 4.11 illustrates the KEs of the gear set with convex spherical helical pinion and conventional helical gear meshing under four assembly conditions (i.e. Cases 9~12), while Fig. 4.12 shows a set of contact ellipses on the pinion tooth surface.

It is found that Case 9 has a lower level of KEs, and the bearing contacts of Case 9 are located near by the middle region of the face width. Comparing with that of Case 9, the KEs shown in Cases 10-12 are almost the same. The bearing contacts of Cases 10 and 11 are similar to that of Case 9, but the bearing contacts of Case 12 are shifted a small distance from the middle region of the face width on pinion's tooth surface.

Comparing the KEs of Example 4.3 with those of Examples 4.1 and 4.2, all of the assembly conditions of the spherical helical gear set with convex pinion and concave gear (Example 4.2) have a lower level KEs than other corresponding assembly conditions in Examples 4.1 and 4.3. For example, in the ideal assembly conditions (Cases 1, 5 and 9), Case 5 has a lower level of KEs than other ideal assembly conditions. Moreover, all the assembly conditions discussed in Example 4.2 have a larger size of contact ellipse than other assembly conditions of Examples 4.1 and 4.3, since the mating tooth surfaces of pinion and gear of Example 4.2 are convex tooth surface mating with concave tooth surface.

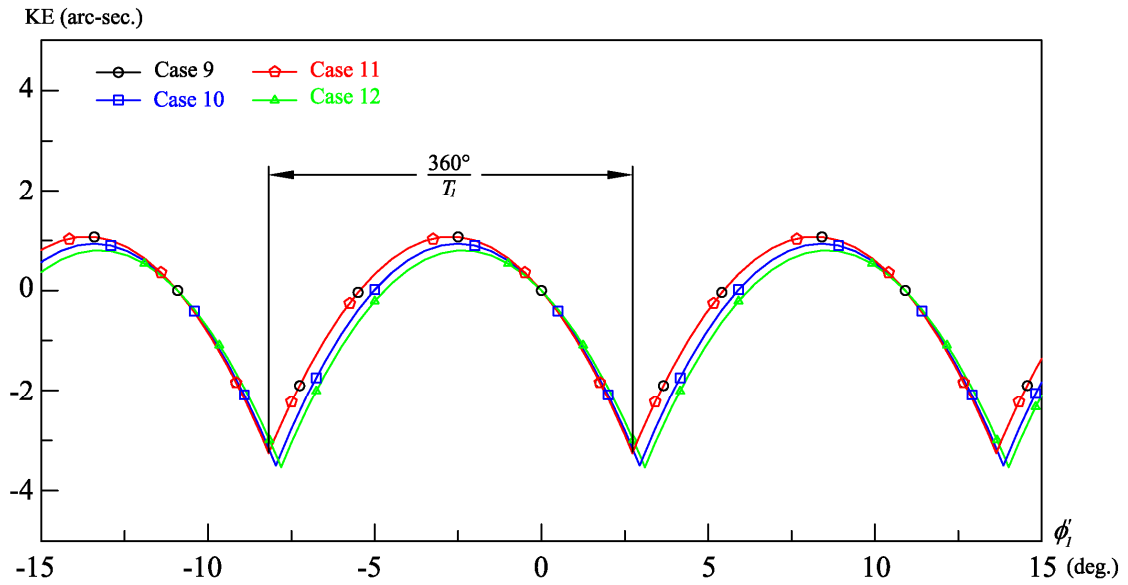


Fig. 4.11 KEs of the gear set with convex pinion and conventional helical gear under parallel axes mounting mode and different assembly conditions

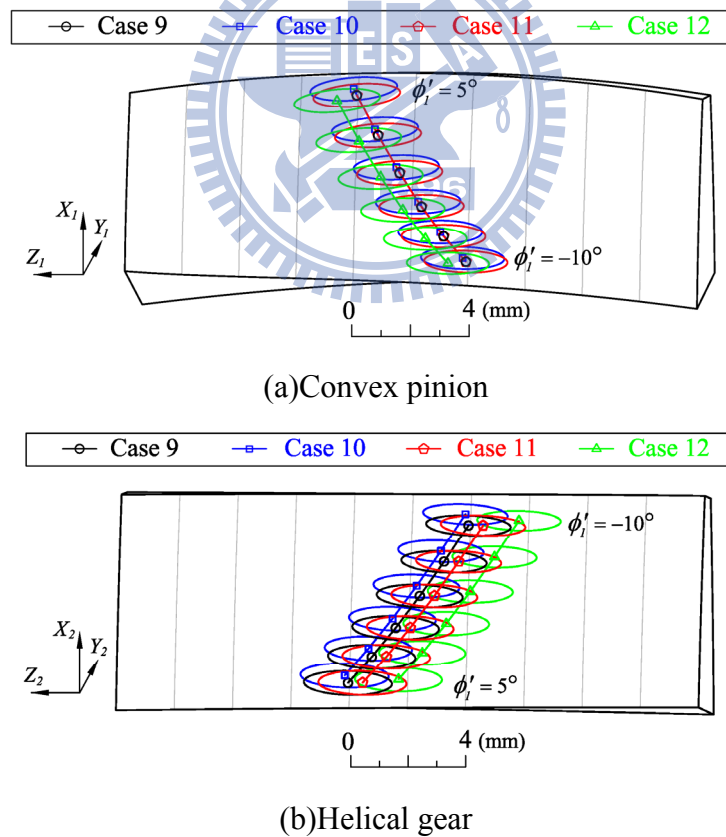


Fig. 4.12 Contact ellipses and contact loci on tooth surfaces of the gear set under parallel axes mounting mode and different assembly conditions

Example 4.4: Contact ratios of the spherical helical gear set under parallel axes mounting mode and three mating combinations

Some major design parameters of the hob cutter and three mating combinations of spherical helical gear sets are summarized in Table 4.1. Moreover, three mating combinations of the spherical helical gear sets are all assembled under ideal condition and axial misalignments $\Delta\gamma_v = 2^\circ$ and $\Delta\gamma_h = 0.5^\circ$.

Table 4.2 summarizes the contact ratios (CRs) and the rotation angles (ϕ'_{IS} and ϕ'_{IE}) of starting contact and end contact of the pinion tooth surface during the meshing of the spherical helical gear sets. The CRs of the spherical helical gear sets under three mating combinations with the ideal assembly condition and axial misalignments $\Delta\gamma_v = 2^\circ$ and $\Delta\gamma_h = 0.5^\circ$ are about 1.7. Comparing with the ideal assembly condition, the spherical helical gear set with vertical and horizontal axial misalignments ($\Delta\gamma_v = 2^\circ$ and $\Delta\gamma_h = 0.5^\circ$) has only a slightly influence on their CRs.

Example 4.5: Average ratio a/b of the major and minor axes of the contact ellipses of spherical helical gear sets under parallel axes mounting mode and different assembly conditions

In this example, the averages of a set of ratio a/b of the major and minor axes of the contact ellipses of the spherical helical gear sets during the pinion's tooth meshing cycle from ϕ'_{IS} to ϕ'_{IE} (see section 4.4) are determined. Where the ratio a/b indicates the ratio of major and minor axes of a contact ellipse of a spherical helical gear set at its meshing instant. The major design parameters of the hob cutter and three mating combinations of the spherical helical gear set are chosen the same as those shown in Table 4.1. Moreover, two assembly conditions, ideal assembly condition and axial misalignments ($\Delta\gamma_v = 2^\circ$ and $\Delta\gamma_h = 0.5^\circ$), are assembled under

Table 4.2 Contact ratios and rotation angles of the spherical helical gear sets under parallel axes mounting mode and two different assembly conditions

Mating combinations	Ideal assembly condition	Axial misalignments
Convex pinion with Convex gear	1.75 (-12.4°~6.7°)	1.73 (-11.8°~7.1°)
Convex pinion with Concave gear	1.71 (-12.3°~6.4°)	1.71 (-12.5°~6.2°)
Convex pinion with Helical gear	1.76 (-12.5°~6.7°)	1.74 (-12°~7°)

Table 4.3 Average ratio a/b and rotation angles of major and minor axes of contact ellipses of the spherical helical gear sets under parallel axes mounting mode and two different assembly conditions

Mating combinations	Ideal assembly condition	Axial misalignments
Convex pinion with Convex gear	2.88	2.90
Convex pinion with Concave gear	5.09	4.82
Convex pinion with Helical gear	3.7	3.69

three mating combinations for spherical helical gear sets.

Table 4.3 lists the average ratio a/b of the major and minor axes of the contact ellipse a/b for three mating combinations of spherical helical gear sets with different assembly conditions when the pinion's rotation angles are $\phi'_i = -10^\circ \sim 5^\circ$ with an increment angle, e.g. 0.1 degree. The gear set of having convex pinion mating with concave gear has a larger average ratio a/b than other two mating combinations. Moreover, the condition of convex pinion mating with convex gear has a smaller level of average ratio a/b than other two mating combinations. Comparing with the ideal assembly condition, the average ratio a/b is not sensitive to axial misalignments for the mating combinations of convex pinion with convex gear and convex pinion with conventional helical gear. However, the spherical helical gear set of convex pinion mating with concave gear has a larger variation of the a/b ratio than other two mating

combinations under the ideal assembly condition and axial misalignments.

4.6.2 Spherical helical gear sets under crossed axes mounting mode

In this subsection, the KEs, CRs, contact loci and bearing contacts of the spherical helical gear sets with crossed axes mounting mode under three mating combinations are investigated by five numerical examples (Examples 4.6~4.10). According to Eq. (4.17) and the pinion's and gear's design parameters (see Table 4.4) of the spherical helical gear sets, the crossing angle γ_o of the gear set for Examples 4.6~4.10 is defined as 30 degrees (i.e. $\gamma_o = \beta_g^{(1)} + \beta_g^{(2)} = 30^\circ$).

Example 4.6: KEs and contact ellipses of a spherical helical gear set with convex pinion and convex gear meshing under crossed axes mounting mode and different assembly conditions

The major design parameters of the hob cutter, convex pinion and convex gear are given in Table 4.4. The assembly conditions of the spherical helical gear set with convex pinion and convex gear under crossed axes mounting mode (i.e. $\gamma_o = 30^\circ$) are chosen the same as those of given in Example 4.1 and listed as follows:

Case 13: $\Delta\gamma_v = \Delta\gamma_h = 0^\circ$ and $\Delta C = \Delta Z = 0$ mm (ideal assembly condition)

Case 14: $\Delta\gamma_v = \Delta\gamma_h = 0^\circ$, $\Delta Z = 0$ mm and $\Delta C = 0.5$ mm (0.3% of center distance variation)

Case 15: $\Delta\gamma_v = \Delta\gamma_h = 0^\circ$, $\Delta C = 0$ mm and $\Delta Z = 0.5$ mm (2.5% of axial shifting variation)

Case 16: $\Delta\gamma_v = 2^\circ$, $\Delta\gamma_h = 0.5^\circ$, $\Delta C = 0$ mm and $\Delta Z = 0$ mm

Table 4.4 Major design parameters of hob cutter, pinion and gears for spherical helical gear sets under crossed axes mounting mode

Types of gear	Hob	Pinion Gear			
		Convex	Convex	Concave	Helical
Normal module m_n (mm/tooth)	4	4	4	4	4
Number of teeth T_j	1	33	47	47	47
Normal pressure angle α_n (deg.)	20	20	20	20	20
Lead angle λ_g (deg.)	3.823 RH	75 RH	75 RH	75 RH	75 RH
Helix angle $\beta_g^{(j)}$ (deg.)	-	15 RH	15 RH	15 RH	15 RH
Face width W (mm)	-	20	20	20	20
Pitch radius r_j (mm)	30	68.328	97.316	97.316	97.316
Spherical radius R_s (mm)	-	68.328	97.316	97.316	-
Cutting radius R_c (mm)	-	98.328	127.316	67.316	-
Center distance C (mm)	-	-	165.644	165.644	165.644

Figure 4.13 illustrates the KEs of the spherical helical gear set with convex pinion and convex gear under crossed axes mounting mode $\gamma_o = 30^\circ$ and above-mentioned four assembly conditions (i.e. Cases 13~16). Meanwhile, Fig. 4.14 reveals a set of contact ellipses and their loci on the convex pinion (Fig. 4.14(a)) and convex gear (Fig. 4.14(b)) tooth surfaces of the spherical helical gear set.

It is found that the spherical helical gear set (with convex pinion and convex gear) with crossed axes has a lower level of KEs under the ideal assembly condition (Case 13), and the bearing contacts are located on the middle region of the pinion's and gear's face widths. If the spherical helical gear set with crossed axes is assembled with a center distance variation (Case 14), there has also a lower level of KEs in meshing. By comparing Case 14 with Case 13, the bearing contact and the contact locus of the spherical helical gear set of Case 14 have a small shift to the top land of pinion. However, the bearing contact of the spherical helical gear set in Case 14 is still located on the middle region of the face width. According to the simulation results

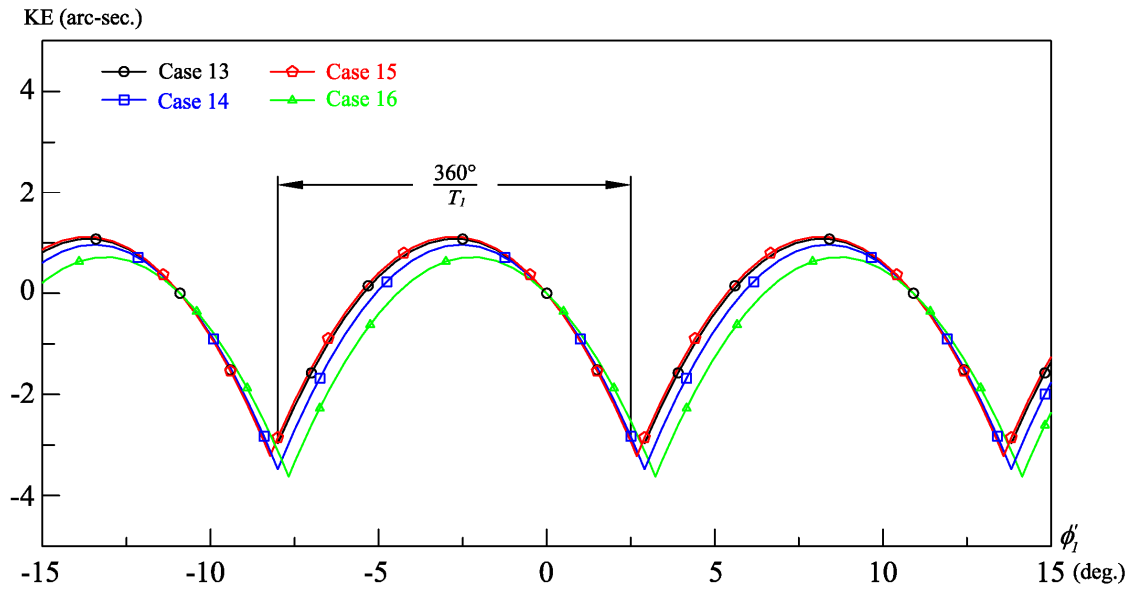
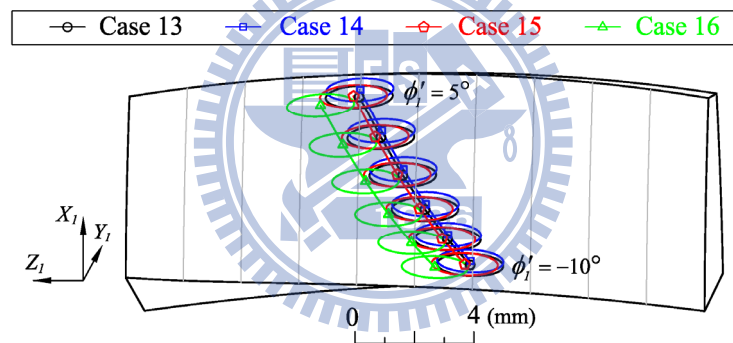
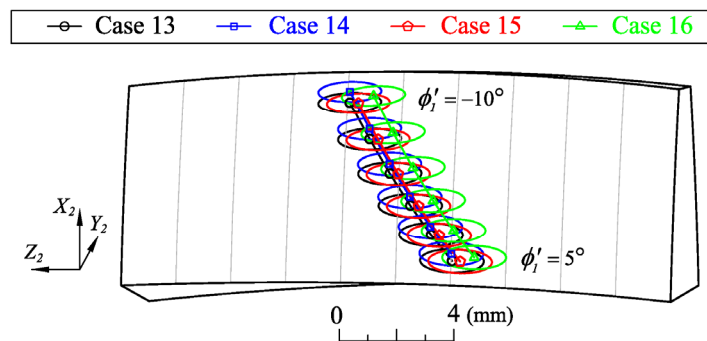


Fig. 4.13 KEs of the spherical helical gear set with convex pinion and convex gear under crossed axes mounting mode and different assembly conditions



(a) Convex pinion



(b) Convex gear

Fig. 4.14 Contact ellipses and contact loci on tooth surfaces of the spherical helical gear set under crossed axes mounting mode and different assembly conditions

shown in Fig. 4.13, the assembly condition of Case 15 also results in a lower level of KEs, while the bearing contacts and the contact loci are all shifted a small distance away from the middle region, as shown in Fig. 4.14. Case 16 has a little higher level of KEs than other three assembly conditions. There is a larger amount of shifting of the bearing contact and the contact locus of the spherical helical gear set than other three assembly conditions for the Case 16. However, the bearing contacts are still located near by the middle region of the face width. Moreover, the positions of contact locus and bearing contacts of the spherical helical gear set of Cases 13, 14 and 15 are almost the same.

Example 4.7: KEs and contact ellipses of a spherical helical gear set with convex pinion and concave gear under crossed axes mounting mode and different assembly conditions

The major design parameters of the hob cutter, convex pinion and concave gear are also given in Table 4.4. The assembly conditions of the spherical helical gear set with convex pinion and concave gear under crossed axes mounting mode (i.e. $\gamma_o = 30^\circ$) are chosen the same as those of given in Example 4.2 and listed as follows:

Case 17: $\Delta\gamma_v = \Delta\gamma_h = 0^\circ$ and $\Delta C = \Delta Z = 0$ mm (ideal assembly condition)

Case 18: $\Delta\gamma_v = \Delta\gamma_h = 0^\circ$, $\Delta Z = 0$ mm and $\Delta C = 0.5$ mm (0.3% of center distance variation)

Case 19: $\Delta\gamma_v = \Delta\gamma_h = 0^\circ$, $\Delta C = 0$ mm and $\Delta Z = 0.5$ mm (2.5% of axial shifting variation)

Case 20: $\Delta\gamma_v = 2^\circ$, $\Delta\gamma_h = 0.5^\circ$, $\Delta C = 0$ mm and $\Delta Z = 0$ mm

Figure 4.15 illustrates the KEs of the spherical helical gear set with convex

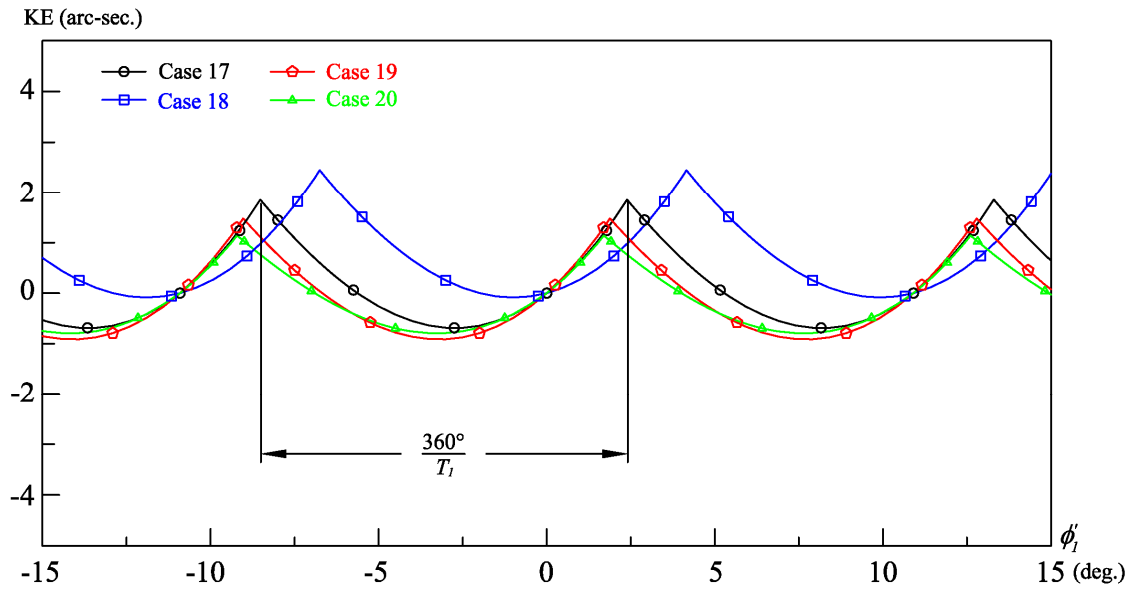


Fig. 4.15 KEs of the spherical helical gear set with convex pinion and concave gear under crossed axes mounting mode and different assembly conditions

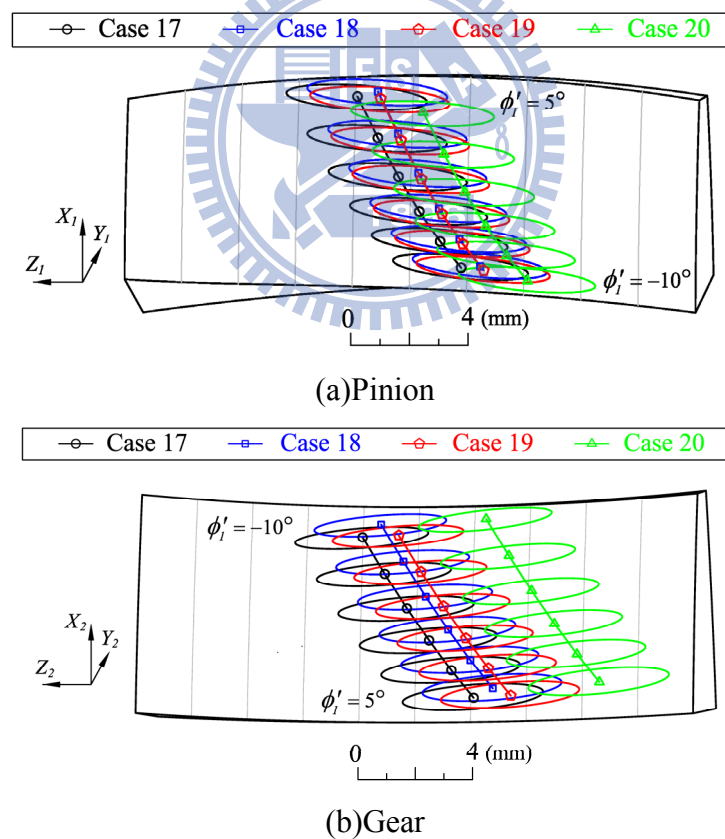


Fig. 4.16 Contact ellipses and contact loci on tooth surfaces of the spherical helical gear set under crossed axes mounting mode and different assembly conditions

pinion and concave gear under crossed axes mounting mode and four assembly conditions (Cases 17~20), while Fig. 4.16 shows a set of contact ellipses on the pinion (Fig. 4.16(a)) and gear (Fig. 4.16(b)) tooth surfaces of the spherical helical gear set.

Observing Case 17 of Figs. 4.15 and 4.16, there is a lower level of KEs (ideal assembly condition), and the bearing contacts are located near by the middle region of the face width. Cases 18 and 19 also reveal a lower level of KEs, and the bearing contacts of the mating gear sets are still located near by the middle region of the face width. However, when compared with that of Case 17, the bearing contact of Case 19 has a larger shifting than that of Cases 17 and 18. Moreover, Case 20 has the largest position shifting of bearing contact in this example. However, the KEs of Case 20 are almost the same as those of other three conditions in this example.

Example 4.8: A gear set with convex spherical helical pinion and conventional helical gear under crossed axes mounting and different assembly conditions

The major design parameters of the hob cutter, convex spherical helical pinion and helical gear are also given in Table 4.1. In addition, the gear set is assembled with four conditions as follows:

Case 21: $\Delta\gamma_v = \Delta\gamma_h = 0^\circ$ and $\Delta C = \Delta Z = 0$ mm (ideal assembly condition)

Case 22: $\Delta\gamma_v = \Delta\gamma_h = 0^\circ$, $\Delta Z = 0$ mm and $\Delta C = 0.5$ mm (0.3% of center distance variation)

Case 23: $\Delta\gamma_v = \Delta\gamma_h = 0^\circ$, $\Delta C = 0$ mm and $\Delta Z = 0.5$ mm (2.5% of axial shifting variation)

Case 24: $\Delta\gamma_v = 2^\circ$, $\Delta\gamma_h = 0.5^\circ$, $\Delta C = 0$ mm and $\Delta Z = 0$ mm

Figure 4.17 illustrates the KEs of the gear set (with convex spherical helical pinion and conventional helical gear) with crossed axes mounting mode (i.e.

$\gamma_o = 30^\circ$) under four assembly conditions (Cases 21~24), while Fig. 4.18 shows a set of contact ellipses on the pinion and gear tooth surfaces.

It is found that Case 21 has a lower level of KEs, and the bearing contacts of Case 21 are located near by the middle region of the face width. Comparing with that of Case 21, the KEs shown in Cases 22-24 are almost the same. The bearing contacts of Cases 23 and 24 are similar to that of Case 21, but the bearing contacts of Case 24 are shifted a small distance from the middle region of the face width on pinion's tooth surface.

Comparing the KE of Example 4.8 with those of Examples 4.6 and 4.7, all of the assembly conditions of the spherical helical gear set with convex pinion and concave gear (Example 4.7) have lower level of KEs than other corresponding assembly conditions in Examples 4.6 and 4.8. For example, for the ideal assembly conditions (Cases 13, 17 and 21), Case 17 has a lower level of KEs than other ideal assembly conditions. Moreover, all the assembly conditions discussed in Example 4.7 have a larger size of contact ellipse than other assembly conditions of Examples 4.6 and 4.8, since the mating tooth surfaces of pinion and gear of Example 4.7 are convex tooth surface mating with concave tooth surface.

Example 4.9: Contact ratios of the spherical helical gear set with crossed axes meshing under three mating combinations

Some major design parameters of the hob cutter and three mating combinations of the spherical helical gear sets with crossed axes mounting mode (i.e. $\gamma_o = 30^\circ$) are summarized in Table 4.4. Moreover, three mating combinations of the spherical helical gear sets with crossed axes are all assembled under ideal condition and axial misalignments $\Delta\gamma_v=2^\circ$ and $\Delta\gamma_h=0.5^\circ$.

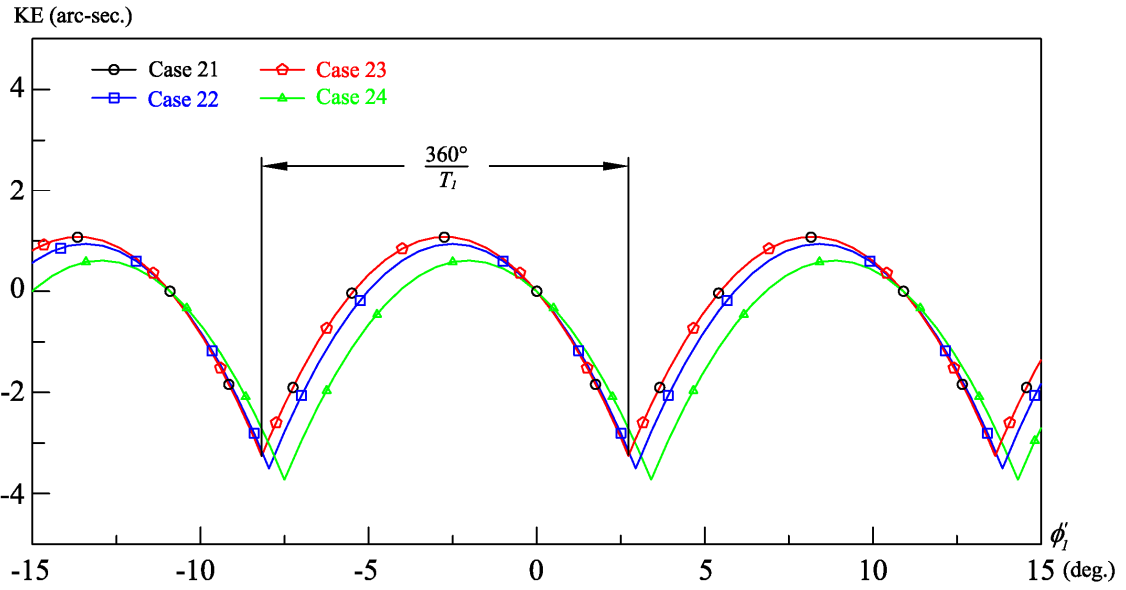
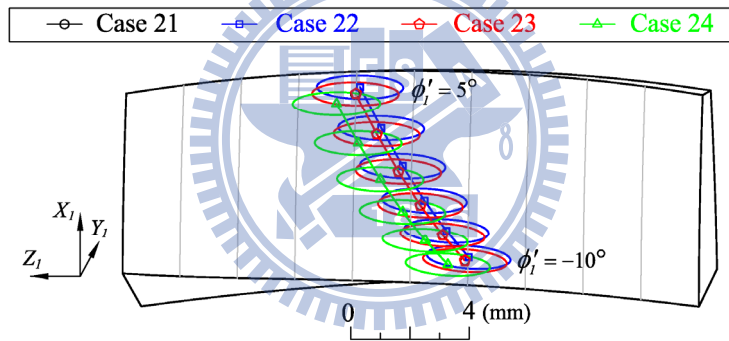
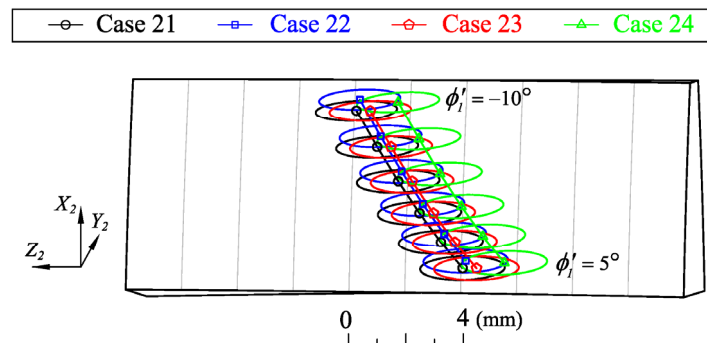


Fig. 4.17 KEs of the gear set with convex pinion and conventional helical gear under crossed axes mounting mode and different assembly conditions



(a) Convex pinion



(b) Conventional helical gear

Fig. 4.18 Contact ellipses and contact loci on tooth surfaces of the gear set under crossed axes mounting mode and different assembly conditions

Table 4.5 summarizes the contact ratios (CRs) and the rotation angles (ϕ'_{IS} and ϕ'_{IE}) of starting contact and end contact of the pinion tooth surface during the meshing of the spherical helical gear sets. The CRs of the spherical helical gear sets under three mating combinations with the ideal assembly condition and axial misalignments $\Delta\gamma_v = 2^\circ$ and $\Delta\gamma_h = 0.5^\circ$ are about 1.7. Comparing with the ideal assembly condition, the spherical helical gear set with vertical and horizontal axial misalignments ($\Delta\gamma_v = 2^\circ$ and $\Delta\gamma_h = 0.5^\circ$) has only a slightly influence on their CRs.

Example 4.10: Average ratio a/b of the major and minor axes of the contact ellipse of the spherical helical gear set with crossed axes meshing under different assembly conditions

The major design parameters of the hob cutter and three mating combinations of the spherical helical gear sets with crossed axes are chosen the same as those shown in Table 4.4. Two assembly conditions, ideal assembly condition and axial misalignments ($\Delta\gamma_v = 2^\circ$ and $\Delta\gamma_h = 0.5^\circ$), are assembled under three mating combinations for the spherical helical gear sets with crossed axes.

Table 4.6 lists the average ratio of the major and minor axes of the contact ellipse a/b for three mating combinations of spherical helical gear sets with different assembly conditions when the pinion's rotation angles are $\phi'_i = -10^\circ \sim 5^\circ$ with an increment angle, e.g. 0.1 degree. The gear set of having convex pinion mating with concave gear has a larger average ratio a/b than other two mating combinations. In the inverse situation, the convex pinion mating with convex gear has a smaller level of average ratio a/b than other two mating combinations. Comparing with the ideal assembly condition, the average ratio a/b is not sensitive to axial misalignments for the mating combinations of convex pinion with convex gear and convex pinion with

Table 4.5 Contact ratios of the spherical helical gear sets with crossed axes under different assembly conditions

Mating combinations	Ideal assembly condition	Axial misalignments
Convex pinion with Convex gear	1.72 (-12.3°~6.5°)	1.72 (-11.8°~7°)
Convex pinion with Concave gear	1.65 (-11.7°~6.3°)	1.7 (-10.9°~7.4°)
Convex pinion with Helical gear	1.72 (-12.3°~6.5°)	1.72 (-11.8°~7°)

Table 4.6 Average ratio a/b of major and minor axes of contact ellipses of spherical helical gear sets with crossed axes meshing under different assembly conditions

Mating combinations	Ideal assembly condition	Axial misalignments
Convex pinion with Convex gear	2.94	2.95
Convex pinion with Concave gear	5.33	5.02
Convex pinion with Helical gear	3.69	3.69

conventional helical gear. However, the spherical helical gear set of convex pinion mating with concave gear has a larger variation of the a/b ratio than other two mating combinations under the ideal assembly condition and the misalignments.

4.7. Remarks

According to the mathematical models of the spherical helical gears with convex and concave teeth developed in Chapter 2, the meshing model of the spherical helical gear sets with assembly errors under two axes mounting and three mating combinations are derived by using the TCA method (Eqs. (4.1) and (4.2)). Based on the developed meshing model of the gear set, the contact loci, KEs (Eq. (4.18)) and contact ratios (Eq. (4.19)) for three mating combinations of the spherical helical gear set with different assembly conditions under two axes mounting modes can be investigated. Moreover, the bearing contacts and average ratios a/b of major and

minor axes of contact ellipses for the three mating combinations of the spherical helical gear sets with different assembly conditions under two axes mounting modes are estimated by utilizing the TCA method and surface separation topology method (Eqs. (4.26)~(4.28)). According to the TCA simulation results, the following remarks can be drawn:

- (1) The KEs of spherical helical gear sets under the proposed two axes mounting modes and three mating combinations will be induced under the ideal assembly condition, the center distance error and the axial shifting error of the face width. However, the levels of KEs of the spherical helical gear sets under the proposed two axes mounting modes and three mating combinations are small. Moreover, the bearing contacts of the spherical helical gear sets under the two axes mounting modes and three mating combinations are localized in the middle region of the face width. Comparing with the ideal assembly condition, the bearing contact of the spherical helical gear set with convex pinion and concave gear under the parallel axes mounting mode and an axial shifting error of the face width has a larger shifting displacement (see Fig. 4.10) than other two mating combinations. This phenomenon is quite similar to that of the spherical helical gear set with convex pinion and concave gear under crossed axes mounting mode has the same situation (see Fig. 4.16).
- (2) The KEs of the spherical helical gear sets under the three mating combinations are not sensitive to the misalignments ($\Delta\gamma_v = 2^\circ$ and $\Delta\gamma_h = 0.5^\circ$) because the contact type of the proposed spherical helical gear set is in point contacts. Bearing contacts of the spherical helical gear set are localized near by the middle region of the face width. The spherical helical gear set with axial misalignments has a larger level of bearing contact shifting than other assembly error conditions.

However, the bearing contacts of the spherical helical gear set with a large axial misalignment are still located near by the middle region of the face width.

- (3) Regardless of the axes mounting modes (parallel or crossed axes mounting mode), the CRs of the spherical helical gear set for the three mating combinations under ideal assembly condition and the large axial misalignments ($\Delta\gamma_v = 2^\circ$ and $\Delta\gamma_h = 0.5^\circ$) are about 1.7 (see Tables 4.2 and 4.5). Comparing with the ideal assembly condition, the CRs of the spherical helical gear sets under the two axes mounting modes and three mating combinations are not sensitive to the axial misalignments (see Tables 4.2 and 4.5).
- (4) Regardless of the assembly combinations and the axes mounting modes, the spherical helical gear set with convex pinion and concave gear has a larger average ratio of the major and minor axes, a/b , of the contact ellipses than other two mating combinations. The spherical helical gear sets with convex pinion and convex gear under two axes mounting modes have smaller a/b ratios (see Tables 4.3 and 4.6). Moreover, the average ratios a/b are not sensitive to the assembly condition of axial misalignments ($\Delta\gamma_v = 2^\circ$ and $\Delta\gamma_h = 0.5^\circ$) for the spherical helical gear set under parallel and crossed axes mounting modes (see Tables 4.3 and 4.6).
- (5) If the axial misalignments of the spherical helical gear set under parallel and crossed axes mounting modes are modified as $\Delta\gamma_v = -2^\circ$ and $\Delta\gamma_h = -0.5^\circ$, the KE's amplitude, contact ratio and average a/b ratio of the gear set will have no apparent change, while the KE's phase of the gear set will change from phase lead (or lag) to phase lag (or lead).

CHAPTER 5

Finite Element Stress Analysis

5.1 Introduction

Due to the progress of computer technology and the computational techniques, finite element method (FEM) [46] becomes a popular tool to determine the formation of bearing contact and stress distribution of a gear drive, especially with a complex tooth geometry. For the conventional and standard gears, the contact and bending stresses can be calculated by employing the stress formulae given in the handbook [47]. However, the stress of gears with a special and complex tooth profile can't be accurately predicted by using the stress formula of the conventional and standard gears. Therefore, FEM is adopted to perform the stress analysis of the proposed spherical helical gear set for complex contact situations.

In this chapter, an automatic mesh-generation program for the contact models of the spherical helical gear set with three types of mating combinations, convex with convex teeth, convex with concave teeth and convex with helical teeth, under two axes mounting modes (parallel axes and crossing axes) was performed by employing the C++ program language. The design parameters and boundary conditions are also imposed on the contact model of the spherical helical gear sets. Furthermore, several illustrative numerical examples are presented to demonstrate the finite element (FE) stress analyses of the spherical helical gear sets with three types of mating combinations under two axes mounting modes by utilizing the commercial finite element analysis (FEA) package, ABAQUS/Standard [48]. Besides, all analyzed FE contact models of the spherical helical gear sets are adopted after meshes convergence test. Therefore, the results of the FEA in this chapter and the results of contact ellipse simulations in previous chapter (Chapter 4) can prove mutually, and can also verify

the superiority of the proposed spherical helical gear sets.

5.2 Finite element contact models of spherical helical gear sets

5.2.1 Processes of establishing FE contact model

The automatic mesh-generation program is developed by utilizing the C++ program language. The processes of establishing the FE contact model of a spherical helical gear set are summarized as follows:

- (1) Determine the surface coordinates, including the tooth profiles and fillets of the spherical helical pinion and gear in meshing, by utilizing the developed mathematical model (Chapter 2) and TCA meshing model (Chapter 4) of the mating spherical helical pinion and gear. A 3-D tooth solid model of the spherical helical gear can be illustrated as shown in Fig. 5.1(a).
- (2) As shown in Fig. 5.1(b), set up some auxiliary points (red points of Fig. 5.1(b)) to partition the 3-D tooth solid model of the spherical helical gear into six parts for easy to generate the hexahedron solid element.
- (3) Calculate and generate the nodes on the tooth surfaces and in the tooth body of the spherical helical pinion and gear, and assign those nodes in a sequential number, as shown in Fig. 5.1(c).
- (4) As shown in Fig. 5.1(d), establish the hexahedron solid elements that include a serial regular nodal numbers by referring the ordering rule of hexahedron solid elements [48], and assign those elements in a sequential number, too.
- (5) Set up the material properties, loadings, boundary conditions and interactions between two surfaces in meshing to the mating spherical helical pinion and gear.

The hexahedron solid element type, C3D8I, has been chosen to improve the bending behavior [48]. The steel material, AISI 1045, is chosen for all FE contact models of the investigated spherical helical gear sets. The basic material properties are

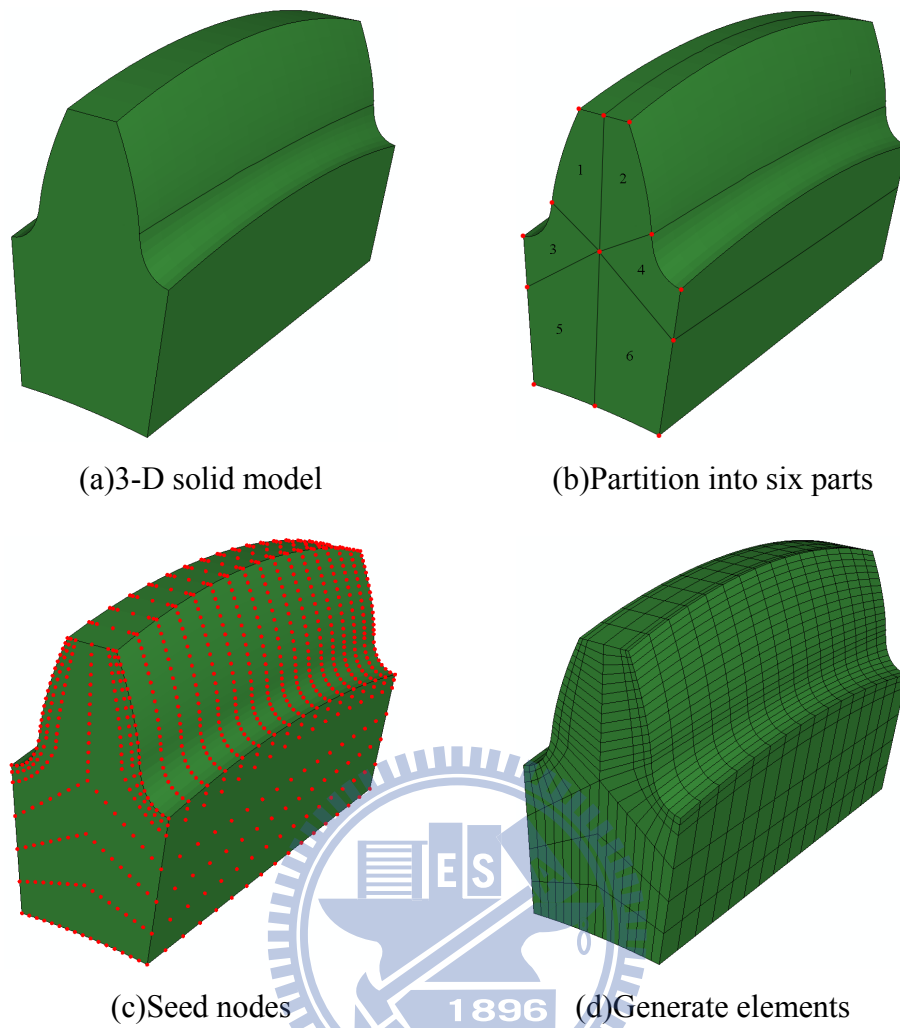


Fig. 5.1 Processes of establishing the FE contact model of a spherical helical gear

Young's modulus $E=2.05 \times 10^5$ MPa, Poisson's ratio $\nu=0.29$ and density $\rho=7.85 \times 10^{-6}$ Kg/mm³. Besides, the material is considered as isotropic, and the heat generation and thermal stress are ignored. However, the actual contact situation of a gear set is complex since the friction on the interface of contact surfaces is hard to know. Therefore, the lubrication condition on the interface of contact surfaces of the spherical helical gear set is assumed as good lubrication that means the frictionless condition is applied to the interface of the contact surfaces. In the software ABAQUS/Standard, the contact pair must be defined as a master surface and a slave surface [48] before the contact stress analysis. According to the rule of the software ABAQUS/Standard, the master and slave surfaces are identified as the large and small

curvature surfaces, respectively. Therefore, all pinion's and gear's tooth surfaces of the proposed spherical helical gear sets are defined as the master and slave surfaces, respectively.

By using the developed automatic mesh-generation program and the gear's design parameters of Table 5.1, a FE contact model of whole spherical helical gear set with convex pinion and concave gear under parallel axes mounting mode can be established as shown Fig. 5.2. Consequently, another FE contact model of whole spherical helical gear set with convex pinion and concave gear under crossed axes mounting mode can also be established by utilizing the same developed automatic mesh-generation program and the gear's design parameters of Table 5.1 as shown in Fig. 5.3.

5.2.2 Simplified meshing model of a gear set

However, the FE contact models shown in Figs. 5.2 and 5.3 are not good models for stress analyses of the gear sets because of those coarse meshes. According to the

Table 5.1 Major design parameters of spherical helical gear set with convex pinion and concave gear under parallel and crossed axes mounting modes

Types of gear	Hob	Parallel axes		Crossed axes	
		Convex pinion	Concave gear	Convex pinion	Concave gear
Normal module m_n (mm/tooth)	4	4	4	4	4
Number of teeth T_j	1	33	47	33	47
Normal pressure angle α_n (deg.)	20	20	20	20	20
Lead angle λ_g (deg.)	3.823 RH	75 RH	75 LH	75 RH	75 RH
Face width W (mm)	-	20	20	20	20
Pitch radius r_j (mm)	30	68.328	97.316	68.328	97.316
Spherical radius R_s (mm)	-	68.328	97.316	68.328	97.316
Cutting radius R_c (mm)	-	98.328	127.316	98.328	127.316
Center distance C (mm)	-	-	165.644	-	165.644

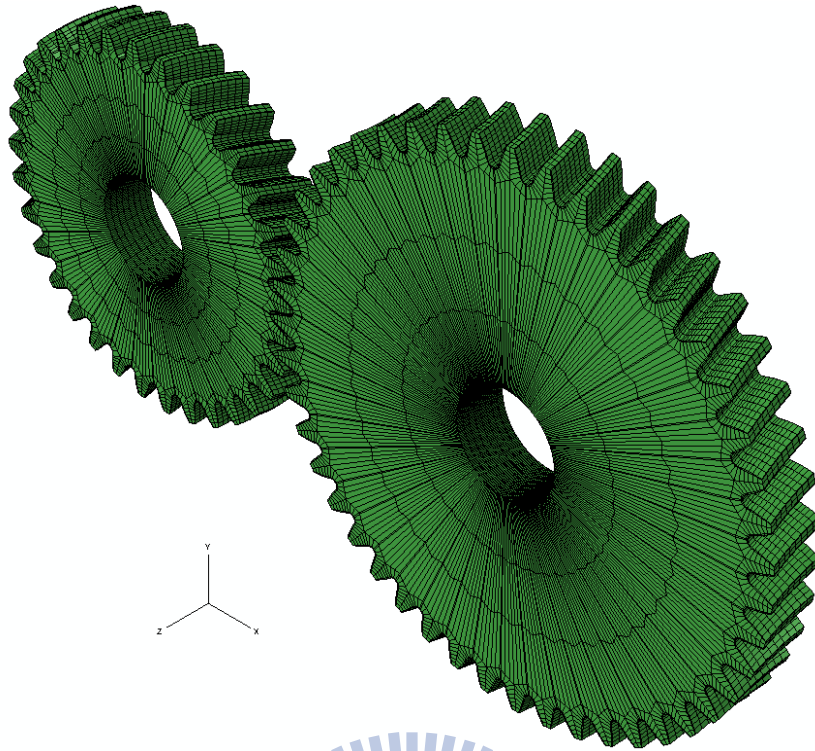


Fig. 5.2 Finite element contact model of a spherical helical gear set with convex pinion and concave gear under parallel axes mounting mode

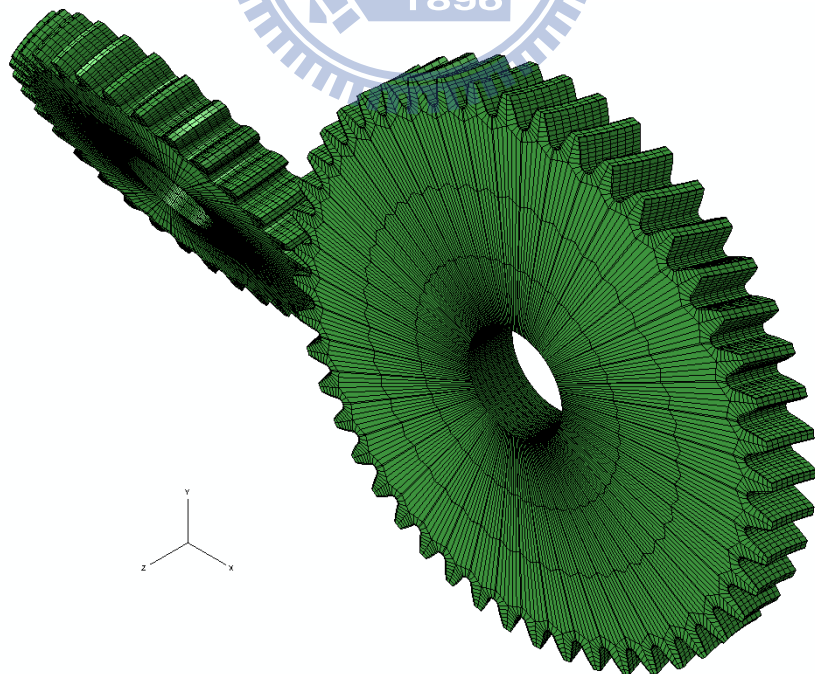


Fig. 5.3 Finite element contact model of a spherical helical gear set with convex pinion and concave gear under crossed axes mounting mode

investigated results of TCA, the contact ratios of the proposed spherical helical gear sets under parallel and crossed axes mounting mode are about 1.7 (see Examples 4.4 and 4.9). It means that at most of contact instants the maximum numbers of teeth in contact is 2. Therefore, a simplified contact model for a gear set with four teeth can be considered as shown in Fig. 5.4. The middle two teeth of the simplified gear set with four teeth are defined as the teeth in contact, whereas, other two teeth are set as the teeth in non-contact. Moreover, the bottom surface and both-side surfaces of the simplified pinion are considered as rigid surfaces to simulate the constraint effect of rotation shaft and the effect that acted by other teeth [43], respectively. A roller boundary condition is applied on both-side surfaces and bottom surface of the simplified gear. The roller boundary condition on both-side surfaces of gear has a free degree-of-freedom (DOF) along the radius direction of gear, while the other DOFs are fixed. The roller boundary condition on bottom surface of gear has a free DOF along the tangent direction of that surface, while the other DOFs are also fixed. Besides, symbols $r_{shaft,j}$ ($j=1$ and 2) denote the shaft-hole radii of pinion and gear, respectively. Symbol O_1 indicates the reference node for the rigid surfaces of pinion, while symbol

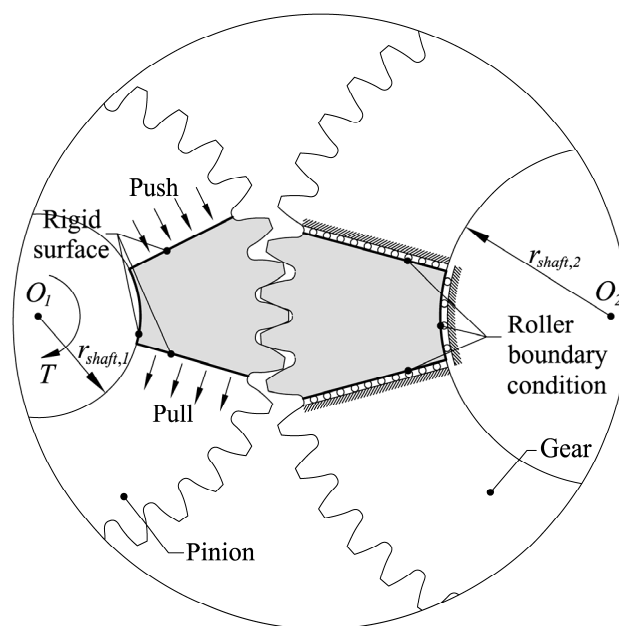


Fig. 5.4 Simplified contact model of a gear set with boundary conditions

O_2 denotes the center point of gear. For all FE contact models of the spherical gear sets appear in this study, a torque, $T=200$ N-m, is applied to the pinion's rotation axis.

5.2.3 Meshes convergence test and local refined FE model

In general, a more refined mesh model may obtain a more accurate simulation result but it takes much more time in analysis. Therefore, it is important to adopt a properly refined mesh to ensure the simulation result is acceptable. In this study, the sufficiently refined meshes of the spherical helical gear set have been performed by applying the meshes convergence test [46] and employing the developed automatic mesh-generation program. Major design parameters of the spherical helical gear set with convex pinion and concave gear under parallel axes mounting mode for the meshes convergence test are given in Table 5.1. Table 5.2 gives five different mesh densities for the spherical helical convex pinion and concave gear, while Fig. 5.5 reveals different cases of mesh densities for the convex spherical helical pinion. If the spherical helical gear set is subjected to a torque 200N-m, Fig. 5.6 shows the nodal displacements and bending stresses of those cases (Cases 1~5) for the convex pinion (Fig. 5.6(a)) at position coordinates of $X_1=65.195$ mm, $Y_1=-3.961$ mm and $Z_1=0$ mm, and for the concave gear (Fig. 5.6(b)) at position coordinates of $X_2=72.396$ mm, $Y_2=10.487$ mm and $Z_2=0$ mm. It is found that the nodal displacements are converged to a stable level (variation is less than 2%) in the cases of refined (Case 3) and high refined meshes (Case 4). However, the FE analysis for the high refined case (Case 4) is time consumptive. Therefore, the local refined mesh case (Case 5) can be adopted for the FE analysis [44]. The information and analysis results of the local refined case (Case 5) are also shown in Table 5.2 and Fig. 5.6, respectively. According to Fig. 5.6, the local refined mesh case (Case 5) is also convergent and similar to that of the high refined mesh case (Case 4), but the numbers of elements and nodes of the local

refined case are substantially less than those of the high refined case (reduction about 30%). Therefore, the local refined mesh model (Cases 5) is adopted thereafter in this study for stress analysis of the spherical helical gear sets under parallel and crossed axes mounting modes. The local refined mesh zone of the spherical helical gear set is controlled with 42 elements along the face width direction. Figures 5.7 and 5.8 illustrate the spherical helical gear sets with local refined mesh models under parallel

Table 5.2 Mesh densities of the spherical convex pinion and concave gear

Cases	Mesh densities	Convex pinion		Concave gear	
		Total nodes	Total elements	Total nodes	Total elements
1	Coarse	14,076	11,198	12,788	10,142
2	Normal	26,004	21,152	23,232	18,848
3	Refined	40,248	33,138	36,636	30,114
4	High refined	66,528	55,366	61,236	50,902
5	Local refined	45,408	37,506	41,796	34,482

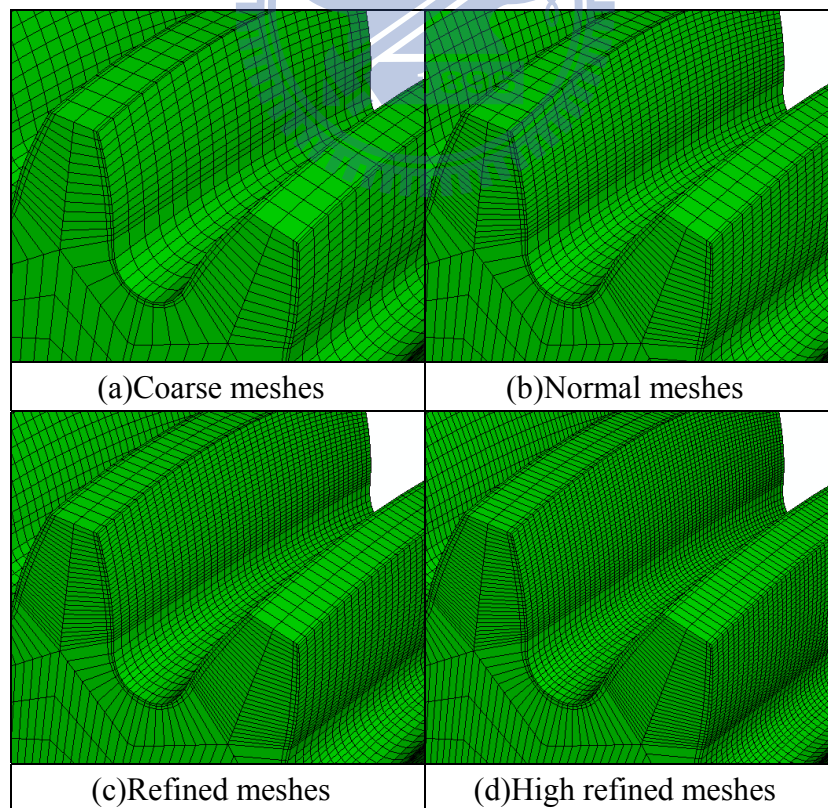
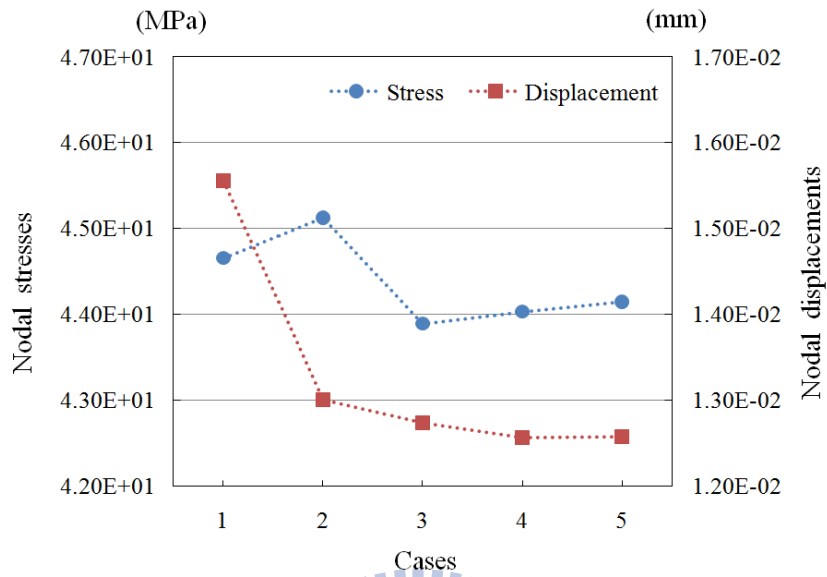
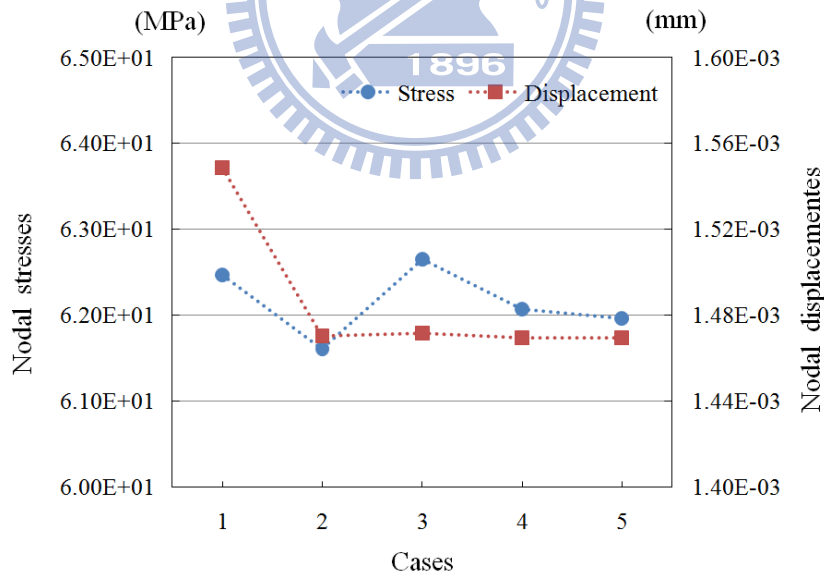


Fig. 5.5 Finite element model of the convex spherical helical pinion with different mesh densities



(a) Convex pinion



(b) Convex gear

Fig. 5.6 Convergence test of nodal displacements and bending stresses for the mating of spherical convex pinion and concave gear with four teeth subjected to a torque of 200N-m

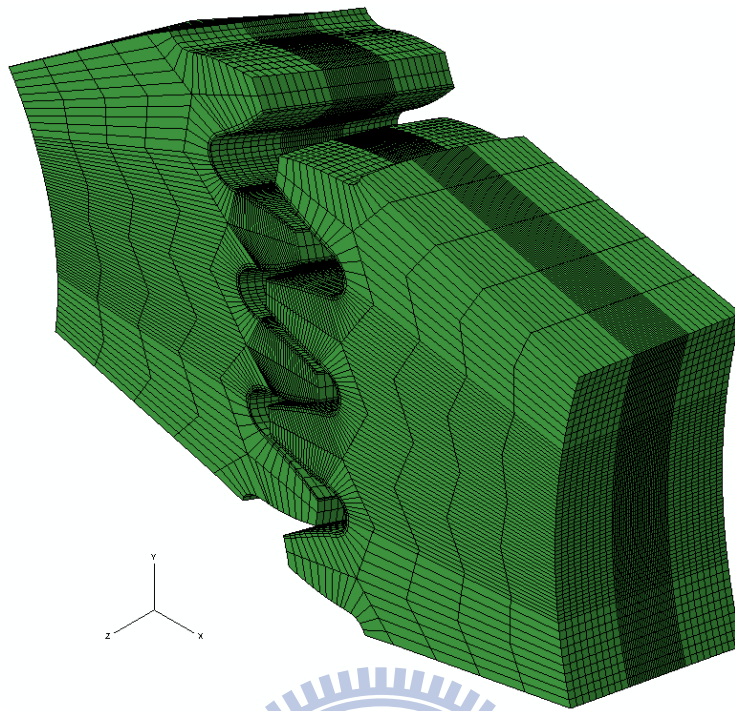


Fig. 5.7 Finite element contact model of the spherical helical gear set with local refined meshes under parallel axes mounting mode

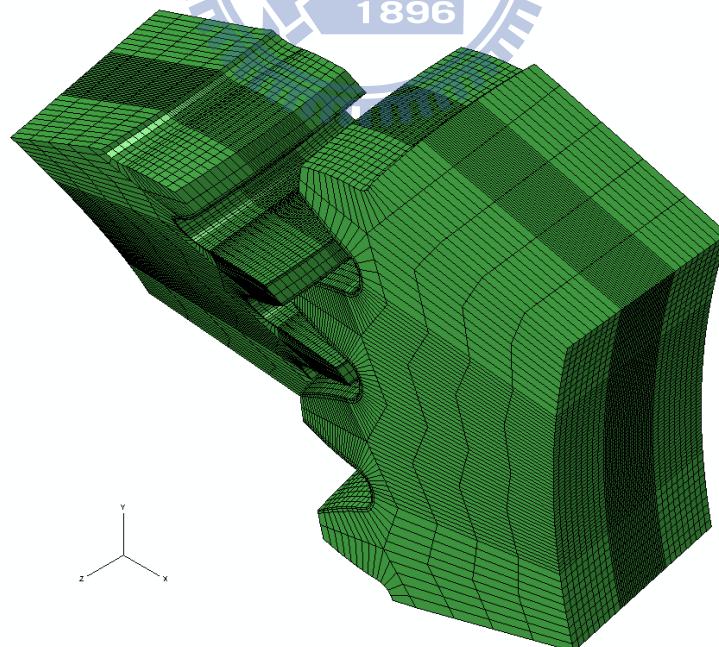


Fig. 5.8 Finite element contact model of the spherical helical gear set with local refined meshes under crossed axes mounting mode

and crossed axes mounting modes, respectively. Moreover, the local refined mesh method is also applied in the elements along the tooth thickness directions of the pinion and gear (see Appendix A). The refined elements along the tooth thickness directions of the pinion and gear are concentrated near the tooth surface.

5.3 Numerical examples

Based on the developed mathematical model and the automatic mesh-generation program of the proposed spherical helical gear sets, the stress analysis of the gear sets can be investigated by using the commercial FEM package, ABAQUS/Standard. In this section, six numerical examples are demonstrated for analyses on the contact and bending stresses of the spherical helical gear sets under different axes mounting modes, mating combinations and assembly conditions. Again, the FE models of Figs. 5.7 and 5.8 with local refined meshes for the spherical helical gear sets under two axes mounting modes are adopted for following numerical examples, respectively. Moreover, some major design parameters of the spherical helical gear sets for all following numerical examples are given in Table 5.3.

Table 5.3 Major design parameters of the spherical helical gear sets under parallel axes mounting mode

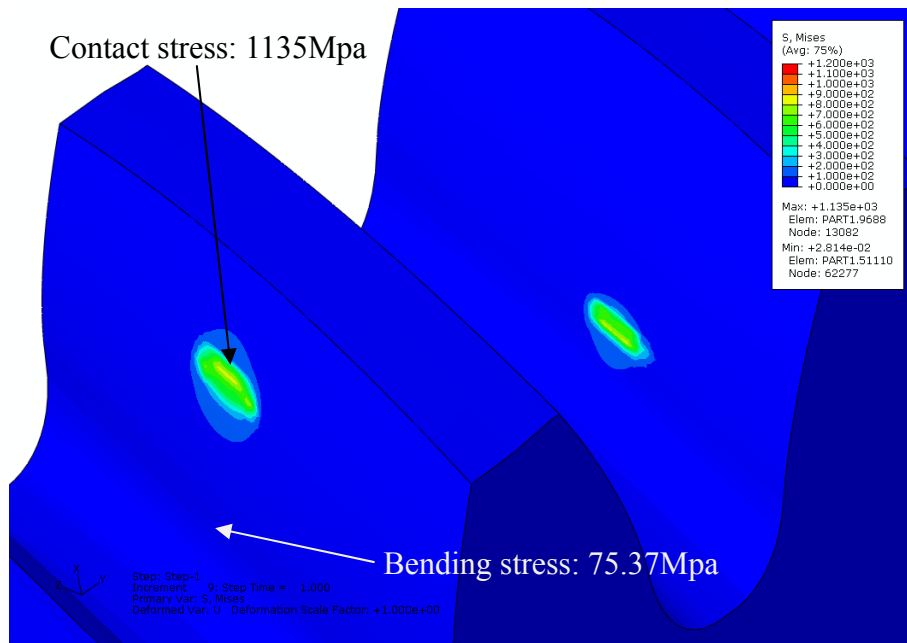
Types of gear	Hob	Gear			
		Pinion Convex	Convex	Concave	Helical
Normal module M_n (mm/tooth)	4	4	4	4	4
Number of teeth T_j	1	33	47	47	47
Normal pressure angle α_n (deg.)	20	20	20	20	20
Lead angle λ_g (deg.)	3.823 RH	75 RH	75 LH	75 LH	75 LH
Face width W (mm)	-	20	20	20	20
Pitch radius r_j (mm)	30	68.328	97.316	97.316	97.316
Spherical radius R_s (mm)	-	68.328	97.316	97.316	-
Cutting radius R_c (mm)	-	98.328	127.316	67.316	-
Center distance C (mm)	-	-	165.644	165.644	165.644

Example 5.1 Stress distributions of spherical helical gear sets with three types of mating combinations under parallel axes mounting mode and ideal assembly condition

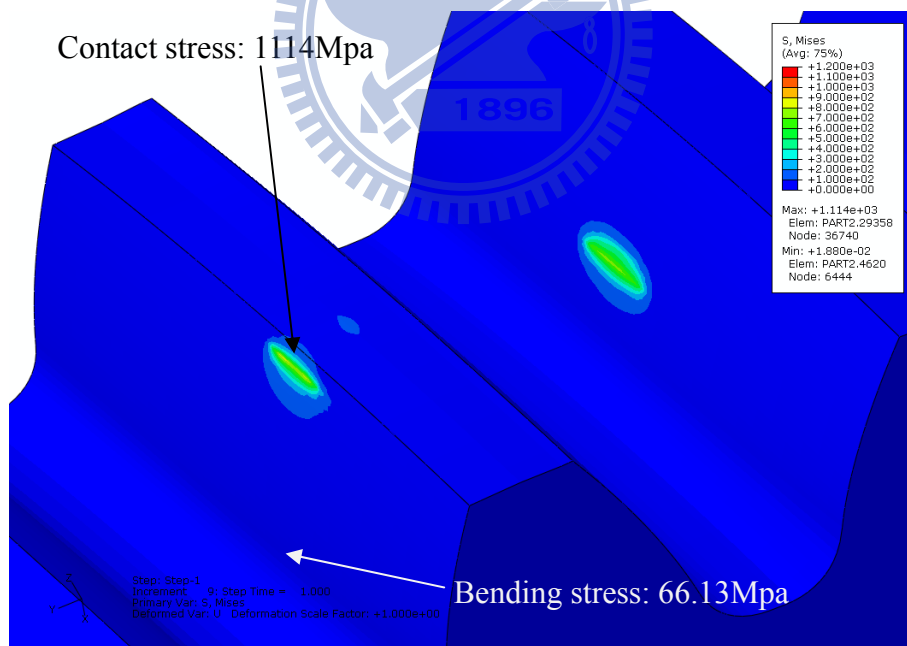
The contact and bending von-Mises stresses on tooth surfaces of spherical helical gear sets with three types of mating combinations under parallel axes mounting mode are performed and summarized in Table 5.4. Moreover, the spherical helical gear sets are meshing at pinion's beginning rotation angle (i.e. $\phi'_i = 0^\circ$). Figures 5.9, 5.10 and 5.11 reveals the von-Mises stress distributions on tooth surfaces of the spherical helical gear sets with convex pinion (Fig. 5.9(a)) and convex gear (Fig. 5.9(b)), convex pinion (Fig. 5.10(a)) and concave gear (Fig. 5.10(b)), and convex pinion (Fig. 5.11(a)) and conventional helical gear (Fig. 5.11(b)), respectively. It is found that contact regions of the spherical helical gear sets are located near by the middle region of the tooth face width under the ideal assembly condition. Moreover, the convex pinion mating with concave gear has the largest size of contact region (Fig. 5.10), while the convex pinion mating with convex gear has the smallest size of contact region (Fig. 5.9). This verified that the convex pinion mating with concave gear has the smallest von-Mises stress because it has the largest contact region, whereas, the inverse situation exists for the convex pinion mating with convex gear. It is worth

Table 5.4 Contact and bending von-Mises stresses of the spherical helical gear set with three types of mating combinations under parallel axes mounting mode at the pinion's beginning rotation angle

Mating types	Convex pinion vs. convex gear		Convex pinion vs. concave gear		Convex pinion vs. helical gear	
	Pinion	Gear	Pinion	Gear	Pinion	Gear
	Contact stress (MPa)	1135	1114	912.4	812.3	978.4
Bending stress (MPa)	75.37	66.13	62.26	83.56	76.36	65.16

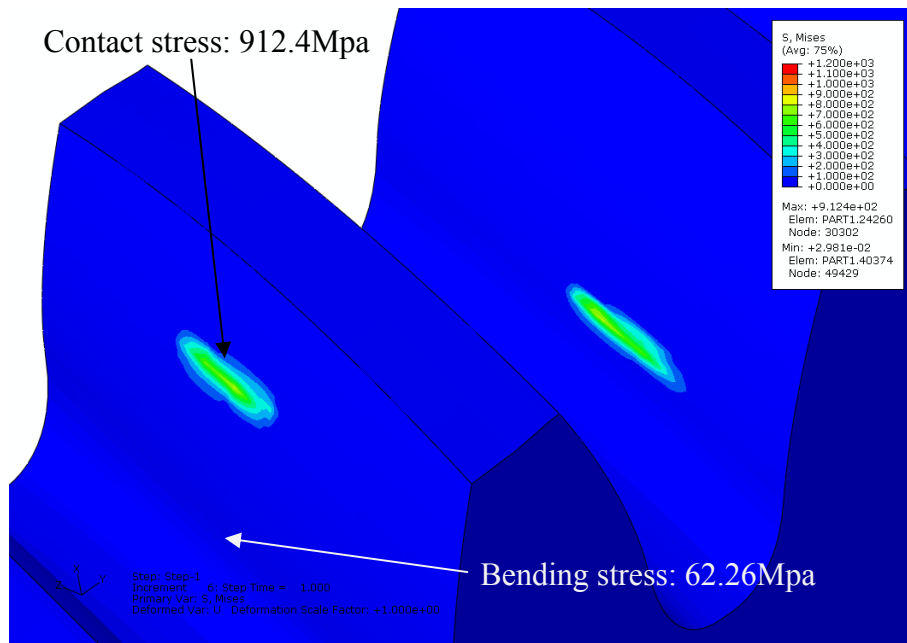


(a) Convex pinion

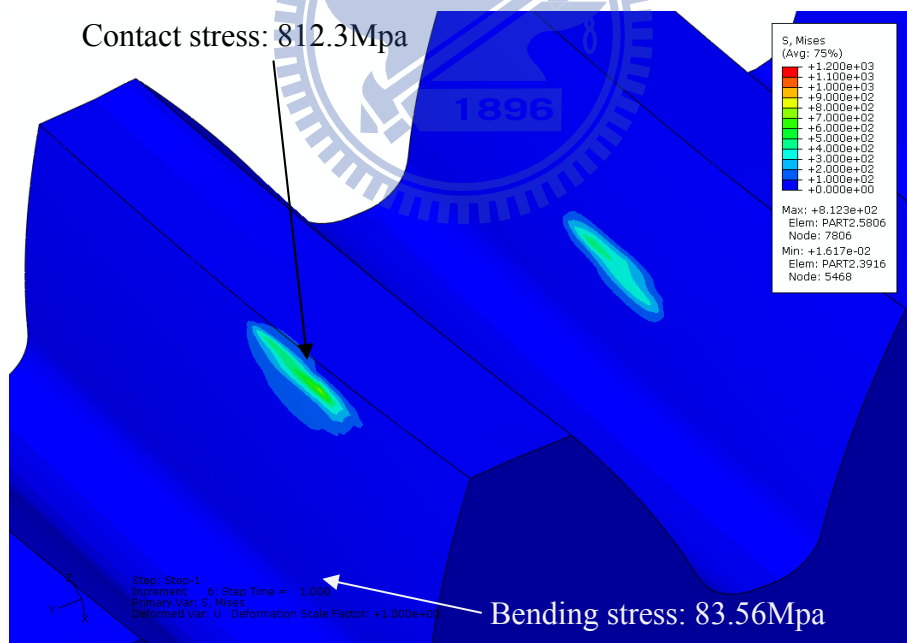


(b) Convex gear

Fig. 5.9 von-Mises stress distributions on tooth surfaces of the spherical helical gear set with convex pinion and convex gear under the parallel axes mounting mode and ideal assembly condition

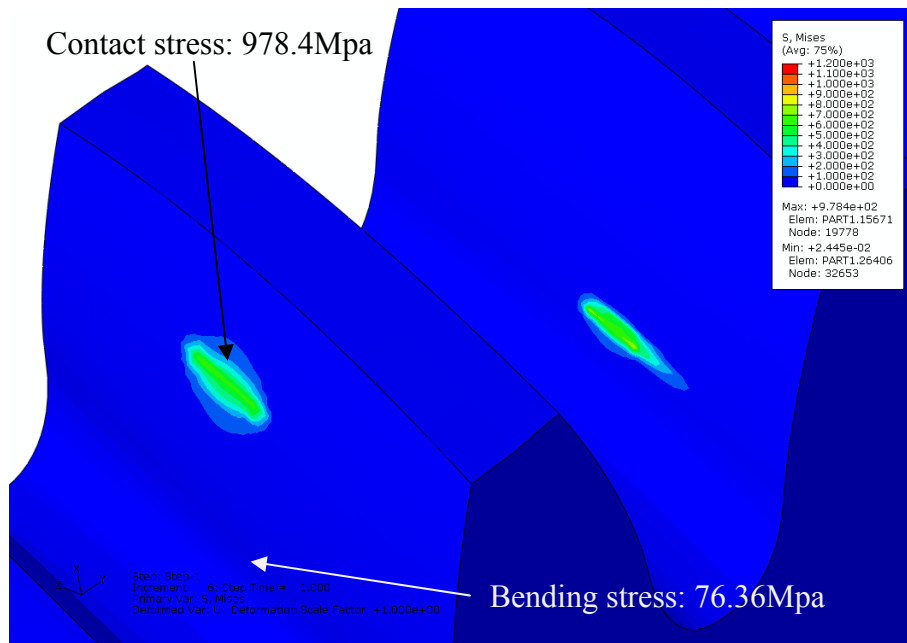


(a) Convex pinion

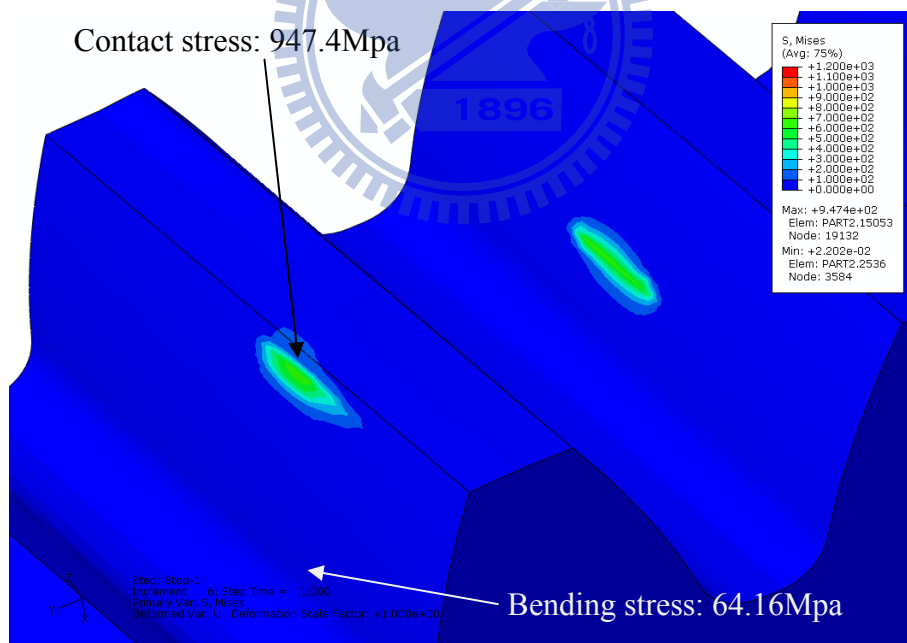


(b) Concave gear

Fig. 5.10 von-Mises stress distributions on tooth surfaces of the spherical helical gear set with convex pinion and concave gear under the parallel axes mounting mode and ideal assembly condition



(a) Convex pinion



(b) Conventional helical gear

Fig. 5.11 von-Mises stress distributions on tooth surfaces of the spherical helical gear set with convex pinion and conventional helical gear under the parallel axes mounting mode and ideal assembly condition

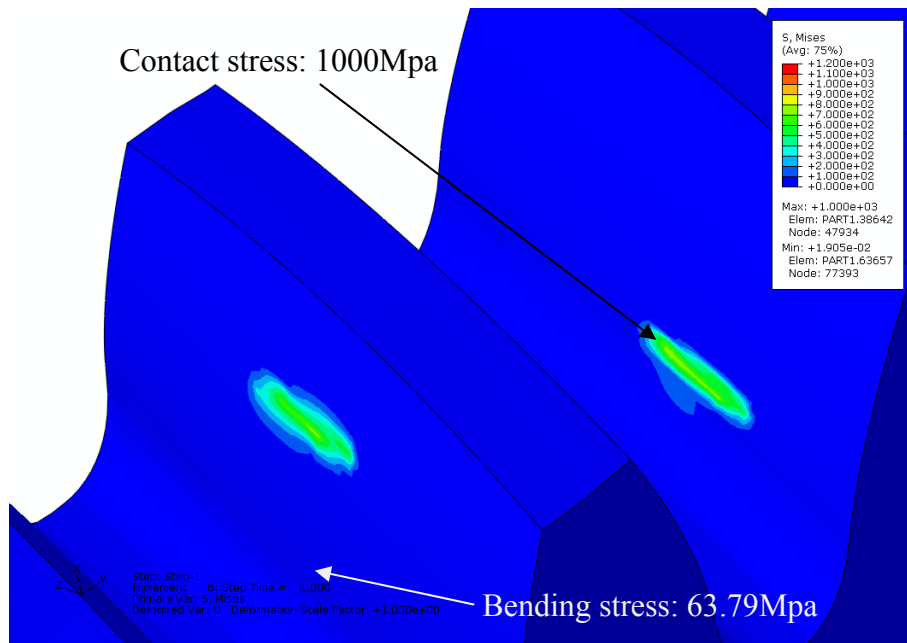
mentioned that contact regions analyzed by the FEM are similar to those of using the surface topology method [37] (see Figs. 4.10, 4.11 and 4.12).

Example 5.2 Stress distribution of the spherical helical gear set with convex pinion and concave gear under parallel axes mounting mode and axial misalignments

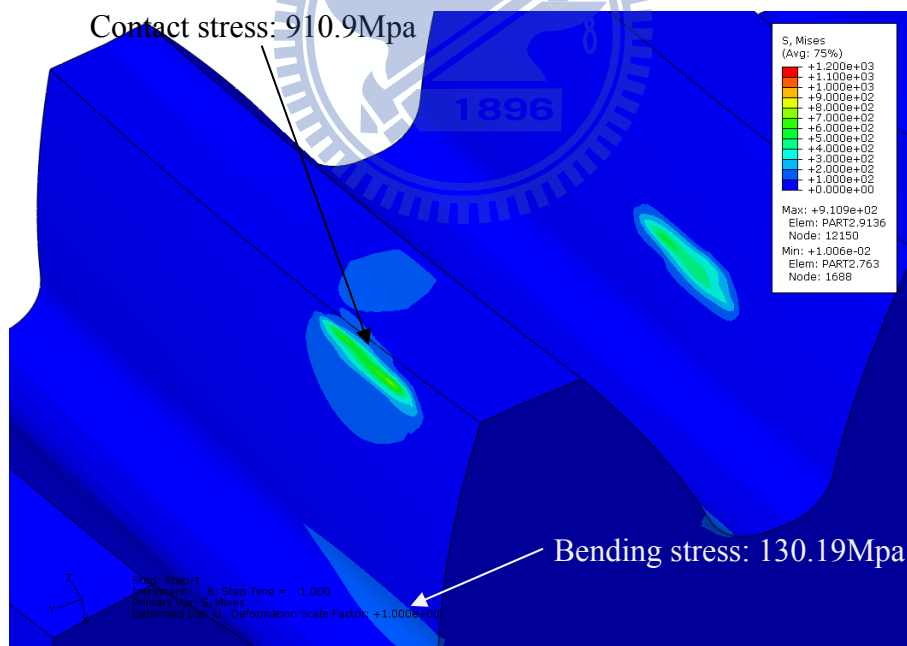
Figure 5.12 illustrates the von-Mises stress distributions of the spherical helical gear set under parallel axes mounting mode and axial assembly misalignments $\Delta\gamma_v = 2.0^\circ$ and $\Delta\gamma_h = 0.5^\circ$ at the pinion's beginning rotation angle (i.e. $\phi'_l = 0^\circ$). Moreover, the spherical helical gear set is composed of a convex pinion and a concave gear. Compared with Fig. 5.10, the contact regions of the spherical helical gear set are shifted a distance from the middle section of face width due to axial misalignments of $\Delta\gamma_v = 2.0^\circ$ and $\Delta\gamma_h = 0.5^\circ$. However, there is still no edge contact occurred for the spherical helical gear set even under axial assembly misalignments. The contact stresses of the convex pinion and concave gear at the pinion's beginning rotation angle are 1000.5MPa and 910.9MPa, respectively, whereas the bending stresses are 63.79MPa and 130.19MPa, respectively.

Example 5.3 Stress analysis of the spherical helical convex pinion mating with concave gear with large modified spherical radii R_j ($j=1$ and 2) under parallel axes mounting mode

In this example, a large modified spherical radius R_j ($j=1$ and 2 ; refer to Figs. 2.4 and 2.6) has been applied to the spherical helical gear set under parallel axes mounting mode. The convex pinion with a modified spherical radius of $R_1=1000\text{mm}$ is given to mesh with the concave gear with a modified spherical radius of $R_2=1200\text{mm}$. Moreover, the design parameters of the spherical helical gear set are also given in Table 5.3, while the gear set is assembled under the ideal condition.



(a) Convex pinion



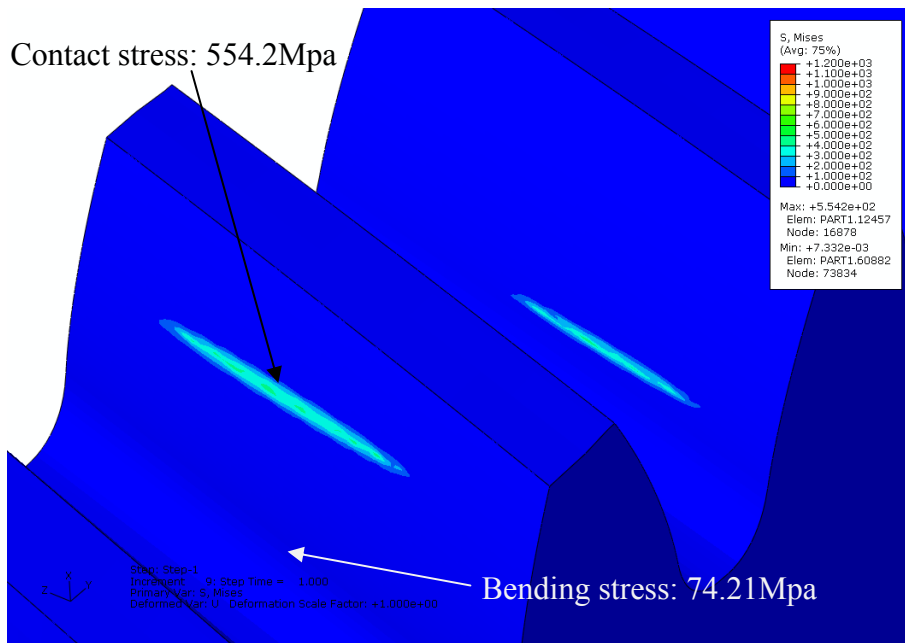
(b) Concave gear

Fig. 5.12 von-Mises stress distributions on tooth surfaces of the spherical helical gear set with convex pinion and concave gear under the parallel axes mounting mode and axial misalignments

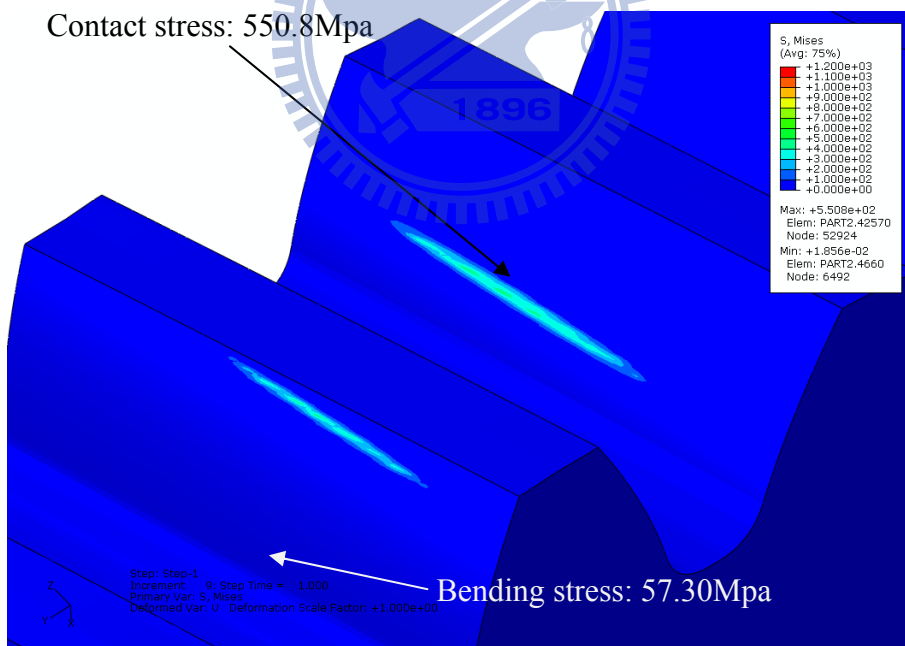
The tooth shapes of spherical helical pinion and gear with large modified spherical radii are quite similar to those of helical gears, and thus they result in slender contact regions along the longitudinal direction of face width as shown in Fig. 5.13. The contact stresses of convex pinion and concave gear at the pinion's beginning rotation angle are 554.2MPa and 550.8MPa, respectively, whereas the bending stresses are 74.21MPa and 57.30MPa, respectively. Therefore, the contact stresses of spherical helical gear set at the pinion's beginning rotation angle are substantially decreased compared with those of Example 5.1.

Example 5.4 Stress distributions of spherical helical gear sets with three types of mating combinations under crossed axes mounting mode and ideal assembly condition

Some major design parameters of the spherical helical gear sets under crossed axes mounting mode are given in Table 5.5. The contact and bending von-Mises stresses on tooth surfaces of spherical helical gear sets with three types of mating combinations under crossed axes mounting mode are performed and summarized in Table 5.6. Figures 5.14, 5.15 and 5.16 reveals the von-Mises stress distributions on tooth surfaces of the spherical helical gear sets with convex pinion (Fig. 5.14(a)) and convex gear (Fig. 5.14(b)), convex pinion (Fig. 5.15(a)) and concave gear (Fig. 5.15(b)), and convex pinion (Fig. 5.16(a)) and conventional helical gear (Fig. 5.16(b)). The spherical helical gear set with convex pinion and concave gear under crossed axes mounting mode also has the smallest von-Mises stress because it has the largest contact region, whereas, the inverse situation exists for the convex pinion mating with convex gear. It is worth mentioned that contact regions analyzed by the FEM are similar to those of using the surface topology method (see Figs. 4.14, 4.16 and 4.18). Again, the spherical helical gear sets with ideal assembly condition under crossed



(a) Convex pinion



(b) Concave gear

Fig. 5.13 von-Mises stress distributions on tooth surfaces of the spherical helical gear set with large modified spherical radii under the parallel axes mounting mode and ideal assembly condition

Table 5.5 Major design parameters of the spherical helical gear sets under crossed axes mounting mode

Types of gear	Hob	Pinion Gear			
		Convex	Convex	Concave	Helical
Normal module M_n (mm/tooth)	4	4	4	4	4
Number of teeth T_j	1	33	47	47	47
Normal pressure angle α_n (deg.)	20	20	20	20	20
Lead angle λ_g (deg.)	3.823 RH	75 RH	75 RH	75 RH	75 RH
Face width W (mm)	-	20	20	20	20
Pitch radius r_j (mm)	30	68.328	97.316	97.316	97.316
Spherical radius R_s (mm)	-	68.328	97.316	97.316	-
Cutting radius R_c (mm)	-	98.328	127.316	67.316	-
Center distance C (mm)	-	-	165.644	165.644	165.644

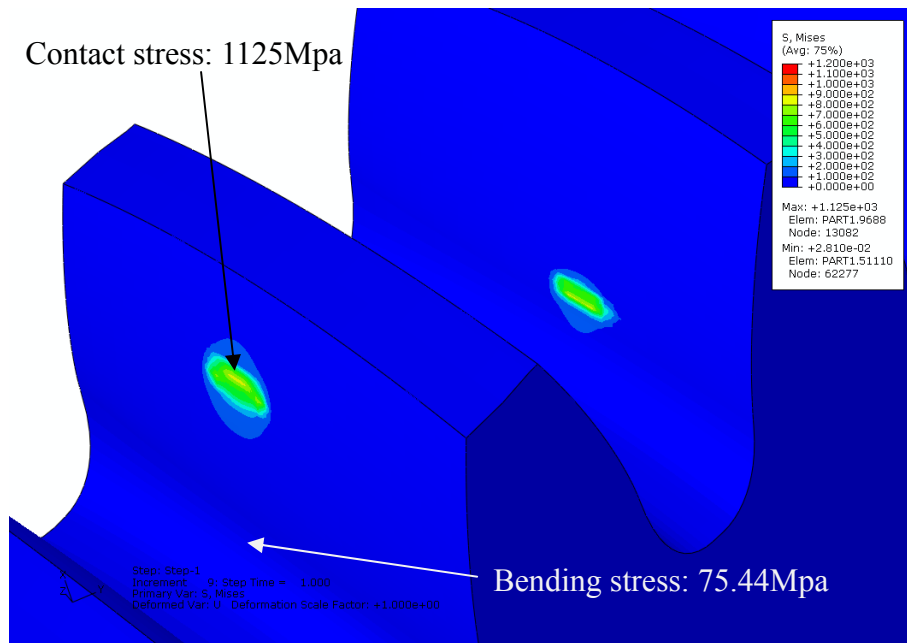
Table 5.6 Contact and bending von-Mises stresses of the spherical helical gear set with three types of mating combinations under crossed axes mounting mode at the pinion's beginning rotation angle

Mating types	Convex pinion vs. convex gear		Convex pinion vs. concave gear		Convex pinion vs. helical gear	
	Pinion	Gear	Pinion	Gear	Pinion	Gear
Contact stress (MPa)	1125	1102	884.5	795.2	1020	854.7
Bending stress (MPa)	75.44	65.84	63.06	81.33	76.55	62.65

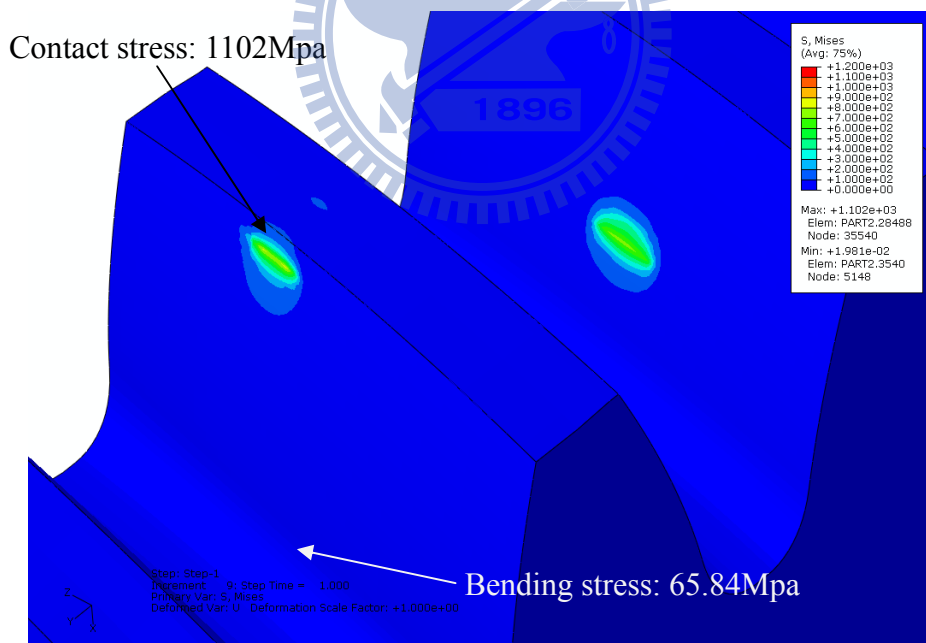
axes mounting mode are meshing at the pinion's beginning rotation angle (i.e. $\phi'_l = 0^\circ$).

Example 5.5 Stress distribution of the spherical helical gear set with convex pinion and concave gear under crossed axes mounting mode and axial misalignments

Figure 5.17 illustrates the von-Mises stress distributions of the spherical helical gear set with convex pinion and concave gear under crossed axes mounting mode and axial assembly misalignments $\Delta\gamma_v = 2.0^\circ$ and $\Delta\gamma_h = 0.5^\circ$ at the pinion's beginning rotation angle (i.e. $\phi'_l = 0^\circ$). Compared with Fig. 5.15, the contact regions of the spherical helical gear set are shifted a small distance due to the axial assembly

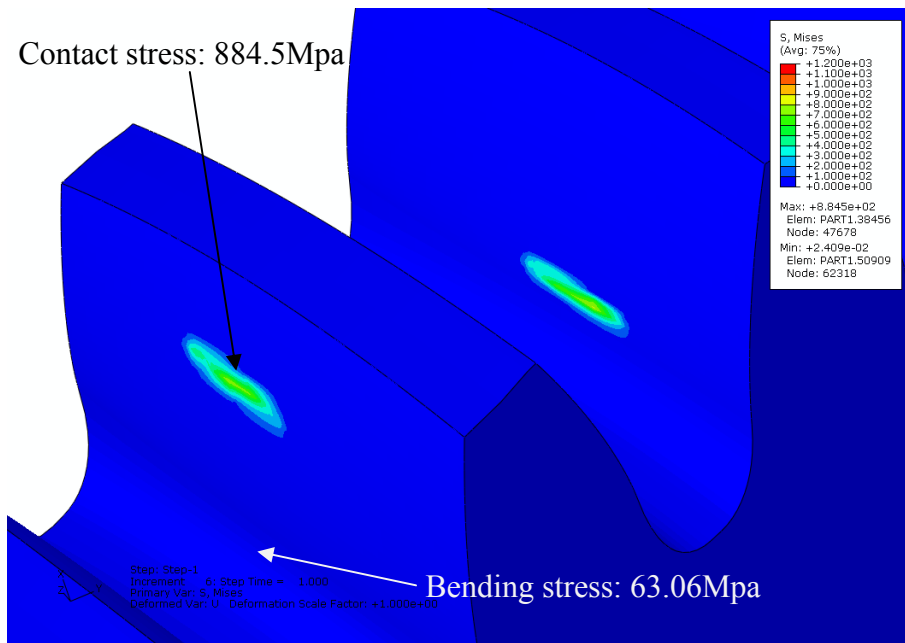


(a) Convex pinion

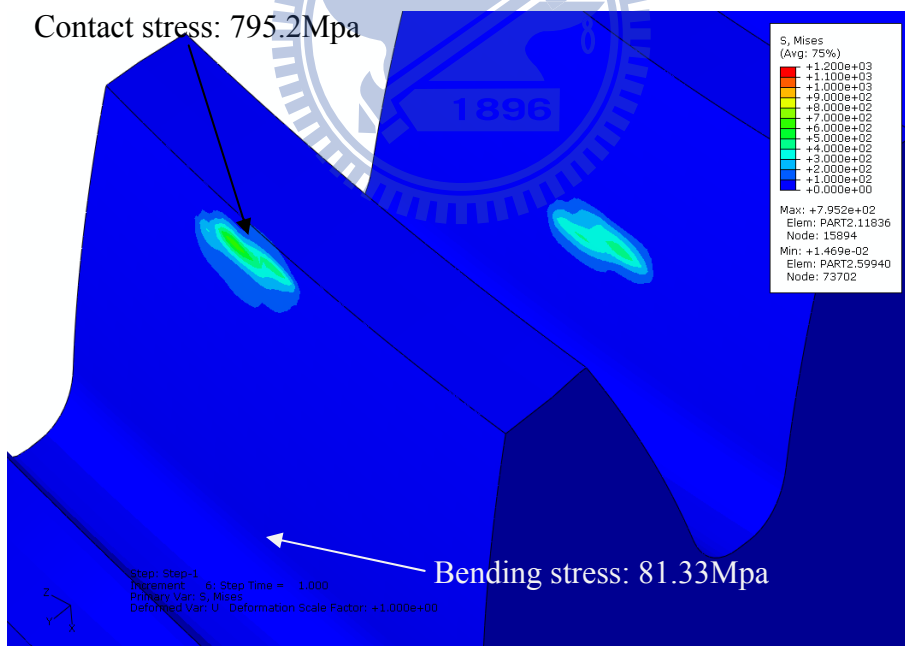


(b) Convex gear

Fig. 5.14 von-Mises stress distributions on tooth surfaces of the spherical helical gear set with convex pinion and convex gear under crossed axes mounting mode and ideal assembly condition

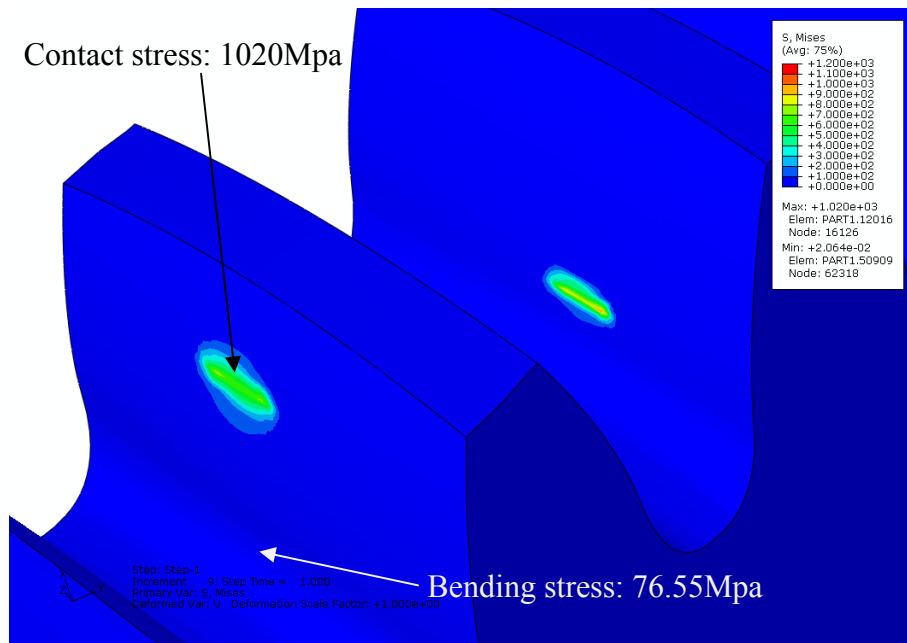


(a) Convex pinion

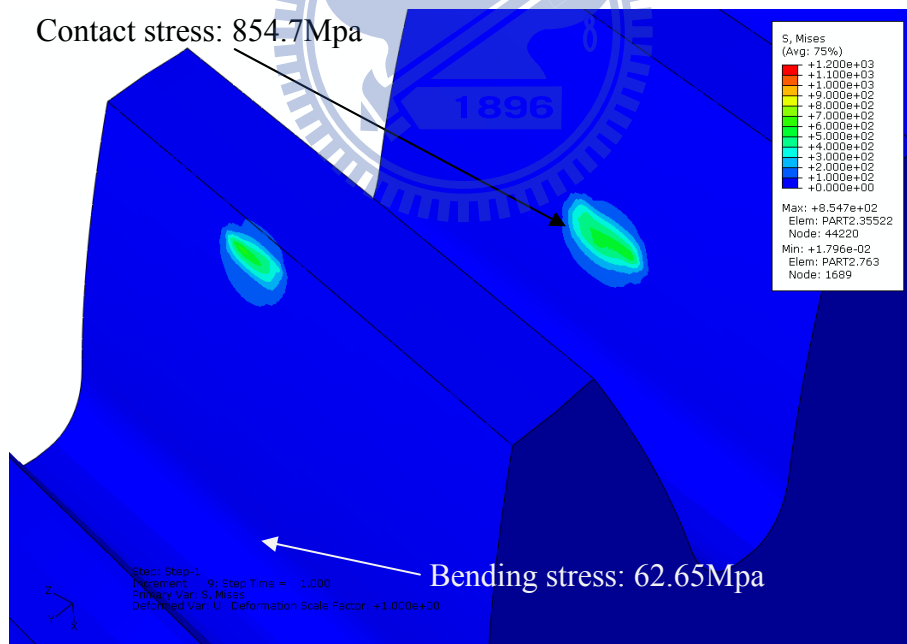


(b) Concave gear

Fig. 5.15 von-Mises stress distributions on tooth surfaces of the spherical helical gear set with convex pinion and concave gear under crossed axes mounting mode and ideal assembly condition

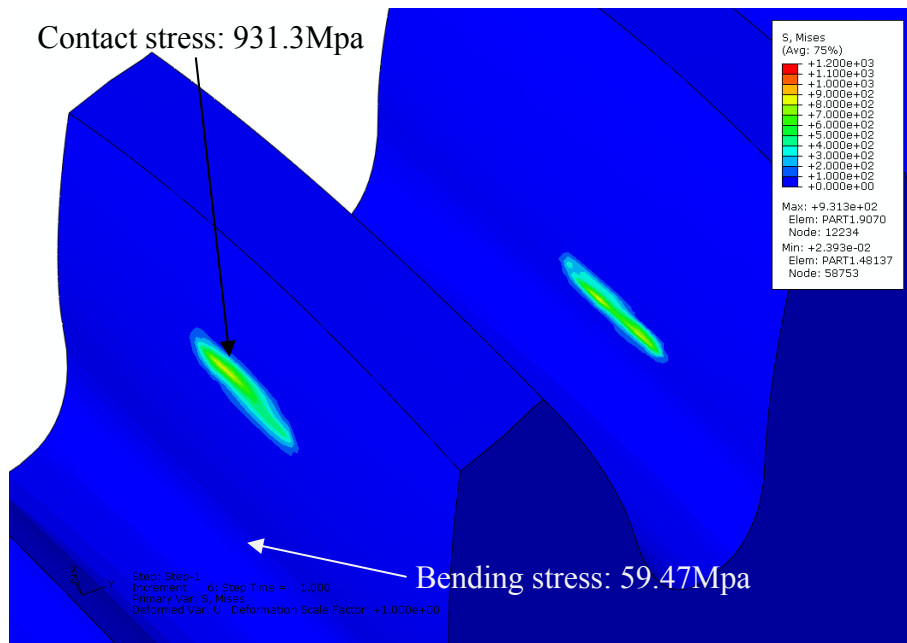


(a) Convex pinion

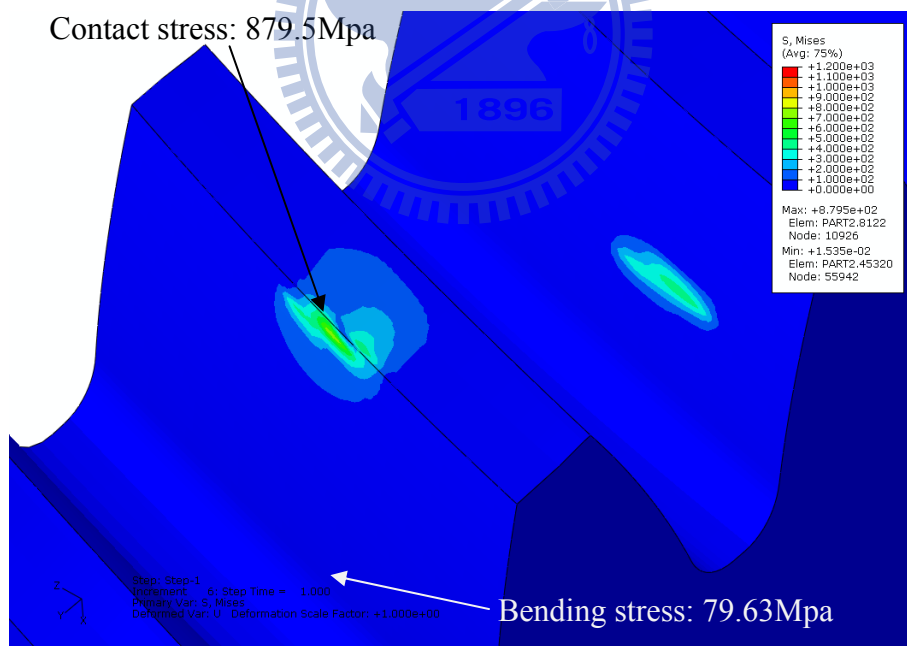


(b) Conventional helical gear

Fig. 5.16 von-Mises stress distributions on tooth surfaces of the spherical helical gear set with convex pinion and conventional helical gear under crossed axes mounting mode and ideal assembly condition



(a) Convex pinion



(b) Concave gear

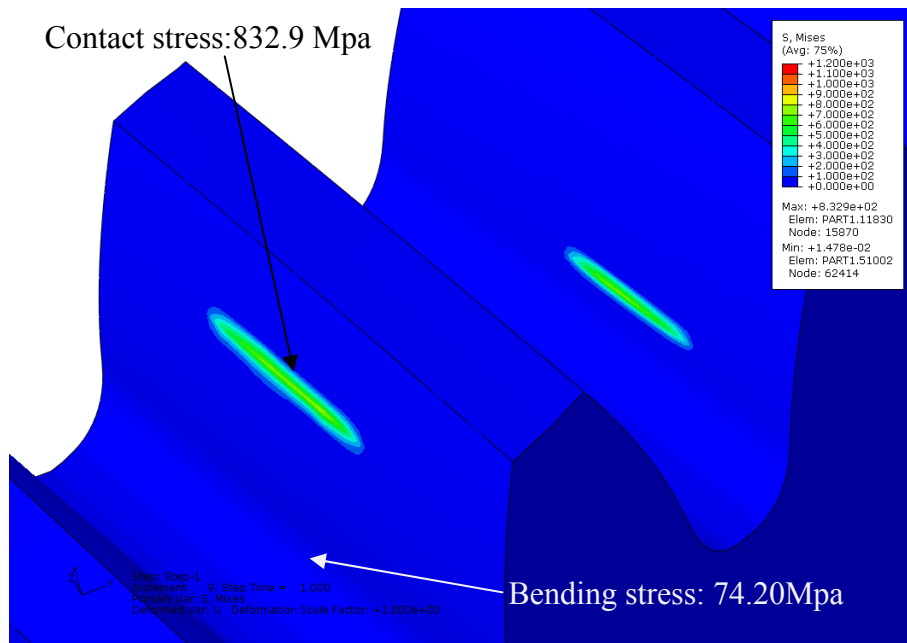
Fig. 5.17 von-Mises stress distributions on tooth surfaces of the spherical helical gear set with convex pinion and concave gear under crossed axes mounting mode and ideal assembly condition

misalignments. The contact stresses of the convex pinion and concave gear at the pinion's beginning rotation angle are 931.3MPa and 879.5MPa, respectively, whereas the bending stresses are 59.47MPa and 79.63MPa, respectively. However, there is still no edge contact occurred for the spherical helical gear set even under the crossed axes mounting mode and axial assembly misalignments.

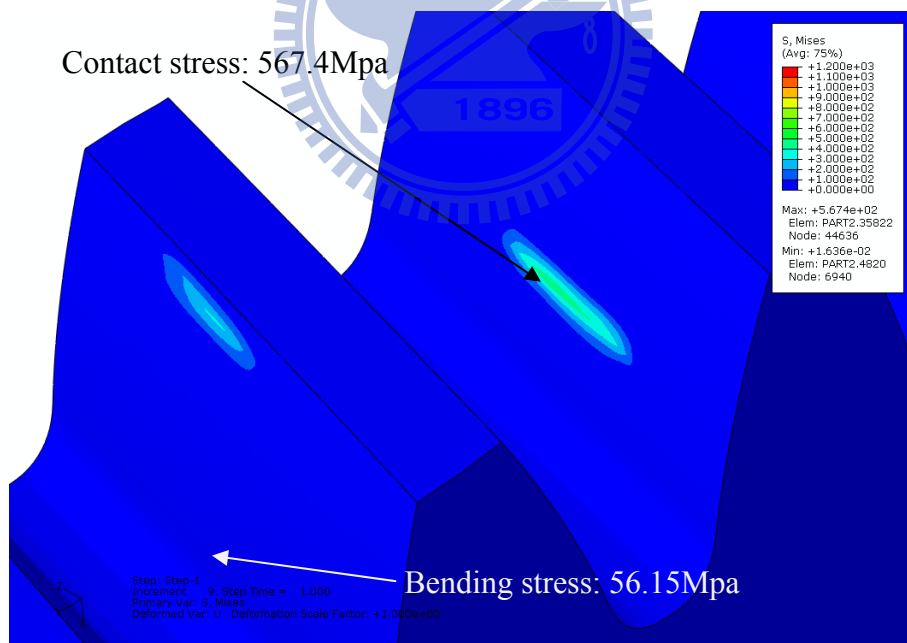
Example 5.6 Stress analysis of the spherical helical convex pinion mating with concave gear with large modified spherical radii R_j ($j=1$ and 2) under crossed axes mounting mode

In this example, a large modified spherical radius R_j ($j=1$ and 2 ; refer to Figs. 2.4 and 2.6) also has been applied to the spherical helical gear set under crossed axes mounting mode. The convex pinion with a modified spherical radius of $R_1=1000\text{mm}$ is given to mesh with the concave gear with a modified spherical radius of $R_2=1200\text{mm}$. Moreover, the design parameters of the spherical helical gear set are also given in Table 5.5, while the gear set is assembled under the ideal condition.

A conventional helical gear set is in point contact during its meshing. The tooth shapes of spherical helical pinion and gear with large modified spherical radii are quite similar to those of conventional helical gears. Therefore, the contact region of the spherical helical gear set only has a slightly increasing by adopting the large modified spherical radii for convex pinion and concave gear as shown in Fig. 5.18. The contact stresses of convex pinion and concave gear at the pinion's beginning rotation angle are 832.9MPa and 567.4MPa, respectively, while the bending stresses are 74.20MPa and 56.15MPa, respectively. Therefore, the contact stresses of the spherical helical gear set at the pinion's beginning rotation angle are substantially decreased compared with those of Example 5.4.



(a) Convex pinion



(b) Concave gear

Fig. 5.18 von-Mises stress distributions on tooth surfaces of the spherical helical gear set with large modified spherical radii under the parallel axes mounting mode and ideal assembly condition

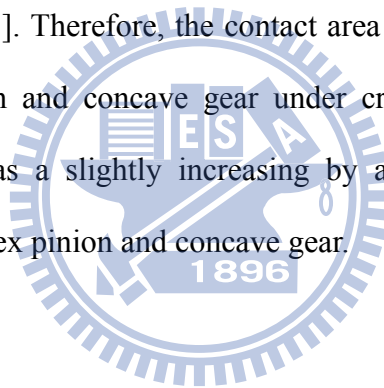
5.4 Remarks

According to the developed mathematical model (Chapter 2) and TCA simulation (chapter 4) of the spherical helical gear set, the FE meshing model of the gear set with local refined meshes for stress analyses have been performed by the developed automatic mesh-generation program of the gear set. Investigations on the contact and bending stresses of the spherical helical gear set with assembly conditions under two axes mounting modes and three types of mating combinations have been performed by employing the commercial FEA package, ABAQUS/Standard. The analysis results lead to the following conclusions:

- (1) Among three types of mating combinations of spherical helical gear sets with ideal assembly condition, the spherical helical gear sets composed of convex pinion and concave gear under parallel (Example 5.1) and crossed (Example 5.4) axes mounting modes have the smallest contact and bending stresses, whereas the spherical helical gear set composed of convex pinion and convex gear has the largest contact and bending stresses.
- (2) For the spherical helical gear set composed of convex pinion and concave gear with large axial misaligned angles $\Delta\gamma_v = 2.0^\circ$ and $\Delta\gamma_h = 0.5^\circ$ under parallel axes mounting mode (Example 5.2), the contact zone of the gear set has a small shift along the longitudinal direction of face width of the gear set, and the contact stress only has a slightly change when compared with the spherical helical gear set with convex pinion and concave gear under the ideal assembly condition (Example 5.1). Moreover, the contact zone of the spherical helical gear set with large axial misaligned angles $\Delta\gamma_v = 2.0^\circ$ and $\Delta\gamma_h = 0.5^\circ$ under crossed axes mounting mode (Example 5.5) also has a small shift along the longitudinal direction of face width of the gear set. The contact stress only has a slightly

change when compared with the spherical helical gear set with convex pinion and concave gear under the ideal assembly condition (Example 5.4).

- (3) The contact area of the spherical helical gear set with convex pinion and concave gear under parallel axes mounting mode (Example 5.3) can be increased by adopting a large modified spherical radius. Therefore, the increase of contact region results in the decrease of contact stress. If the spherical radii of the gear set with spherical helical pinion and gear under crossed axes mounting mode are modified and approach to infinite, the gear set composed of spherical helical pinion and gear will become a conventional helical gear set under crossed axes mounting mode. However, a conventional helical gear set is in point contact during its meshing [3-5]. Therefore, the contact area of the spherical helical gear set with convex pinion and concave gear under crossed axes mounting mode (Example 5.6) only has a slightly increasing by adopting the large modified spherical radii for convex pinion and concave gear.



CHAPTER 6

Conclusions and Future works

6.1 Conclusions

In this study, the mathematical models of the convex (Eqs. (2.31)~(2.33)) and concave (Eqs. (2.58)~(2.60)) spherical helical gears are developed in chapter 2. Then, based on the developed mathematical models of the spherical helical gears, the condition equations of the tooth undercutting (Eqs. (3.7)~(3.9)) and tooth pointing (Eqs. (3.35)~(3.40)) for the convex and concave spherical helical gears are derived in chapter 3, respectively. The limit curve of tooth undercutting and Z_g cross-section of tooth pointing beginning for the convex and concave spherical helical gears under different design parameters are also investigated, respectively. In chapter 4, a general form of meshing model of the spherical helical set with assembly errors under two axes mounting modes is developed (Eqs. (4.1) and (4.2)). According to the meshing model of the spherical helical gear set, the equations of the contact ellipses (Eqs. (4.13)~(4.15)) of the gear set is developed by utilizing the surface separation topology method [37]. Therefore, the KEs, contact ratios, contact loci and contact ellipses of the spherical helical gears sets with assembly errors under two axes mounting modes and three mating combinations are investigated. Moreover, an automatic mesh-generation program for the contact models of the spherical helical gear sets under two axes mounting modes and three types of mating combinations is developed. Therefore, the stress distributions on tooth surfaces of the spherical helical gear set under two axes mounting modes and three mating combinations are determined by using the software ABAQUS/Standard. Based on the analysis results obtained in the previous chapters, the following conclusions are drawn:

- (1) The mathematical model of convex and concave spherical helical gears generated by a ZN-type worm-type hob cutter has been developed based on the cutting mechanism of a 5-axes CNC hobbing machine. The tooth profiles obtained by the mathematical model can be considered as a standard profile for the convex and concave spherical helical gears.
- (2) The kinematic method to find the differentiated equations of meshing is developed for analyzing tooth undercutting of the convex spherical helical gear. According to the tooth undercutting analysis results, the occurrence of tooth undercutting at the both-end sections of face width of the convex spherical helical gear is much easier than other sections. The tooth undercutting of the convex spherical helical gear can be avoided with a large number of teeth or pressure angle, and the tooth undercutting may lessen by decreasing the pitch radius of hob cutter.
- (3) The tooth pointing of the concave spherical helical gear is investigated by utilizing the derived condition equations of tooth pointing of the concave spherical helical gear. According to the tooth pointing analysis results, the concave spherical helical gear can be avoided with a large number of teeth or small pressure angle. The tooth pointing of the concave spherical helical has a slight effect by changing pitch radius of the hob cutter.
- (4) The spherical helical gear set under two axes mounting modes and three mating combinations generated by a ZN-type worm-type hob cutter induces KEs when the gear set is meshing under ideal assembly condition and center distance error. However, the level of KEs of the gear set is small. Moreover, the KEs of the gear set are not sensitive to axial shifting of face width and axial misalignments because the contact type of the proposed spherical helical gear set is in point contacts.
- (5) The spherical helical gear set under two axes mounting modes and three mating

combinations with axial misalignments has a larger level of bearing contact shifting than other assembly error conditions. However, the bearing contacts of the spherical helical gear set with a large axial misalignment are still located near by the middle region of the face width. It means that there is no edge contact on the pinion and gear tooth surfaces of the spherical helical gear set.

- (6) The CRs of the spherical helical gear set under the two axes mounting modes and three mating combinations with ideal assembly condition and the large axial misalignments ($\Delta\gamma_v = 2^\circ$ and $\Delta\gamma_h = 0.5^\circ$) are about 1.7. Moreover, the CRs of the spherical helical gear sets under the two axes mounting modes and three mating combinations are not sensitive to the large axial misalignments.
- (7) An automatic mesh-generation program for generating the FE contact model of the spherical helical gear sets under two axes mounting modes and three mating combinations is developed. Moreover, the FE meshes, the definition of contacting surfaces, material properties and boundary conditions of the gear sets are also automatically generated by using the developed computer program. The stress analysis of the spherical helical gear set is performed by utilizing the software ABAQUS/Standard. The analysis results show that the spherical helical gear set with convex pinion and concave gear has the smallest contact and bending stresses due to the largest contact region, whereas the gear set with convex pinion and convex gear has the largest contact and bending stresses due to the smallest contact region.
- (8) Due to the conventional helical gear set is in line contact, the helical gear set with small axial misalignments under parallel axes mounting mode has edge contact and tooth interference (see Appendix B). However, the spherical helical gear set with larger axial misalignments ($\Delta\gamma_v = 2^\circ$ and $\Delta\gamma_h = 0.5^\circ$) under parallel axes

mounting mode has no edge contact and no tooth interference.

- (9) The large modified spherical radius can decrease the contact and bending stresses of the spherical helical gear set with convex pinion and concave gear under parallel and crossed axes mounting modes. Since the spherical helical gear set with a large modified spherical radius under crossed axes mounting mode is similar to that of a conventional helical gear set under crossed axes mounting mode, the contact and bending stresses of the gear set with convex pinion and concave gear under parallel axes mounting mode have larger decreasing margin than that of the gear set under crossed axes mounting mode by the same increasing margin of the spherical radius.

6.2 Future works

The tooth surfaces of the convex and concave spherical helical gears generated by a ZN-type hob cutter are indeed new types of gear surfaces. Advanced studies of these kinds of gear for industrial applications are important and necessary. In the future, the following research topics can be extended:

- (1) The illustrated approach in Chapter 2 can be further extended to derive the mathematical model for noncircular hobbing locus of the gears, e.g. parabolic or elliptical curved hobbing locii.
- (2) The sensitivity analysis can be used to study the surface deviation of the spherical helical gear with respect to hob cutter settings in the manufacturing process.
- (3) The curvature analysis of the proposed convex and concave spherical helical gears should be developed for the determination of principal curvatures and directions of the surfaces of convex and concave spherical helical gears.
- (4) Real contact ratio, load sharing between the meshing teeth, and transmission error under the given load may be implemented by considering multi-tooth finite

element models. Moreover, the effect of friction force may be investigated by defining the tooth surfaces interaction with friction.

(5) In order to save the preprocess time of the finite element model of other types of gear sets, the developed automatic mesh-generation program of chapter 5 can be further extended to include other types of gear sets, e.g. curvilinear-tooth gear set, bevel gear set, conical gear set, gear set of worm and worm wheel, etc. Moreover, the developed automatic mesh-generation program can be packaged as a plug-in for the software ABAQUS/Standard.

(6) The single flank test and the measurement of noise and vibrations could be performed with the proposed convex and concave spherical helical gear sets.



REFERENCES

- [1] Mitome, K., Okuda, T., Ohmachi, T. and Yamazaki, T., “Develop of a New Hobbing of Spherical Gear,” *Journal of JSME*, Vol. 66 , pp. 1975-1980, 2000.
- [2] 山崎隆, “軸断面形状を変え、特色を出した円錐形歯車と球形歯車,” *機械設計*, 第 34 卷, 第 13 号, 第 53-60 頁, 1990.
- [3] Litvin, F. L., *Theory of Gearing*, NASA Reference Publication 1212, Washington D.C., 1989.
- [4] Litvin, F. L., *Gear Geometry and Applied Theory*, PTR Prentice Hall, Englewood Cliffs, New Jersey, 1994.
- [5] Litvin, F. L. and Fuentes, A., *Gear Geometry and Applied Theory, 2nd Edition*, Cambridge University Press, 2004.
- [6] Mancuso, J. R., *Couplings and Joints, 2nd Edition*, Marcel Dekker, 1999.
- [7] Yang, S. C., “Mathematical Model of a Ring-Involute-Teeth Spherical Gear with a Double Degree of Freedom,” *Journal of Advanced Manufacturing Technology*, Vol. 20, pp. 865-870, 2002.
- [8] Yang, S. C., “A Rack-Cutter Surface Used to Generate a Spherical Gear with Discrete Ring-Involute-Teeth,” *Journal of Advanced Manufacturing Technology*, Vol. 27, pp. 14-20, 2005.
- [9] Yang, S. C., Chen, C. K. and Li, K. Y., “A Geometric Model of a Spherical Gear with a Double Degree of Freedom,” *Journal of Material Processing Technology*, Vol. 123, pp. 219-224, 2002.
- [10] Yang, S. C., “Study of an Elbow Mechanism Generated by a Conical Cutter,” *Proceedings of the Institution of Mechanical Engineerings Part C: Journal of Mechanical Engineering Science*, Vol. 221, pp. 727-738, 2007.
- [11] Tsai, Y. C. and Jehng, W. K., “Rapid Prototyping and Manufacturing Technology

- Applied to the Forming of Spherical Gear Sets with Skew Axes,” *Journal of Materials Processing Technology*, Vol. 95, pp. 169-179, 1999.
- [12] Chao, L. C. and Tsay, C. B., “Contact Characteristics of Spherical Gears,” *12th World Congress in Mechanism and Machine Science*, Vol. 2, pp. 236-241, 2007.
- [13] Chao, L. C. and Tsay, C. B., “Contact Characteristics of Spherical Gears,” *Mechanism and Machine Theory*, Vol. 43, pp. 1317-1331, 2008.
- [14] Chao, L. C. and Tsay, C. B., “Stress Analysis of Spherical Gear Sets,” *ASME International Design Engineering Technical Conferences*, DETC2009- 86843 (CD-ROM), pp. 1-7, San Diego, California, U.S.A., Aug. 30~Sep. 02, 2009.
- [15] Wang, W. S. and Fong, Z. H., “A Dual Face-Hobbing Method for the Cycloidal Crowning of Spur Gears,” *Mechanism and Machine Theory*, Vol. 43, pp. 1416-1430, 2008.
- [16] Mao, K., “Gear Tooth Contact Analysis and its Application in The Reduction of Fatigue Wear,” *Wear*, Vol. 262, pp. 1281-1288, 2007.
- [17] Wang, J. D., and Howard, I. M., “Errors Analysis of Finite Element Modeling of Involute Spur Gears,” *ASME Journal of Mechanical Design*, Vol. 128, pp. 90-97, 2006.
- [18] Chen, W. H. and Tsai, P., “Finite Element Analysis of an Involute Gear Drive Considering Friction Effects,” *ASME Journal of Engineering for Industry*, Vol. 111, pp. 94-111, 1989.
- [19] Ganesan, N. and Vijayarangan, S., “Static Contact Stress Analysis of a Spur Gear Tooth Using the Finite Element Method, Including Frictional Effects,” *Computers and Structures*, Vol. 51, pp. 765-770, 1994.
- [20] Tsay, C. B., “Helical Gears with Involute Shaped Teeth: Geometry, Computer Simulation, Tooth Contact Analysis, and Stress Analysis,” *Journal of Mechanisms, Transmissions, and Automation in Design*, Vol. 110, pp. 482-491,

- 1988.
- [21] Litvin, F. L., Fuentes, A., Gonzalez-Perez, I., Carnevali, L. and Sep, T. M., “New Version of Novikov–Wildhaber Helical Gears: Computerized Design, Simulation of Meshing and Stress Analysis,” *Computer Methods in Applied Mechanics and Engineering*, Vol. 191, pp. 5707-5740, 2002.
- [22] Chen, Y. C. and Tsay, C. B., “Tooth Contact Analysis and Kinematic Optimization of a Modified Helical Gear Pair with Involute-Teeth Pinion and Modified-Circular-Arc Gear,” *Journal of the Chinese Society of Mechanical Engineers*, Vol. 21, pp. 537-547, 2000.
- [23] Chen, Y. C. and Tsay, C. B., “Stress Analysis of a Helical Gear Set with Localized Bearing,” *Finite Element in Analysis and Design*, Vol. 38, pp. 707-723, 2002.
- [24] Brauer, J., “A General Finite Element Model of Involute Gears,” *Finite Element in Analysis and Design*, Vol. 40, pp. 1857-1872, 2004.
- [25] Colbourne, J. R., “The Contact Stress in Novikov Gear,” *Mechanism and Machine Theory*, Vol. 24, pp. 223-229, 1989.
- [26] Liu, C. C. and Tsay, C. B., “Contact Characteristic of Beveloid Gears,” *Mechanism and Machine Theory*, Vol. 37, pp. 333-350, 2002.
- [27] Liu, C. C. and Tsay, C. B., “Tooth Undercutting of Beveloid Gears,” *ASME Journal of Mechanical Design*, Vol. 123, pp. 569-576, 2001.
- [28] Tsai, Y. C. and Chin, P. C., “Surface Geometry of Straight and Spiral Bevel Gears,” *Journal of Mechanism, Transmissions, and Automation in Design*, Vol. 109, pp. 443-449, 1987.
- [29] Litvin, F. L., Fuentes, A. and Hayasaka, K., “Design, Manufacture, Stress Analysis, and Experimental Tests of Low-Noise High Endurance Spiral Bevel Gears,” *Mechanism and Machine Theory*, Vol. 41, pp. 83-118, 2006.

- [30] Litvin, F. L., Chen, J. S., and Lu, J., "Application of Finite Element Analysis for Determination of Load Share, Real Contact Ratio, Precision of Motion, and Stress Analysis," *ASME Journal of Mechanical Design*, Vol. 118, pp. 561-567, 1996.
- [31] Chang, S. L. and Tsay, C. B., "Computerized Tooth Profile Generation and Undercut Analysis of Noncircular Gears Manufactured with Shaper Cutters," *ASME Journal of Mechanical Design*, Vol. 120, No.1, pp. 92-99, 1998.
- [32] Tseng, R. T. and Tsay, C. B., "Mathematical Model and Undercutting of Cylindrical Gears with Curvilinear Shaped Teeth," *Mechanism and Machine Theory*, Vol. 36, pp. 1189-1202, 2001.
- [33] Tseng, R. T. and Tsay, C. B., "Contact Characteristics of Cylindrical Gears with Curvilinear Shaped Teeth," *Mechanism and Machine Theory*, Vol. 39, pp. 905-919, 2004.
- [34] Tseng, J. T. and Tsay, C. B., "Mathematical Model and Surface Deviation of Cylindrical Gears with Curvilinear Shaped Teeth Cut by Hob Cutter," *ASME Journal of Mechanical Design*, Vol. 127, pp. 982-987, 2005.
- [35] Tseng, J. T. and Tsay, C. B., "Undercutting and Contact Characteristics of Cylindrical Gears with Curvilinear Shaped Teeth Generated by Hobbing," *ASME Journal of Mechanical Design*, Vol. 128, pp. 635-643, 2006.
- [36] Simon, V., "The Influence of Gear Hobbing on Worm Gear Characteristics," *ASME Journal of Manufacturing Science and Engineering*, Vol. 129, pp. 919-925, 2007.
- [37] Janninck, W. K., "Contact Surface Topology of Worm Gear Teeth," *Gear Technology*, March/April, pp. 31-47, 1988.
- [38] Litvin, F. L., Nava, A., Fan, Q. and Fuentes, A., "New Geometry of Face Worm Gear Drives with Conical and Cylindrical Worms Generation, Simulation of

- Meshing, and Stress Analysis,” *Computer Methods in Applied Mechanics and Engineering*, Vol. 191, pp. 3035-3054, 2002.
- [39] Fang, H. S. and Tsay, C. B., “Mathematical Model and Bearing Contacts of the ZN-type Worm Gear Set Cut by Oversize Hob Cutters,” *Mechanism and Machine Theory*, Vol. 35, pp. 1689-1708, 2000.
- [40] Maki, M. and Sakai, T., “A Study on Hourglass Worm Gearing With Developable Tooth Surfaces,” *Journal of Mechanical Design*, Vol. 100, pp. 451-459, 1978.
- [41] Chen, K. Y. and Tsay, C. B., “Mathematical Model and Worm Wheel Tooth Working Surfaces of the ZN-Type Hourglass Worm Gear Set,” *Mechanism and Machine Theory*, Vol. 44, pp. 1701-1712, 2009.
- [42] Simon, V., “Stress Analysis in Double Enveloping Worm Gears by Finite Element Method,” *ASME Journal of Mechanical Design*, Vol. 115, pp. 179-185, 1993.
- [43] Sun, S. C. and Hung, C. H., *The Research on Finite Element Simulation of Deformable Bodies Contact*, Master thesis, National Chiao Tung University, 2000.
- [44] Tsai, Y. C. and Hung, C. H., *The Research on FEM Mesh System Applied to 3D Contact Analysis of Elastically Deformable Bodies*, Master thesis, National Chiao Tung University, 2002.
- [45] Litvin, F. L. and Seol, I. H., “Computerized Determination of Gear Tooth Surface as Envelope to two Parameter Family of Surfaces,” *Computer Methods Apply Mechanical Engineering*, Vol. 138, pp. 213-225, 1996.
- [46] Zienkiewicz, O. C., and Taylor, R. L., *The Finite Element Method for Solid and Structural Mechanics, 6th Edition*, John Wiley, 2000.
- [47] Dudley, D. W., *Dudley’s Gear Handbook, 2nd Edition*, McGraw-Hill, U.S.A.,

New York, 1992.

- [48] ABAQUS/Standard 6.2, *User's Manual*, Hibbitt, Karlsson & Sorensen, U.S.A., 2001.

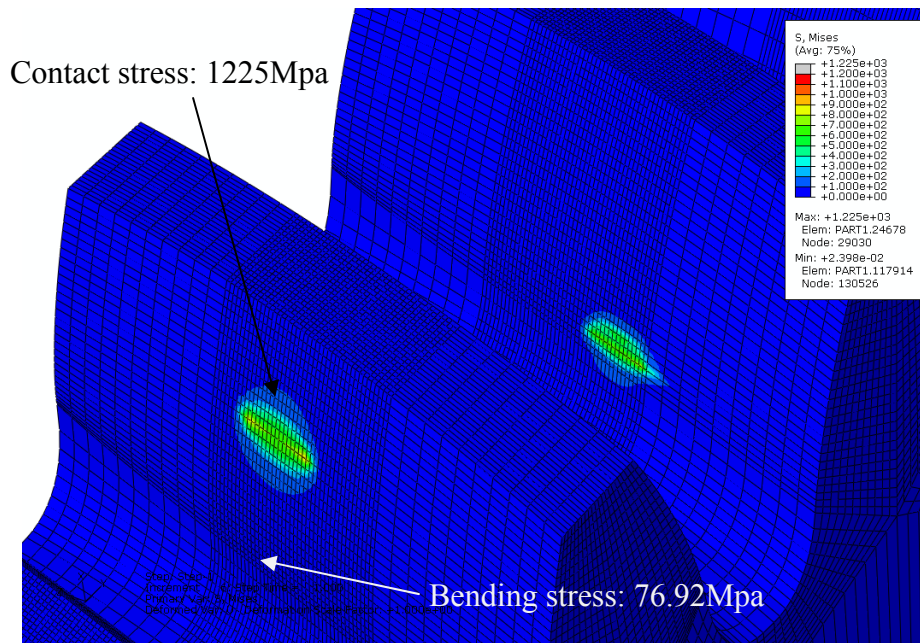


Appendix A

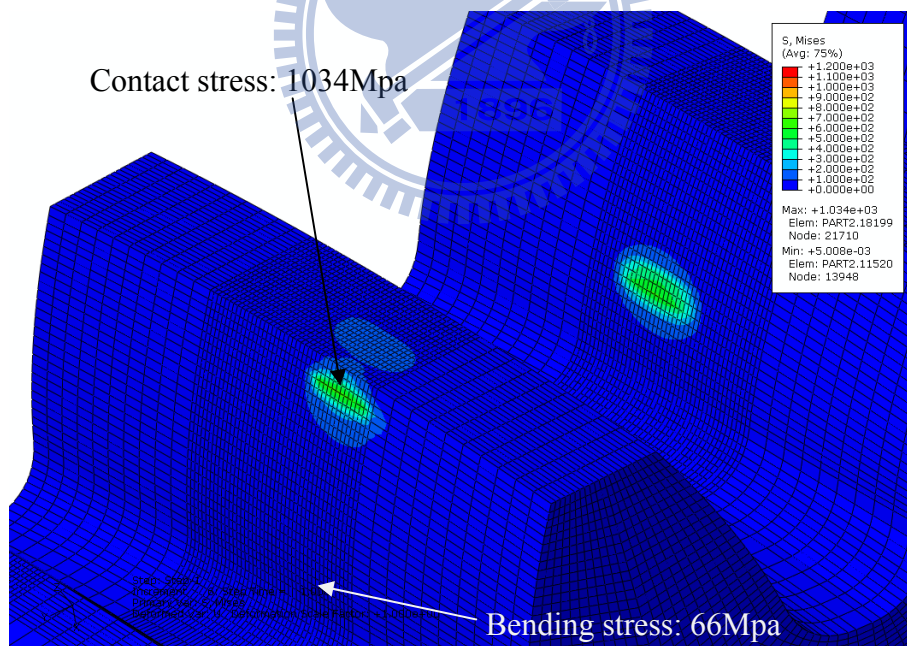
Stress distributions of A Spherical Helical Gear Set with Uniform Element Size along Tooth Thickness Direction

Example A.1 Stress distributions of spherical helical gear sets with convex pinion and convex gear under parallel axes mounting mode and ideal assembly condition

The stress analysis result of the spherical helical gear set with convex pinion and convex gear are illustrated in Fig. A.1. The design parameters of the gear set are the same as those of Table 5.3. Noteworthy, the element sizes along the tooth thickness direction of the convex pinion and convex gear of the gear set are uniform (see Fig. A.1), moreover, the other settings of element size of the convex pinion and convex gear are the same as those of the spherical helical gear set with convex pinion and convex gear of Example 5.1. The contact stresses of the convex pinion and convex gear at the pinion's beginning rotation angle are 1225MPa and 1034MPa, respectively, whereas the bending stresses are 76.92MPa and 66MPa, respectively. By comparing the analysis results (Fig. A.1) of Example A.1 with those of Example 5.1 (Fig. 5.9), the contact and bending stresses only have a slight change between the two examples. However, the analysis time cost of Example A.1 is expensive due to the total elements and nodes are 297228 and 325080, respectively. Therefore, the local refined mesh along the tooth thickness direction of the pinion and gear is also adopted in this study for stress analysis of the spherical helical gear sets under parallel and crossed axes mounting modes.



(a) Convex pinion



(b) Convex gear

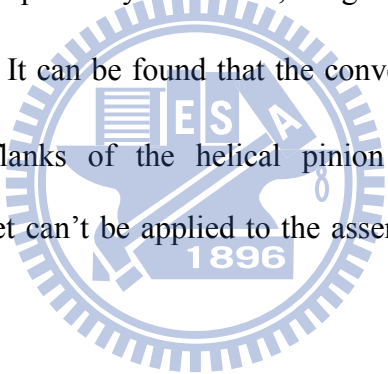
Fig. A.1 von-Mises stress distributions on tooth surfaces of the spherical helical gear set with convex pinion and convex gear under the parallel axes mounting mode and ideal assembly condition

Appendix B

Stress Distributions of A Conventional Helical Gear Set with Axial Misalignments under Parallel Axes Mounting Mode

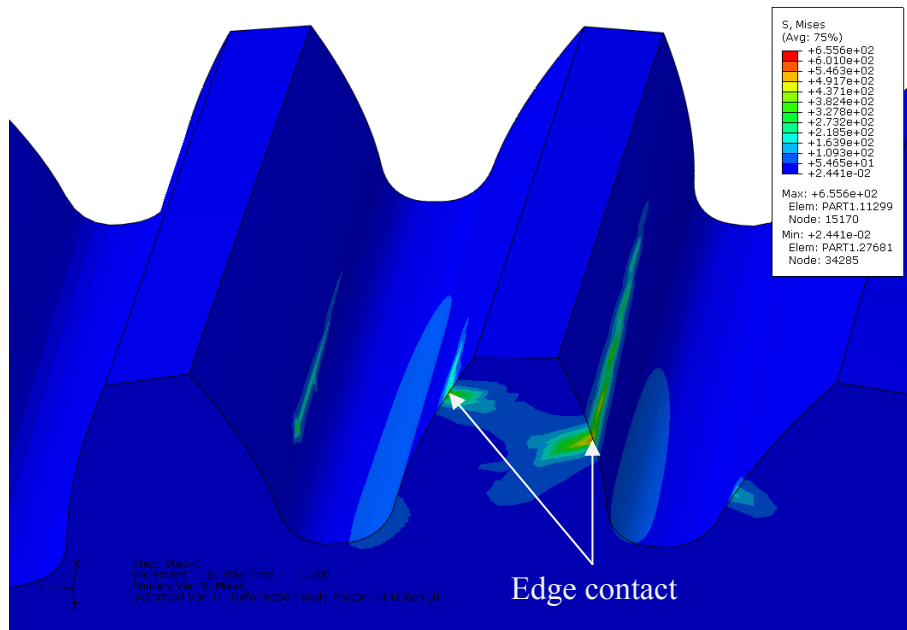
Example B.1 Stress distributions of conventional helical gear set with axial misalignment $\Delta\gamma_v = 0.15^\circ$ under parallel axes mounting mode

Figure B.1 illustrates stress distributions of the conventional helical gear set with 33 teeth helical pinion and 47 teeth helical gear under parallel axes mounting mode. The normal module and normal pressure angle of the helical pinion and gear are 4 mm/tooth and 20 degrees, respectively. Moreover, the gear set is assembled with axial misalignment $\Delta\gamma_v = 0.15^\circ$. It can be found that the conventional helical gear set has edge contacts on tooth flanks of the helical pinion and gear. Therefore, the conventional helical gear set can't be applied to the assembly condition with a large axial misalignment $\Delta\gamma_v$.

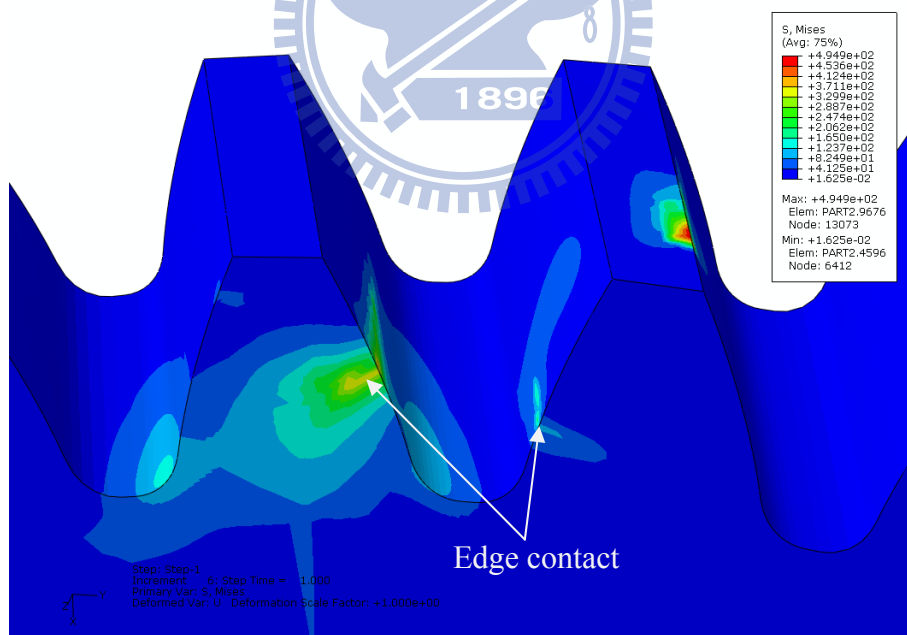


Example B.2 Stress distributions of conventional helical gear set with axial misalignment $\Delta\gamma_h = 0.1^\circ$ under parallel axes mounting mode

The design parameters of the conventional helical gear set of this example are given the same as those of Example B.2. The gear set is assembled with axial misalignment $\Delta\gamma_h = 0.1^\circ$ under parallel axes mounting mode. Figure B.2 illustrates stress distributions of the helical pinion and gear set. It can be found that the gear set also has edge contact on the tooth flanks of the helical pinion and gear. Therefore, the conventional helical gear set can't be applied to the assembly condition with a large axial misalignment $\Delta\gamma_h$.

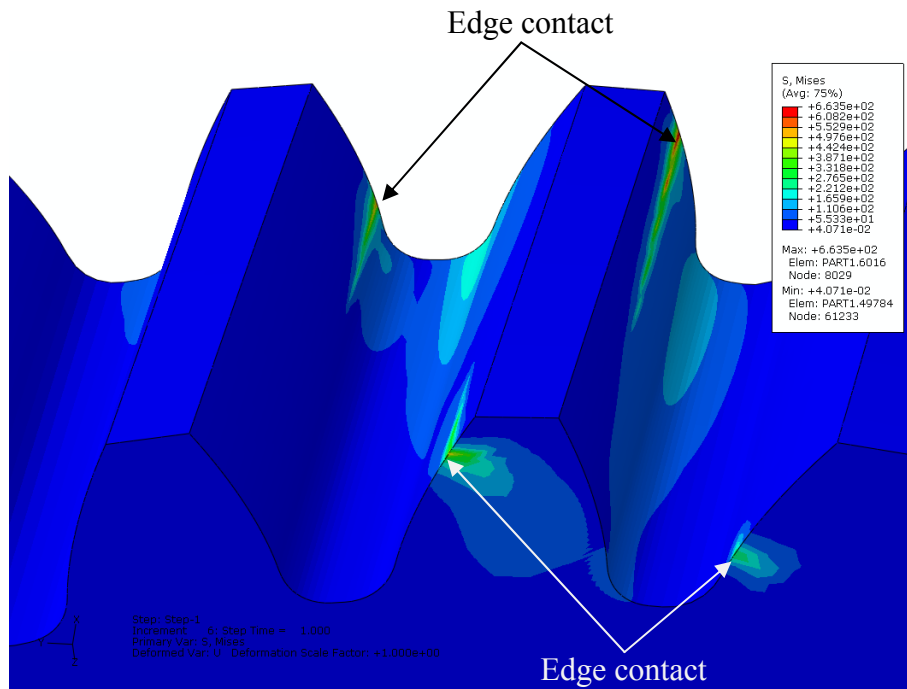


(a) Conventional helical pinion

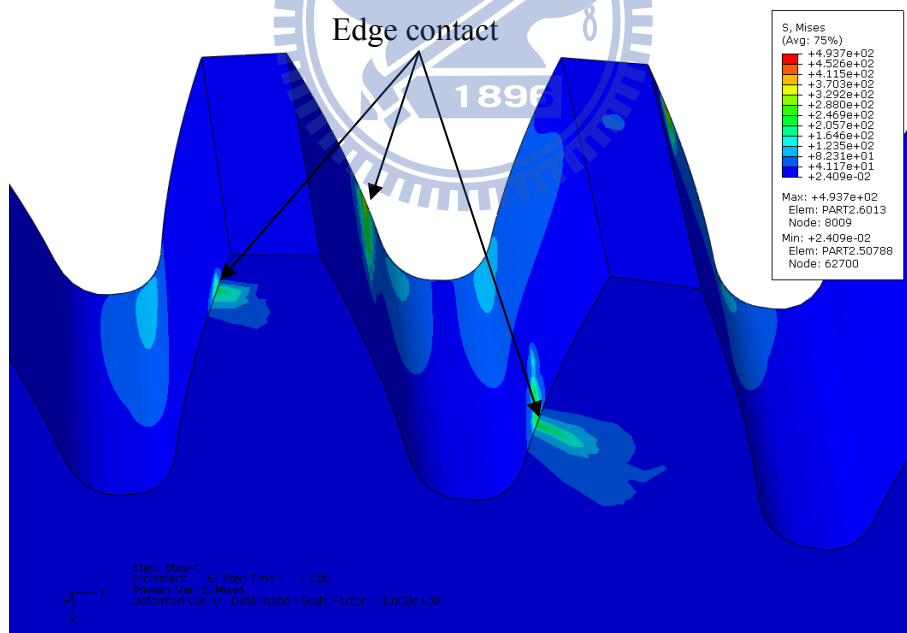


(b) Conventional helical gear

Fig. B.1 von-Mises stress distributions on tooth surfaces of the conventional helical gear set with axial misalignment $\Delta\gamma_v = 0.15^\circ$ under the parallel axes mounting mode



(a) Conventional helical pinion



(b) Conventional helical gear

Fig. B.2 von-Mises stress distributions on tooth surfaces of the conventional helical gear set with axial misalignment $\Delta\gamma_h = 0.1^\circ$ under the parallel axes mounting mode